# FINAL REPORT

## Advanced Magnetometer System

### SERDP Project MR-2646

NOVEMBER 2020

Dr. Rui Zhang
Rahul Mhaskar
**Geometrics, Inc.**

SERDP
DOD ▪ EPA ▪ DOE

| REPORT DOCUMENTATION PAGE | *Form Approved*<br>*OMB No. 0704-0188* |
|---|---|

| | | |
|---|---|---|
| **1. REPORT DATE** *(DD-MM-YYYY)*<br>12/11/2020 | **2. REPORT TYPE**<br>SERDP Final Report | **3. DATES COVERED** *(From - To)*<br>9/26/2016 - 9/26/2021 |

| | |
|---|---|
| **4. TITLE AND SUBTITLE**<br>Advanced Magnetometer System | **5a. CONTRACT NUMBER**<br>16-C-0010 |
| | **5b. GRANT NUMBER** |
| | **5c. PROGRAM ELEMENT NUMBER** |
| **6. AUTHOR(S)**<br>Dr. Rui Zhang<br>Rahul Mhaskar | **5d. PROJECT NUMBER**<br>MR-2646 |
| | **5e. TASK NUMBER** |
| | **5f. WORK UNIT NUMBER** |
| **7. PERFORMING ORGANIZATION NAME(S) AND ADDRESS(ES)**<br>Geometrics, Inc.<br>2190 Fortune Drive<br>San Jose, CA, 95131 | **8. PERFORMING ORGANIZATION REPORT NUMBER**<br>MR-2646 |
| **9. SPONSORING/MONITORING AGENCY NAME(S) AND ADDRESS(ES)**<br>Strategic Environmental Research and Development Program (SERDP)<br>4800 Mark Center Drive, Suite 16F16<br>Alexandria, VA 22350-3605 | **10. SPONSOR/MONITOR'S ACRONYM(S)**<br>SERDP |
| | **11. SPONSOR/MONITOR'S REPORT NUMBER(S)**<br>MR-2646 |

**12. DISTRIBUTION/AVAILABILITY STATEMENT**
DISTRIBUTION STATEMENT A. Approved for public release: distribution unlimited.

**13. SUPPLEMENTARY NOTES**

**14. ABSTRACT**

Scalar magnetometers and Time-Domain Electromagnetic (TDEM) systems are proven and effective technologies used extensively in the field to detect, discriminate and classify unexploded ordnance (UXO). These two methods complement each other with magnetometers being excellent at detecting large and deep ferrous targets but having limited discrimination capability while the opposite is true for TDEM systems. A combined magnetometer-electromagnetic system is ideal for UXO remediation. However, without complicated interleaving method, it is not possible to simultaneously run both sensors in the close vicinity to each other due to the interruption of the magnetometer operation by the electromagnetic (EM) pulses. Our objective is to enable integration of miniature laser-pumped cesium magnetometers with TDEM systems by improving the magnetometer sensor to function in presence of an EM transmitter.

**15. SUBJECT TERMS**

Scalar Atomic Magnetometer, Time-Domain Electromagnetic System, Polar Angle, Angle Measurement, Digital Signal Processing, UXO Discrimination, Low Frequency Magnetic Field Excitation

| **16. SECURITY CLASSIFICATION OF:** | | | **17. LIMITATION OF ABSTRACT** | **18. NUMBER OF PAGES** | **19a. NAME OF RESPONSIBLE PERSON**<br>Rui Zhang |
|---|---|---|---|---|---|
| **a. REPORT**<br>UNCLASS | **b. ABSTRACT**<br>UNCLASS | **c. THIS PAGE**<br>UNCLASS | UNCLASS | 83 | **19b. TELEPHONE NUMBER** *(Include area code)*<br>408-954-0522 |

# Contents

# List of Figures

# List of Acronyms

A – Ampere
AOM – Acousto-optic Modulator
Cs – Cesium
DBR – Distributed Bragg Reflector
DC – Direct Current
DPLL – Digital Phase Locked Loop
DSP – Digital Signal Processing
EM – Electromagnetic
ESTCP – Environmental Security Technology Certification Program
FPGA – Field-programmable Gate Array
FWHM – Full Width at Half Maximum
GPS – Global Positioning System
Hz – Hertz
kHz – kilohertz
MFAM – MicroFabricated Atomic Magnetometer
ms – milli-second
nT – nanoTesla
pT – picoTesla
µs – micro-second
µT – microTesla
OD – Optical Density
PI – Proportional Integral
PLL – Phase Locked Loop
SERDP – Strategic Environmental Research and Development Program
TDEM – Time-Domain Electromagnetic
ToI – Target of Interest
UXO – Unexploded Ordnance
VCSEL – Vertical Cavity Surface Emitting Laser
3-D – Three-dimensional

# List of Keywords

Scalar Atomic Magnetometer, Time-Domain Electromagnetic System, Polar Angle, Angle Measurement, Digital Signal Processing, UXO Discrimination, Low Frequency Magnetic Field Excitation

# Abstract

***Introduction and Objectives***: Scalar magnetometers and Time-Domain Electromagnetic (TDEM) systems are proven and effective technologies used extensively in the field to detect, discriminate and classify unexploded ordnance (UXO). These two methods complement each other with magnetometers being excellent at detecting large and deep ferrous targets but having limited discrimination capability while the opposite is true for TDEM systems. A combined magnetometer-electromagnetic system is ideal for UXO remediation. However, without complicated interleaving method, it is not possible to simultaneously run both sensors in the close vicinity to each other due to the interruption of the magnetometer operation by the electromagnetic (EM) pulses. Our objective is to enable integration of miniature laser-pumped cesium magnetometers with TDEM systems by improving the magnetometer sensor to function in presence of an EM transmitter.

***Technical Approach***: Ongoing developments in integrating, miniaturizing and digitizing magnetometer sensor electronics, funded by SERDP, allow for novel methods of interrogating the sensors. The digital signal processing (DSP) approach in the sensor driver also provides an avenue to analyze the dynamic behavior of the magnetic field. This allows us to extract extra field information from the magnetometer operation, such as the field angle. The DSP approach simplifies the implementation of the fast-recovery algorithm of the magnetometer operation interrupted by the EM pulses by searching the magnetic resonance in the close vicinity of a predicted magnetic field. Combining this fast-recovery method with the field angle information, it is possible to achieve the magnetic field measurement during the EM pulses.

***Results***: Better than 0.02° sensitivity has been achieved in the field angle measurement at the optimal orientation of the magnetic field with a measurement time of 100 milliseconds. The demonstrated angle measurement shows that it is possible to achieve the fast tracking of the EM pulse with our advanced magnetometer system. Less than one millisecond recovery time after the EM pulses has been demonstrated in the laboratory. In the field application, a portable system with the magnetometer and an EM transmitter was used to conduct magnetic field surveys. Compared with the magnetometer-only survey, the magnetometer-EM surveys show similar magnetic field results with EM frequencies up to 200 Hertz. Our study delivers a promising prospect that simultaneous magnetic field measurement and EM measurement can become commercially available in the near future. A new method for UXO detection and discrimination has also been explored.

***Benefit***: An array of miniature magnetometers can be integrated with EM transmitters and receivers to achieve simultaneous magnetic field and EM measurements. Such a hybrid magnetometer-EM system can greatly improve the efficiency of detection and remediation of unexploded ordnance, especially in an underwater environment. Accurate location parameters of targets, extracted from the magnetic field data, can be incorporated into the interpretation of the transient decay curves, collected by the TDEM system, to enhance the UXO discrimination and classification. Challenges in an underwater environment such as limited visibility, mobility of targets and the absence of GPS positioning can potentially be overcome by combining the real-time target localization using the magnetometer array with the high-confidence UXO discrimination with the TDEM system.

# Executive Summary

## 1. Introduction

Scalar magnetometers and Time-Domain Electromagnetic (TDEM) systems are proven and effective technologies used extensively in the field to detect, discriminate and classify unexploded ordnance (UXO). These two methods complement each other with magnetometers being excellent at detecting large and deep ferrous targets but having limited discrimination capability while the opposite is true for TDEM systems. A combined magnetometer-electromagnetic system is ideal for UXO remediation. However, without complicated interleaving method, it is not possible to simultaneously run both sensors in the close vicinity due to the interruption of the magnetometer operation by the electromagnetic (EM) pulses.

## 2. Objectives

The objective of this project is to enable integration of miniature laser-pumped cesium magnetometers with TDEM systems by improving the magnetometer sensor to function in presence of an EM transmitter.

## 3. Technical Approach

Scalar atomic magnetometers rely on the resonant Larmor precession of atomic spins to measure the magnitude of the magnetic field. A high-amplitude EM pulse can interrupt the magnetometer operation by collapsing the precession signal. It typically takes a few tens of milliseconds for the magnetometer to find the resonant Larmor frequency again. The recovery time can be greatly reduced if the initial driving frequency is set to be close to the resonant Larmor frequency. This hypothesis can be verified in the lab using a bench top magnetometer setup shown in Figure 1.

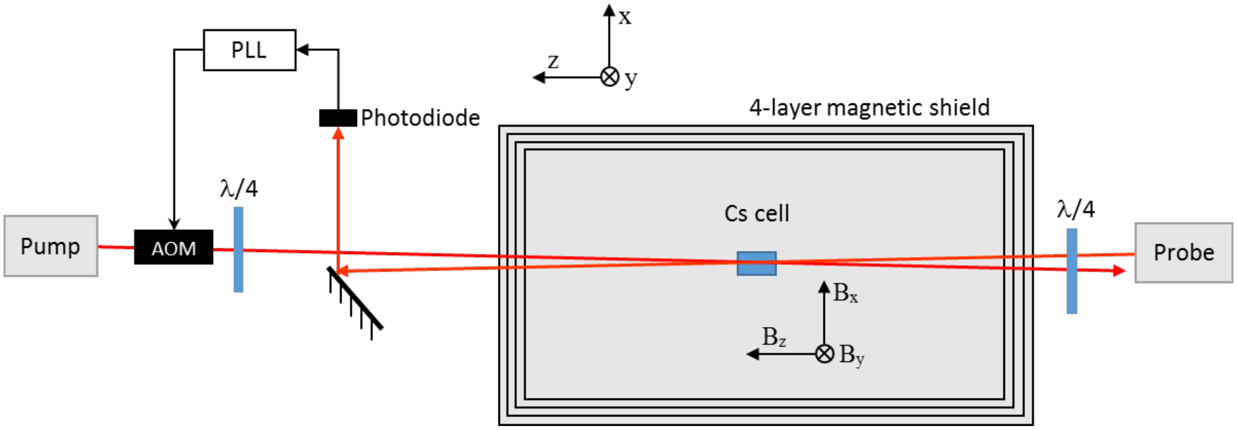

Figure 1 Schematic of the experimental setup of a bench-top scalar atomic magnetometer.

A cuboid vapor cell containing Cs atoms is placed inside a 4-layer magnetic shield can. The cell is resistively heated to operating temperature. The pump and probe lights come from two Distributed Bragg Reflector (DBR) lasers and are circularly polarized with a quarter-wave plate. The pump light is amplitude-modulated with an acousto-optic modulator (AOM). The angle between the two beams is about 1°. The fundamental operating principal of the magnetometer is based on the Bell-Bloom scheme. The pump light periodically aligns atomic spins. The precession of the atomic spins in a magnetic field is detected by the counter-propagating probe beam. The transmitted probe light is detected and conditioned using the phase-lock-loop (PLL) electronics to determine the Larmor frequency and also control the AOM driving frequency. Inside the shield can, the magnetic field in x, y and z directions can be independently controlled.

We set the constant background magnetic field around $B_x$ = 60.55 μT inside the shield can, corresponding to a resonant Larmor frequency of 212 kHz. Amplitude and phase of the Larmor signal across the resonant Larmor frequency are shown as the black and red curves, respectively, in Figure 2. To investigate the dependence of the PLL settle time on the difference between the starting pump modulation frequency and the resonant Larmor frequency, the initial pump modulation frequency is set to be different from the resonant Larmor frequency before the PLL loop is closed. The tested starting pump frequencies are indicated by the blue lines in Figure 2. At t = 0, the PLL is enabled.

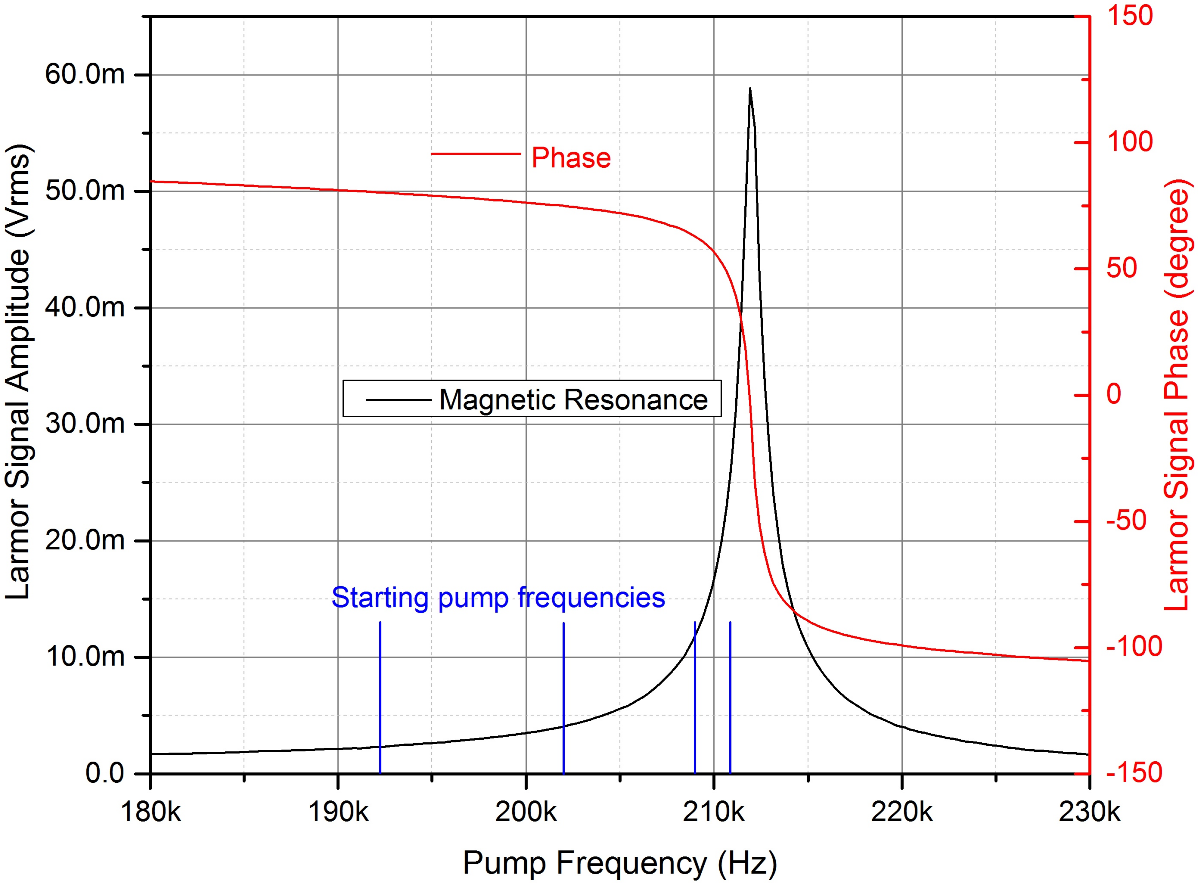

**Figure 2 Magnetic resonance signal (black curve), its phase (red curve) and the starting pump frequencies (indicated by the blue lines).**

We first set the initial pump frequency to be 1 kHz away from the resonant Larmor frequency, shown as the closest blue line to the magnetic resonance signal in Figure 2. We record both the Larmor signal (black curve) and the magnetometer reading (red curve) around t=0, shown in Figure 3 (a). As can be seen, in less than 1 ms, the magnetometer outputs the correct field reading. Meanwhile the Larmor signal also reaches steady state. Notice that the field reading settles much faster than the signal amplitude because PLL measures the frequency, not the amplitude, of the Larmor signal. We also set the initial pump frequency to be 3 kHz, 10 kHz and 20 kHz away from the resonant Larmor frequency. Corresponding results are shown in Figure 3 (b), (c) and (d), respectively. As expected, the further away the initial pump frequency, the longer it takes for the magnetometer to recover its normal operation. This verifies our technical approach: to achieve fast-recovery of magnetometer operation, it is necessary to set the initial pump modulation frequency close to the resonant Larmor frequency of Cs atoms. Note that in order to record both the Larmor signal (analog) and the magnetometer reading (digital) at the same time, the digital reading is first converted to an analog signal through a digital-analog converter. The magnetometer reading appears to settle at different values most likely due to the nonlinearity of the converter. The reading range is only 0.4μT in (a) compared with 6.5μT in (d).

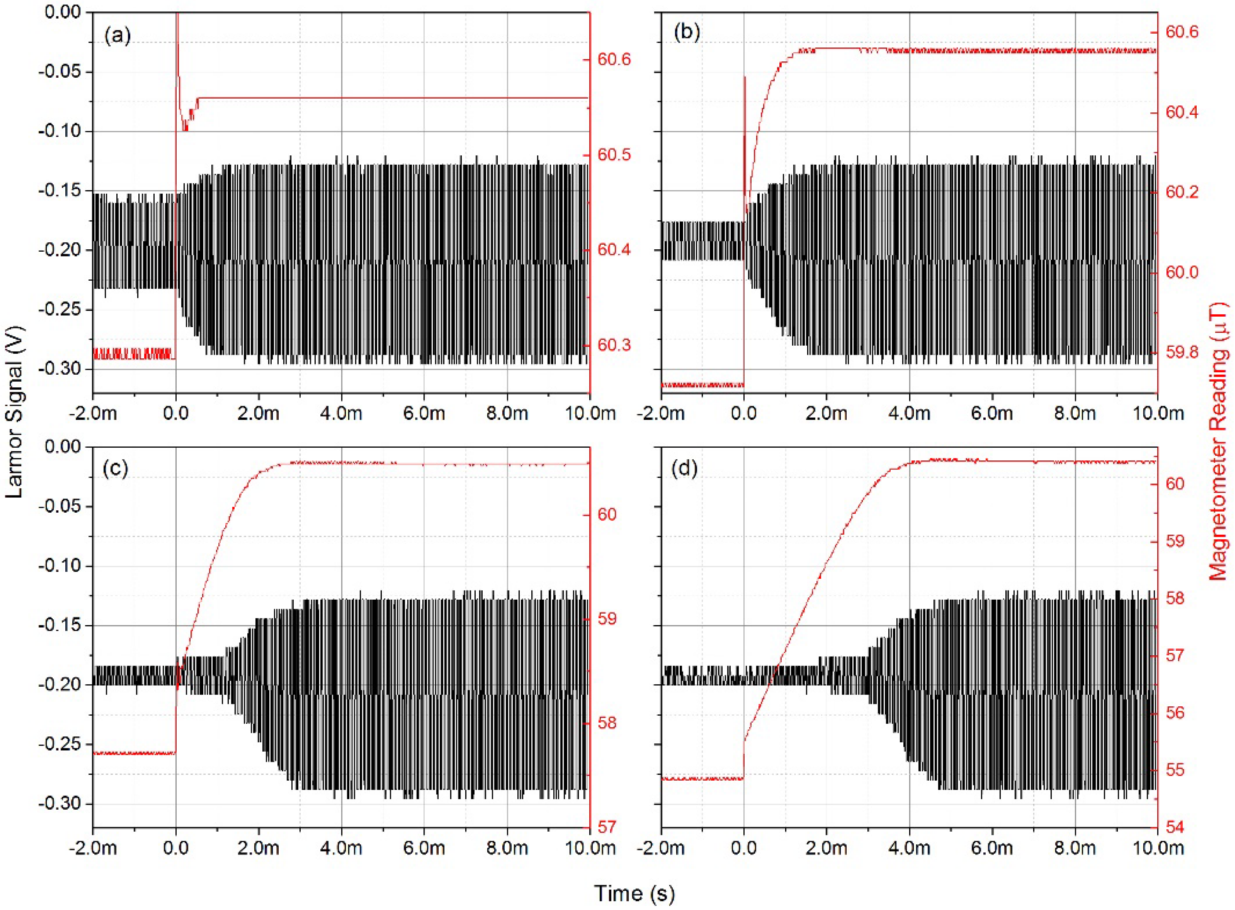

**Figure 3 Reading of the magnetometer after the PLL is enabled (red curves). The initial pump modulation frequency is (a) 1 kHz, (b) 3 kHz, (c) 10 kHz and (d) 20 kHz away from the resonant Larmor frequency, corresponding to 4 blue lines in Figure 2. The probe Larmor signal detected by the photodiode is also shown as the black curve.**

A new UXO detection method based on low frequency AC magnetic field excitation is also explored. Assuming two magnetometers are placed near an aluminum plate with one sensor closer to the plate than the other, as shown in Figure 4. A low frequency AC magnetic field, such as a 60 Hz oscillating field, is present in the background. Without the aluminum plate, the 60 Hz components in two magnetometer outputs have the same phase. With the aluminum (or any metal) plate, an eddy current is induced by the oscillating magnetic field. The eddy current has the same frequency as the exciting AC field. But its amplitude and phase are determined by many factors such as the frequency of the exciting field, the conductivity of the material as well as the size and shape of the target. Due to the eddy current, a secondary oscillating magnetic field is generated with the same frequency as the main AC field but a slightly different phase. As a result, the overall 60 Hz signal at one sensor location is phase shifted from that at the other sensor since the secondary field amplitude decreases fast away from the plate. Based on this theory, we should be able to use the phase difference between two sensors as a signal to detect metal targets.

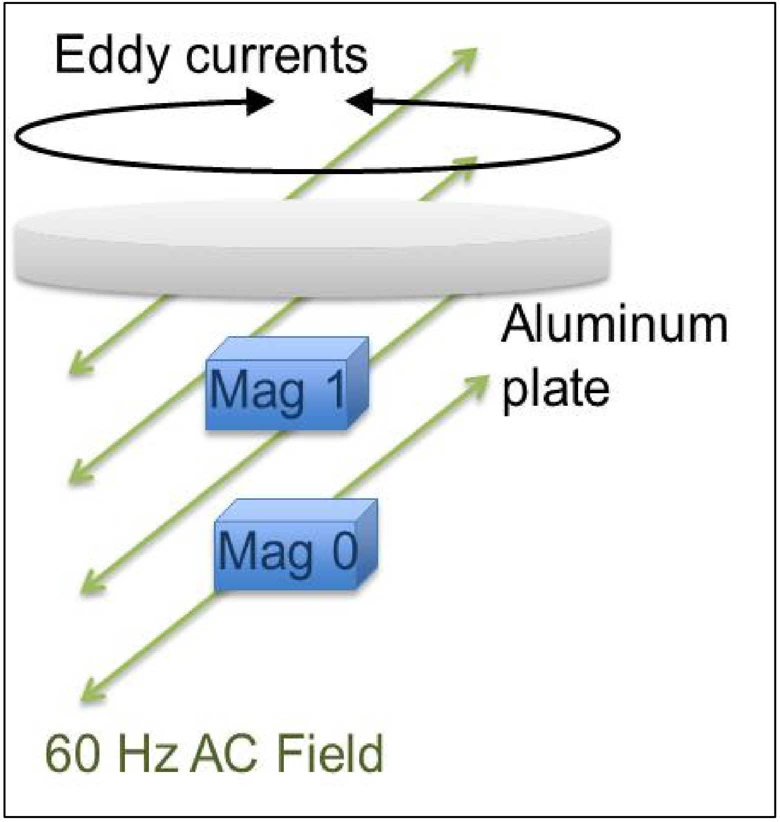

Figure 4 Low frequency AC magnetic field excitation method.

## 4. Results and Discussion

In our Micro-Fabricated Atomic Magnetometer (MFAM) sensor, we replaced the DBR lasers shown in Figure 1 with vertical cavity surface emitting lasers (VCSELs). The optical wavelength of the VCSELs can be dithered at the Larmor frequency through laser current modulation, thus eliminating the need for AOMs. With these changes, we were able to integrate the bench top magnetometer into a sensor package less than 20 cubic centimeters in volume. All signals generated by the sensor are analyzed by a field-programmable gate array (FPGA). The phase-lock-loop (PLL) is realized through digital signal processing (DSP) inside the FPGA. The DSP allows us to implement complicated procedures in the sensor driver to achieve fast-recovery of MFAM operation in presence of EM pulses.

After implementing the fast-recovery procedure, we test the MFAM operation with a commercially available TDEM system, MetalMapper from Geometrics. The setup is shown in Figure 5. To simplify the testing setup, we move the target, instead of the MFAM-MetalMapper system during the test. For the maximum effect of the EM pulse on the magnetometer operation, the MFAM sensor head is placed directly on top of the MetalMapper. We record the MFAM readings during on and off stages of the MetalMapper. In the meanwhile the magnetic target travels back and forth in the tube, changing the total magnetic field by about 25 nT at the location of the sensor. When the MetalMapper is on, it generates 8 ms pulses in alternating directions separated by 8 ms off times. The pulse has amplitude much larger than the Earth's field at the location of the sensor. The raw MFAM output, including valid and invalid readings, is plotted in Figure 6 (a). As can be seen, when the MetalMapper is turned on, MFAM reading becomes very noisy, overwhelming any magnetic field signals. After the MetalMapper is switched off, the signal of the moving magnetic target clearly shows up. The reading noise during MetalMapper off is dominated by 60 Hz oscillating magnetic fields generated by nearby power lines.

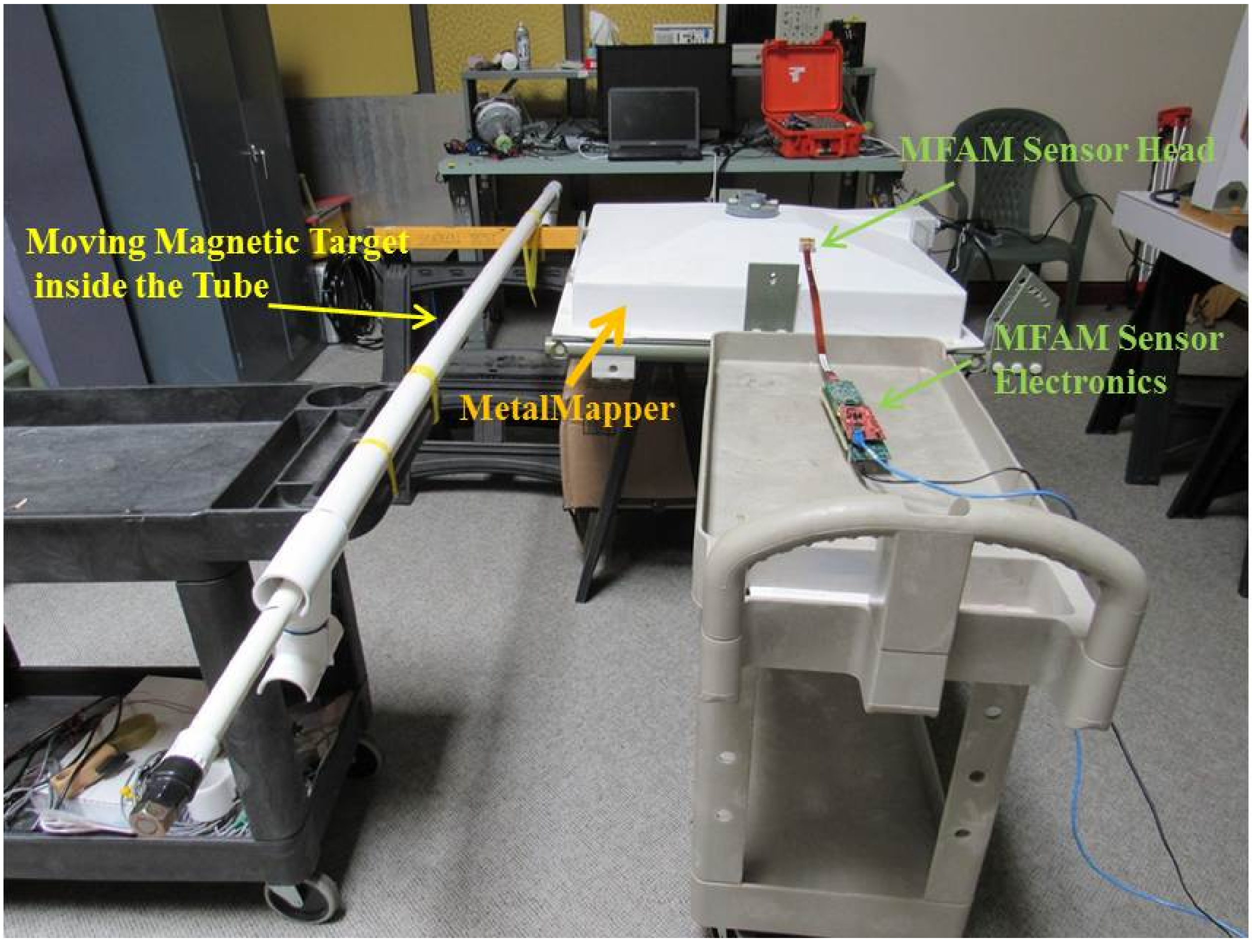

Figure 5 Setup for testing the simultaneous operation of the magnetometer and the MetalMapper.

If the MFAM recovery time is much less than 8 ms and an internal signal can be used to distinguish between valid and invalid readings, noises caused by the MetalMapper can be filtered out and the real magnetic response will be recovered. We rely on the amplitude of the Larmor signal to filter out invalid readings. In Figure 6 (b), we plot only the valid readings of the same data in Figure 6 (a). Filtered data indicates that turning on the MetalMapper almost has no effect on the MFAM operation.

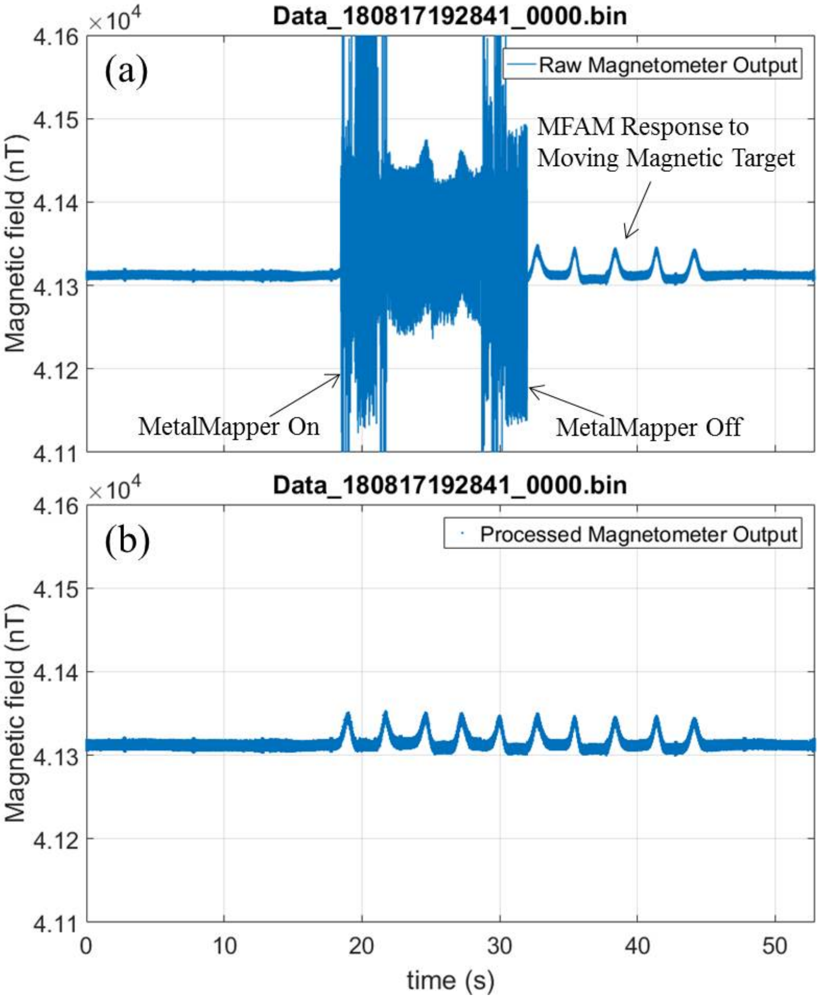

Figure 6 MFAM readings during on and off of the MetalMapper. (a) Raw MFAM output including valid and invalid readings. (b) The same data as in (a), but only valid readings are plotted as dots.

Figure 7 Combined MFAM-EM transmitter system and NASA field testing site.

Field testing of a combined MFAM-EM transmitter system is conducted at a survey site inside the NASA Ames Research Center, shown in Figure 7. The survey site is covered by 6 40-feet scanning lines with 3 feet line spacing. We first conduct the survey without turning on the EM pulses. The survey result is shown in Figure 8 (a). Two targets can be clearly located in the survey map. The EM pulses are then turned on during the survey. All pulse waveforms have 50% duty cycle, amplitude of more than 5 μT at the location of the sensor and the rising or falling edges of less than 10 μs. The frequency of the first waveform is 50 Hz. After collecting the raw MFAM data, the missing readings during the EM pulse on are interpolated based on the valid MFAM data. A 5 Hz low pass filter is then applied to the data set. The resulting MFAM survey result with 50 Hz EM pulses is plotted in Figure 8 (b). Compared with the data without the EM pulses in Figure 8 (a), the magnetic field survey is not impacted much by the 50 Hz EM pulses. We also applied 100 Hz and 200 Hz waveforms. The corresponding MFAM survey results are plotted in Figure 8 (c) and (d), respectively. These two data sets show that MFAM still generates valid magnetic field readings in presence of EM pulses up to 200 Hz. For bi-polar EM pulses, the maximum allowed frequency is about 100 Hz.

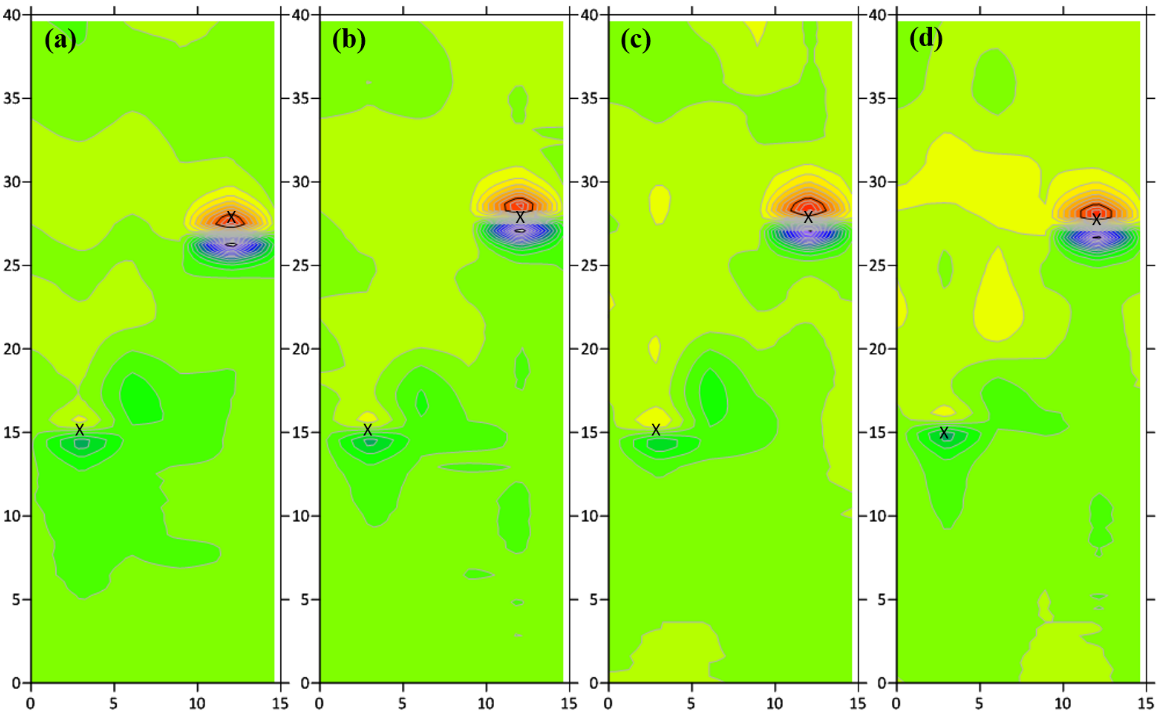

**Figure 8 Magnetic field survey results with two targets. (a) Without EM pulses. (b) With 50 Hz EM pulses. (c) With 100 Hz EM pulses. (d) With 200 Hz EM pulses. The color scale is in unit of nT. The target locations are marked by "x". Due to the positioning inaccuracy, the magnetic field survey results do not always overlap with the target locations.**

The low frequency AC magnetic field excitation method is also tested in the field. The excitation field has a sinusoidal waveform at 100 Hz with 5 μT peak-to-peak amplitude at the center of the coil. We place 7 targets on the survey site, including three magnetic ones and four non-magnetic ones. The locations are indicated by the marker "x". All three magnetic targets have similar size and shape (1.375 inch in diameter and 4.5 inch long) but with different magnetic signatures. Four non-magnetic targets are all made of aluminum. The setup for the new method collects magnetic field data, magnetic gradient data and AC field time delay data at the same time, shown in Figure 9 (a), (b) and (c), respectively. From Figure 9 (a) and (b), it is obvious that non-magnetic targets cannot be detected by the traditional magnetometer methods. But with the low frequency AC field excitation method, all metal targets can be detected. One interesting fact is that even for two magnetic targets with similar magnetic field or gradient amplitude, the time delay signal is very different. This is very likely due to the orientation difference between the two targets.

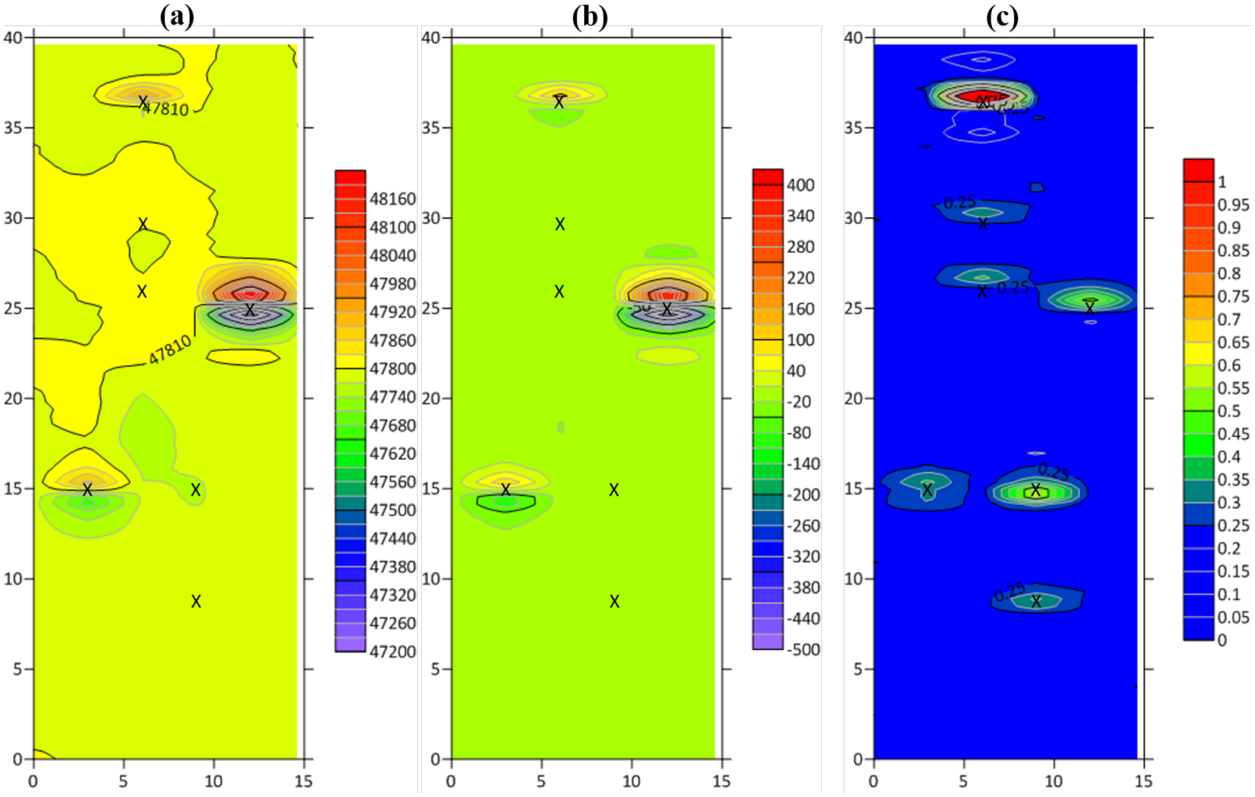

**Figure 9 Data collected by the low frequency AC excitation method. (a) Magnetic field data. (b) Magnetic gradient data. (c) AC field time delay data. The color scales for (a) and (b) are in unit of nT and the color scale in (c) is in unit of μs. The target locations are marked by "x". Due to the positioning inaccuracy, the survey results do not always overlap with the target locations.**

Overall we have demonstrated an advanced atomic magnetometer system capable of simultaneous operation with TDEM systems. Our field testing results confirm that the project has met its objective, which is to enable integration of MFAM sensors with TDEM systems by improving the sensor to function in presence of an EM transmitter. Magnetic field surveys over the same site have been conducted and survey results with and without EM pulses have been compared. No obvious compromise is found in the MFAM sensor performance with EM pulses up to 200 Hz in frequency. A new UXO detection and discrimination method has also been explored. Although the low frequency AC magnetic field excitation method has been successfully demonstrated in the field, our study indicates that further improvements, such as noise reduction in the time delay signal, are still necessary in order for this technique to work robustly in field applications.

## 5. Implications for Future Research and Benefits

The advanced magnetometers developed in this project can be easily integrated with TDEM systems to achieve simultaneous measurements of scalar magnetic field and transient EM signals. Such a hybrid magnetometer-EM system is expected to greatly improve the efficiency of UXO remediation, especially in an underwater environment where conducting surveys remains challenging. Accurate location parameters of targets, extracted from the magnetic field data, can be incorporated into the interpretation of the transient decay curves, collected by the TDEM system, to enhance the UXO discrimination and classification. With an array of MFAM sensors, it may be possible to achieve real-time target localization. Challenges in the underwater environment such as limited visibility, mobility of targets and the absence of GPS positioning can potentially be overcome by combining the real-time target localization using the magnetometer array with the high-confidence UXO discrimination with the TDEM system.

In the future, the low frequency AC magnetic field excitation method may be worth further investigation. We have clearly demonstrated the advantage of the method, which is to achieve additional information about the target without compromising the magnetic field measurement. It will be interesting to investigate how the additional information can be beneficial in UXO discrimination and classification and how to reduce motion-induced noises in field applications.

The advanced MFAM sensors also open door to a new research opportunity: transient magnetic field measurement. Traditional TDEM systems use induction coils to measure the dB/dt response of targets after cessation of EM transmitter pulses for UXO discrimination and classification. Although induction coils are effective in detecting dB/dt signal over early and intermediate times, they become less so over late times (> 10 ms) because of the fast decay of the dB/dt signal. Magnetometers measure B field directly. Since B field decays much slower than dB/dt, magnetometers may be more preferred in late-time measurements. Although transient or AC-coupled magnetometers exist that are capable of recovering and acquiring signal shortly after an EM pulse, they are orders of magnitude less sensitive than the MFAM sensors. With the fast-recovery technique developed in this project, MFAM sensors are now capable of measuring magnetic field less than 2 ms after the EM pulses. New and useful information may be revealed by the MFAM sensors in the late-time transient magnetic field measurement.

## Objective

The objective of this project is to enable integration of miniature laser-pumped cesium magnetometers with Time-Domain Electromagnetic (TDEM) systems by improving the magnetometer sensor to function in presence of an electromagnetic (EM) transmitter. This technology addresses MRSON-16-01: Detection, Classification, and Remediation of Military Munitions Underwater. In particular, this project addresses the issues of sensor development and analysis methodologies as applicable to detailed surveys. The project is based on the new generation of atomic sensors utilizing the digital signal processing (DSP) to track the magnetic field. The DSP approach simplifies the implementation of complicated magnetic field tracking algorithms that are necessary when the normal magnetometer operation is constantly interrupted by EM pulses.

## Background

Scalar magnetometers and Time-Domain Electromagnetic (TDEM) systems are proven and effective technologies used extensively in the field to detect, discriminate and classify unexploded ordnance (UXO). These two methods complement each other with magnetometers being excellent at detecting large and deep ferrous targets but having limited discrimination capability while the opposite is true for TDEM systems. A combined magnetometer-electromagnetic system is ideal for UXO remediation, especially in an underwater environment where UXO remediation is particularly difficult due to the dynamical nature of the environment, limited visibility, mobility of targets, and the absence of GPS positioning. However, it is not trivial to simultaneously operate both sensors in the close vicinity to each other due to the interruption of the magnetometer operation by the electromagnetic (EM) pulses. Previous researches, such as ESTCP UX-0208, ESTCP MM-0414 and ESTCP MR-200733, have focused on the interleave method [1, 2, 3], where the magnetometers are only sampled after the EM pulses have diminished. The interleave method requires additional customized electronics specifically for the interleaving purpose and the maximum sampling frequency is less than 20 Hz unless the magnetometers are separated by a few feet from the EM transmitters. All previous projects use analog-based traditional magnetometer sensors, which are large and consume a lot of power.

Recently Geometrics successfully commercialized the Micro-Fabricated Atomic Magnetometer (MFAM) technology, a miniaturized all-optical cesium magnetometer, the development of which is partly supported by SERDP through project MM-1512, MM-1568 and MR-2104. The MFAM sensor has a size of less than 20 cubic centimeters, consumes less than 3 Watts in power and reaches 1 pT/√Hz sensitivity. The unique DSP capability of the MFAM sensor allows us to explore more advanced methods to achieve the simultaneous magnetometer operation in presence of EM pulses. The specific technical objectives of the project include evaluating, through simulations and laboratory experiments, advanced methods of signal extraction in the scalar magnetometer instrument and implementing advanced methods of operating the sensors to obtain rapid DC magnetometer measurements in the presence of a TDEM system. The possibility of new discrimination techniques will also be explored using the advanced MFAM sensor.

# Materials and Methods

## 1. Extraction of Angle Information in Scalar Atomic Magnetometers

Scalar atomic magnetometers rely on the resonant Larmor precession of atomic spins to measure the magnitude of the magnetic field [4]. A high-amplitude EM pulse can interrupt the magnetometer operation by collapsing the precession signal. It typically takes a few tens of milliseconds for the magnetometer to find the resonant Larmor frequency again. The recovery time can be greatly reduced, however, if the initial driving frequency is set to be close to the resonant Larmor frequency. This can be implemented using the advanced digital signal processing (DSP) solutions we have developed for driving the scalar magnetometer. The resonant Larmor frequency during the EM pulse can be calculated based on the vector sum of the EM pulse and the background magnetic field. The EM pulse at the location of the magnetometer can be calibrated and the magnitude of the background field is measured by the scalar magnetometer. If the angle information about the background field can also be obtained, we will be able to implement the fast-recovery method of operating the scalar magnetometers in presence of EM pulses.

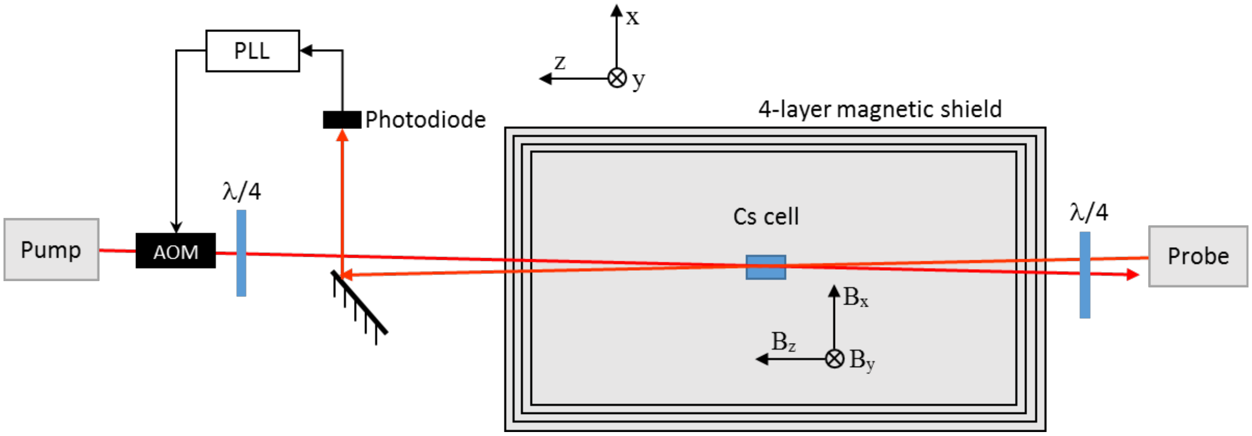

Figure 10 Schematic of the experimental setup of a bench-top scalar atomic magnetometer.

We used a bench-top scalar atomic magnetometer setup, shown schematically in Figure 10, to experimentally investigate different angle measurement concepts. A cuboid vapor cell containing Cs atoms is placed inside a 4-layer magnetic shield can. The cell is resistively heated to the operating temperature. The pump and probe lights come from two Distributed Bragg Reflector (DBR) lasers and are circularly polarized with a quarter-wave-plate. The pump light is amplitude-modulated with an acousto-optic modulator (AOM). The angle between the two beams is about 1°. The fundamental operating principal of the magnetometer is based on the Bell-Bloom scheme [5]. The pump light periodically aligns atomic spins. The precession of the atomic spins in a magnetic field is detected by the counter-propagating probe beam. The transmitted probe light is detected and conditioned using the phase-lock-loop (PLL) electronics to determine the Larmor frequency and also control the AOM driving frequency. Inside the shield can, the magnetic field in x, y and z directions can be independently controlled.

## 1.1. Extraction of polar angle from the DC transmission of the probe beam

### 1.1.1. Efficacy of the method

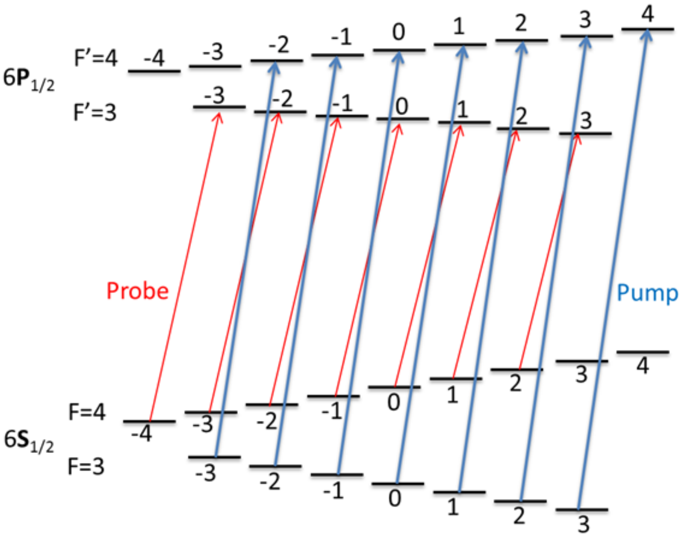

Figure 11 Transition diagram of the probe and pump beams.

The first method we investigate to measure the magnetic field orientation is based on the DC transmission of the probe light. The transition diagram of the pump-probe atomic magnetometer based on the Bell-Bloom scheme [5] is shown in Figure 11. The probe light is circularly polarized, resonant with the |F=4>→|F'=3> transition of Cs D1 line. The two extreme magnetic sublevels of |F=4> ground state are dark states to the probe. Atoms in these states will not interact with probe photons. When the polar angle, $\theta$ (the angle between the magnetic field and the light) is 90°, atoms decaying into the dark states will escape quickly due to the Larmor precession. However, when the light and the magnetic field are aligned (polar angle at 0° or 180°), atoms decaying into the dark states get trapped. This decreases the optical density (OD) of the vapor. The OD is defined as OD = -log($P_{out}/P_{in}$), where $P_{in}$ and $P_{out}$ are the input and output of the light power, respectively. We can write the effective OD for the probe light as $OD(\theta)=OD_0+OD_1*\sin^2\theta+OD_2*\sin^4\theta$. Here, $OD_0$, $OD_1$ and $OD_2$ are constants, corresponding to the optical densities associated with different groups of atoms. The transmitted probe intensity, $I$, satisfies the following equation,

$$I(\theta) = I_0 e^{-OD(\theta)} = I_0 e^{-OD_0} e^{-OD_1 sin^2\theta - OD_2 sin^4\theta} . \qquad (1)$$

The transmission dependence of the probe light on $\theta$ is studied with the experimental setup shown in Figure 10. We first rotate the magnetic field in the x-z plane while keeping its magnitude constant. The transmitted probe beam is detected by a photodiode and the photo current, amplified by a trans-impedance amplifier, is recorded. The DC photodiode signal as a function of $\theta$ is shown as dots in Figure 12. The magnetometer is on during the measurement.

According to Equation (1), we fit the data with the following function:

$$y = A * \exp\left[-B * sin^2(\theta - \theta_0) - C * sin^4(\theta - \theta_0)\right]. \qquad (2)$$

An offset in the polar angle, $\theta_0$, is added to the fitting function in order to compensate for any systematic error in $\theta$. The fitting result is plotted as the red curve in Figure 12. As can be seen, the theoretical model agrees well with the experimental data. We also rotate the magnetic field in planes other than x-z and obtain similar results.

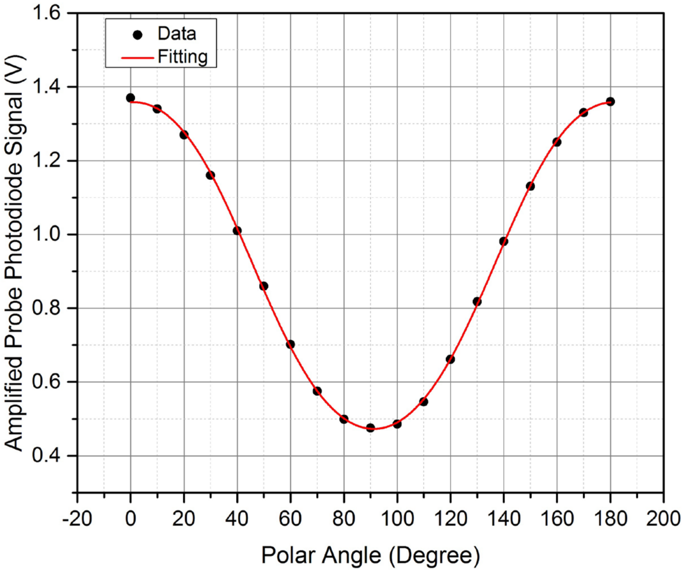

Figure 12 Transmitted probe light DC signal as a function of the polar angle. The magnetic field vector is in the x-z plane. The red curve is the fitting to the experimental data, represented by dots.

The probe DC signal only depends on the polar angle of the magnetic field, not its magnitude. To verify this, we conduct similar experiments in magnetic fields of different strengths. The results are shown in Figure 13. As expected, the magnitude of the magnetic field does not affect the transmitted probe light DC level. The slight disagreement is likely due to the error in the polar angle. Even though we can generate precise Bx, By and Bz with state-of-the-art current sources, there may be changing stray magnetic fields inside the shield can, which affect the actual polar angle during the measurement. The cell temperature is not actively stabilized in the experiments conducted in the benchtop setup, possibly contributing to the error seen in Figure 13. According to our experimental results presented above, the probe DC transmission signal can be used to measure the polar angle of the magnetic field.

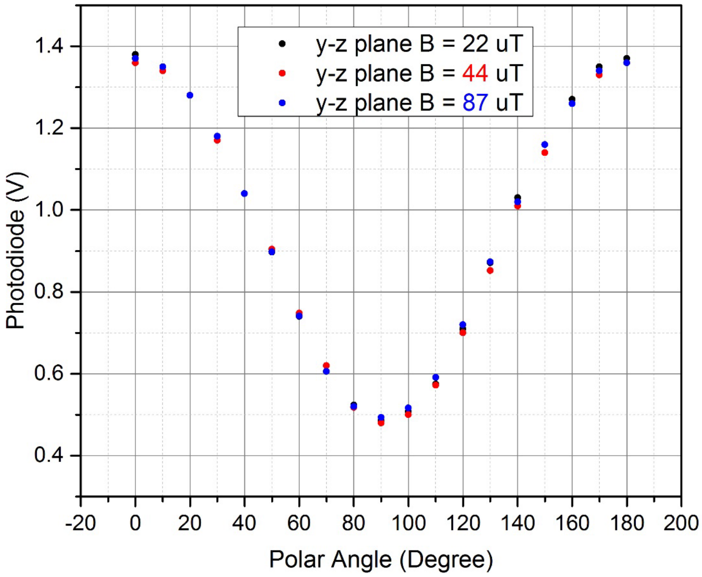

Figure 13 Transmitted probe DC as a function of polar angle of the magnetic field. Black, red and blue dots represent results at B of 22 µT, 44 µT and 87 µT, respectively. The slight difference is likely due to the inaccuracy of polar angles and the fluctuation in the cell temperature.

### 1.1.2. Noise in the polar angle measurement

To investigate the noise in the polar angle measurement using the probe DC transmission, we record the signal for 5 minutes and calculate its Allan Deviation [6]. The Allan Deviation at 50° polar angle is shown in Figure 14. As seen, with about 0.1 second integration time (10 Hz sample rate), the Allan Deviation of the probe DC is less than 0.1 mV. At 50° polar angle, the DC/polar angle calibration slope according to Figure 12 is roughly 16mV/degree. Therefore, a 0.1 mV variation in the probe DC will lead to about 0.006° noise in the polar angle measurement, which is very sensitive. In fact, even at 88° polar angle, the slope is still 0.9mV/degree. A sensitivity of 0.1° in the polar angle can still be achieved with the 0.1 mV noise in the probe DC.

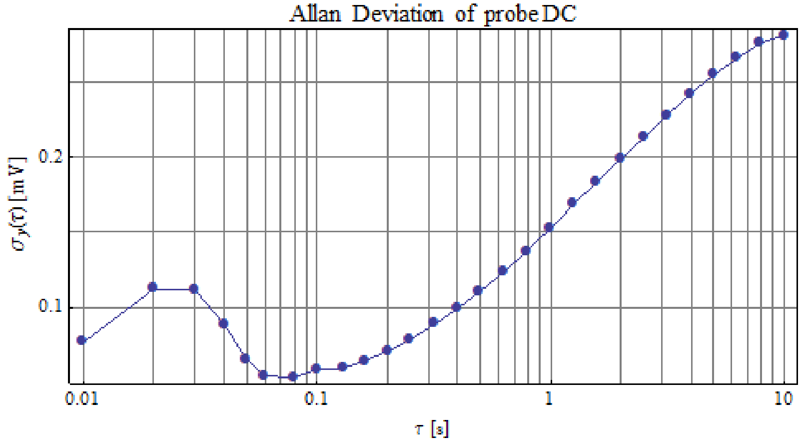

Figure 14 Allan Deviation of the probe DC transmission at $50^o$ polar angle.

### 1.1.3. Dynamic response of the polar angle measurement

So far, all the measurements discussed above were done in steady state where the magnetic field does not change its relative direction or magnitude. In most mobile applications, however, the polar angle of the magnetic field will change. Here we present the dynamic response of the probe DC method to a changing magnetic field.

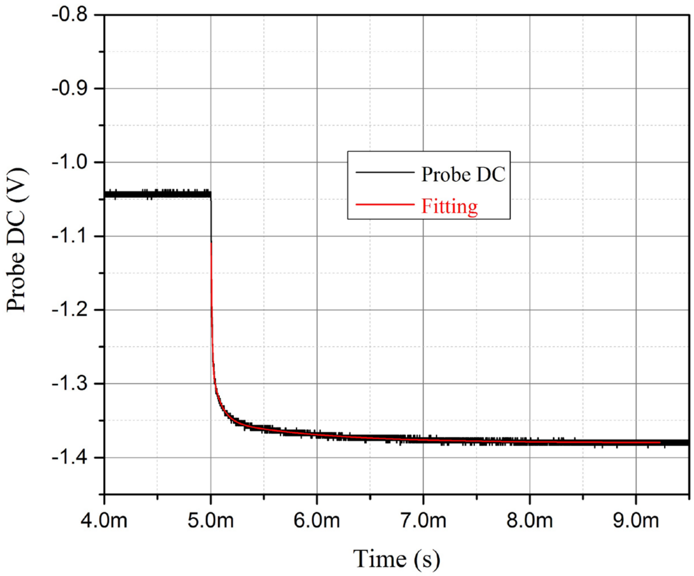

Figure 15 Dynamic response of the probe DC to a sudden change of the B field direction. Polar angle changes from $45^o$ to $0^o$ at t = 5 ms.

As we discussed before, the probe DC signal is independent of the magnitude of the magnetic field. We further confirm this by monitoring the DC signal while applying a magnitude change to the magnetic field. No change is observed in the DC signal. In order to generate a sudden change in the direction of the B field, we initially apply fields in both x and z direction, Bx = 20 μT and Bz = 20 μT. At t = 5 ms, Bx is switched off in less than 50 μs. Figure 15 shows the response of the probe DC signal when the Bx is switched off. The curve cannot be modeled with an exponential function with a single time constant. Instead, three time constants are required, with the longest time constant being 950μs. Hence, the probe DC signal responds to a change in the B field direction with bandwidth greater than 100 Hz. Considering that it is unlikely that the polar angle of the B field will vary at a rate beyond 100 Hz in practical applications, the fundamental dynamic response of the probe DC method is not expected to limit the B field angle measurements.

#### 1.1.4. Discussion

There are two major issues with the polar angle measurement using the probe DC method. First, the probe DC signal is symmetric with respect to $\theta = 90°$. Therefore, based on the probe DC signal only, the polar angle is not unique. The other problem is that the response of the probe DC to $\theta$ around 90° is flat, as seen in Figure 12, leading to a poor sensitivity of this method. For $\theta$ close to 0° or 180°, the sensitivity is also poor. However, this is the dead zone for the magnetometer. In practice, the magnetometer would never be operated close to this orientation.

### 1.2. Extraction of polar angle from the probe light shift

#### 1.2.1. Efficacy of the method

To overcome the issues associated with the probe DC method, we consider the following supplementary method. Circularly polarized light causes a slight shift of energy levels of atomic ground states, equivalent to a fictitious magnetic field being applied along the light propagation direction [7]. The total effective magnetic field, which is measured by the magnetometer, is given by the vector sum of real magnetic field $\boldsymbol{B}$ and the fictitious magnetic field $\boldsymbol{B_k}$. In general, $B_k \ll B$. The effective magnetic field can be approximated by $B + B_k \cos\theta$. $B_k$ depends on the wavelength of the light. If the probe laser optical wavelength is dithered at a frequency $f$ by adding a small oscillating current to the laser drive current, $B_k$ will also develop an oscillating component with the same frequency $f$, $B_k = B_k^0 + B_k^1 * \sin(2\pi f t)$. When the measured magnetic field is demodulated at the frequency $f$, component $B_k^1 \cos\theta$ can be extracted. Since $B_k^1$ is a constant to the first order, the value of $B_k^1 \cos\theta$ gives us a measurement of $\theta$.

To implement this method, we inject a 2 kHz signal in the probe laser current. The signal dithers the laser wavelength by about 0.1 pm. We then demodulate the magnetometer output at the 2 kHz dither frequency. The phase of the demodulator is set such that the y-component output is maximized at 160° polar angle. We rotate the magnetic field (with the same magnitude) in both x-z and y-z plane. At each polar angle, the y-component output is recorded. The result in x-z plane is shown as black dots in Figure 16. As discussed previously, the data should follow the function $y = A\cos(\theta - \theta_0)$. Here $\theta_0$ is added to compensate for any systematic error in $\theta$. A nonlinear fit of the function to the experimental data yields a good agreement between the theory and the experiment. The fitting result is plotted as the red curve. The discrepancies are mostly due to inaccuracies in setting the actual polar angle. We obtain similar results in the y-z plane.

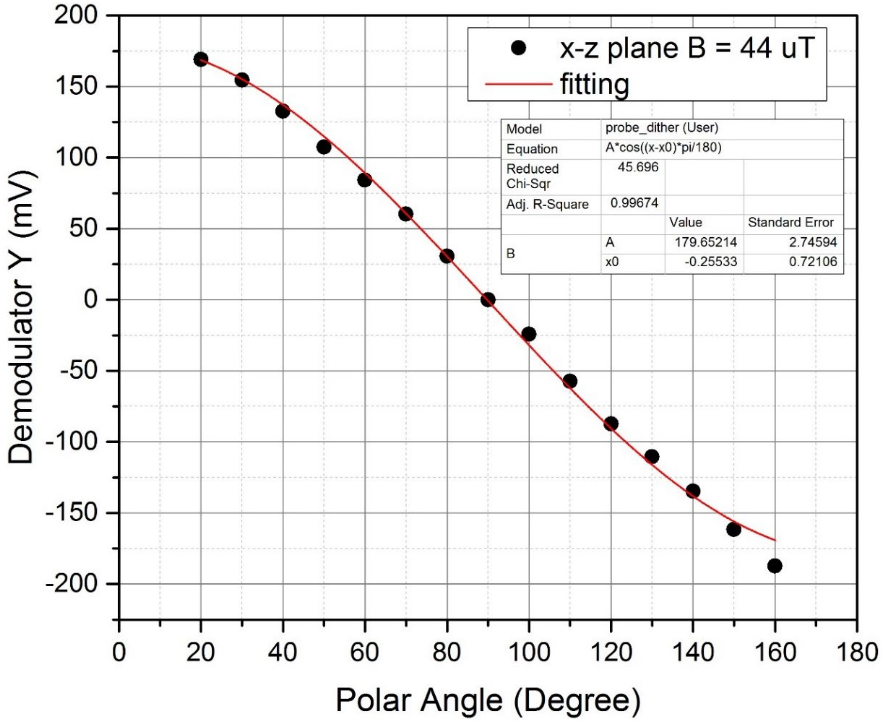

**Figure 16 Response of the light-shift induced magnetic field to the polar angle. The pseudo magnetic field is measured by demodulating the magnetometer output at the frequency dithering the probe current. Y component of the demodulator output is plotted as a function of polar angle.**

### 1.2.2. Noise in the polar angle measurement

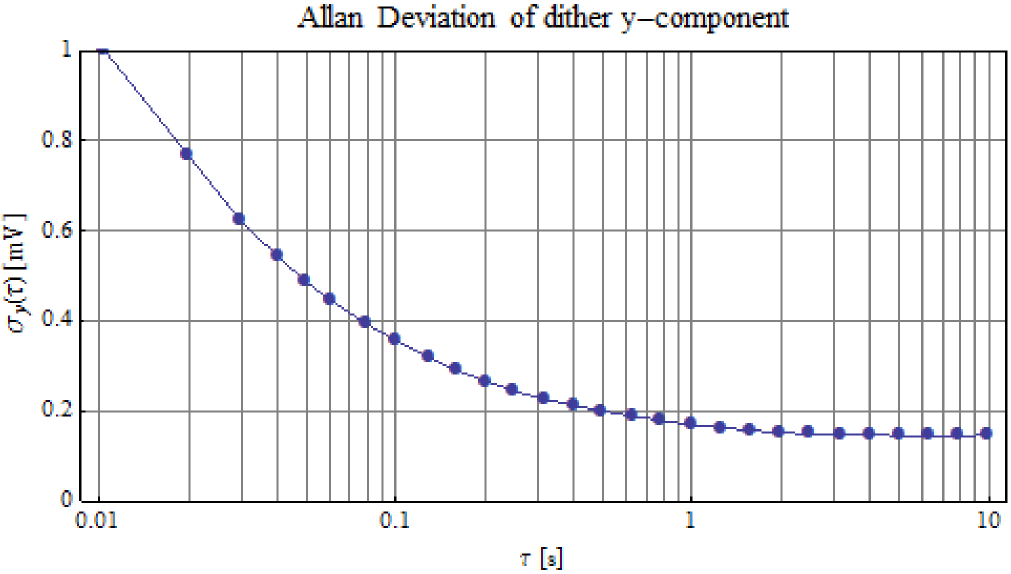

**Figure 17 Allan Deviation of the y-component output at 90º polar angle.**

We record the y-component output for 5 mins and calculate its Allan Deviation. The Allan Deviation for 90° polar angle is shown in Figure 17. As seen, with 0.1s integration time, the Allan Deviation is about 0.4 mV for the y component. According to Figure 16, around 90° polar angle, the slope y/polar is about 2.5 mV/degree. Therefore, a 0.4 mV variation in the y component will lead to about 0.2° noise in the polar angle.

### 1.2.3. Dynamic response of the polar angle measurement

The dependence of the y-component on the polar angle is simply due to the projection of the light-shift induced magnetic field onto the main magnetic field. The response of the projection to the polar angle change is expected to be instantaneous.

### 1.2.4. Discussion

This method relies on the measurement of the magnetic field. When the magnetometer is orientated close to dead zone, the increased noise in the magnetometer output leads to significant increase in noise in the polar angle measurement.

## 1.3. Azimuthal angle measurement

If two scalar magnetometers are used, we can extract some information about the azimuthal angle as well. Assuming that two probes in the magnetometers are aligned as shown in Figure 18 and the relative polar angles, $\theta_1$ and $\theta_2$, are calculated based on the methods presented above, then the azimuthal angle of the magnetic field, $\varphi$, satisfies the following equation:

$$\cos\varphi = \frac{\cos\theta_2 - \cos\theta_1 \cos\theta_0}{\sin\theta_1 \sin\theta_0}. \tag{3}$$

Here $\theta_0$ is the angle separation between the two probes. For $\theta_0 = 90°$, Equation (3) can be simplified. The azimuthal angle is then calculated to be $\varphi = arccos(\cos\theta_2/\sin\theta_1)$. Note that *arccosine* is only defined between 0° and 180°. The azimuthal angle is still undetermined between $\varphi$ and $360° - \varphi$.

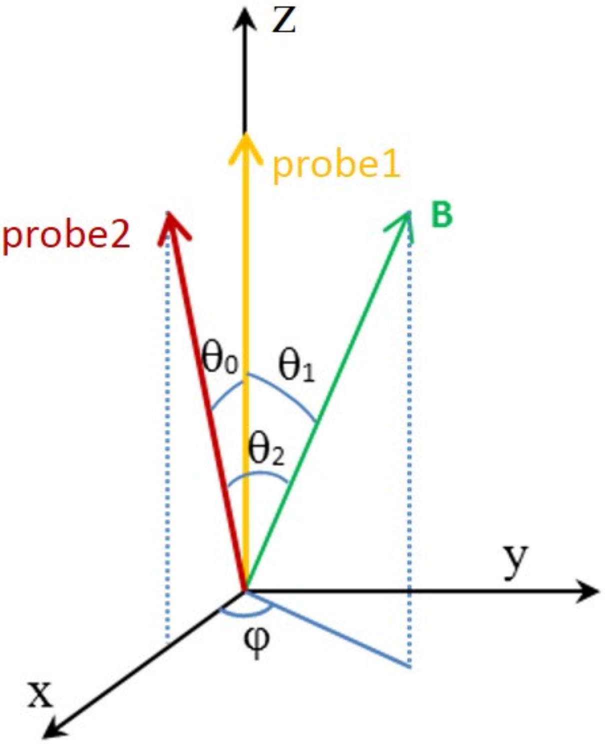

Figure 18 Schematics showing the relative directions of two probes and the magnetic field. The azimuthal angle of the magnetic field can be calculated based on the two polar angles and the angle separation between the two probes.

# 2. Fundamental Slew Rate of the Magnetometer

## 2.1. Magnetic Response of Polarized Atomic Spin

The best solution for achieving the simultaneous operation of a magnetometer and a TDEM system is for the magnetometer to have a fast enough slew rate that it can follow the EM pulses. To investigate the fundamental slew rate of the magnetometer, we first study the dynamic response of polarized atomic spin, which generates the Larmor signal. The experimental steps are as following. Initially the background magnetic field is set at 2 μT in x direction with the large Helmholtz coils. The AOM driving frequency is the resonant Larmor frequency at this field. After a short while (less than 3 ms), macroscopically polarized atomic spins build up and undergo Larmor precession, which is detected by the probe beam. At t = 0, a magnetic field of 10μT, generated by the smaller coils, is switched on in less than 20 μs along the same direction. At the same time, the AOM driving frequency is turned off. The probe photodiode signal, representing the Larmor precession of the atomic spin, is shown in Figure 19 (a). As can be seen, the precession of the atomic spin follows the magnetic field pulse almost instantaneously. In Figure 19 (b), we change the magnetic field from 12 μT to 2 μT at t = 0. A similar result is observed. The demonstrated dynamic response of polarized atomic spin indicates that the slew rate of the atomic magnetometer is not limited by the fundamental physics.

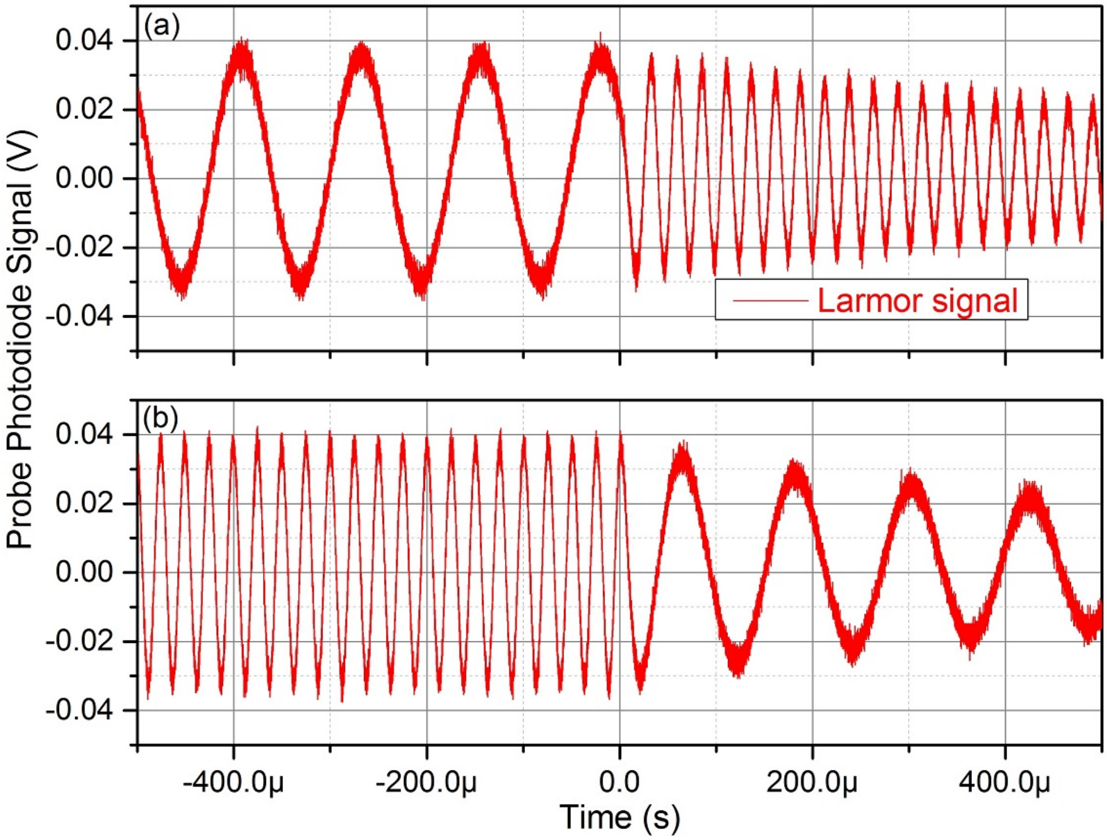

**Figure 19 Magnetic response of polarized atomic spin. The magnetic field in x direction is changed from 2 μT to 12 μT in (a) and from 12 μT to 2 μT in (b) in less than 20 μs at t = 0.**

### 2.2. Tuning of the Phase-Lock-Loop

As we have discussed in the previous section, the atomic spin can react to a sudden change of the magnetic field almost instantaneously. Therefore, the response of a Larmor-based atomic magnetometer is not limited by the fundamental physics. Rather it depends on the detailed implementation of the feedback loop in the driving electronics of the magnetometer. We use a commercially available digital phase-lock-loop (PLL) system as the feedback controller. A typical implementation of the PLL involves three stages, schematically shown in Figure 20. The phase of the input probe photodiode signal is compared with a reference signal, generated by the local oscillator, at the phase detector stage. The output of the phase detector goes through the standard Proportional Integral (PI) controller, whose output controls the frequency of the local oscillator. The feedback loop of the PLL adjusts the frequency of the local oscillator such that there is no phase difference (or a fixed phase difference) between the local oscillator and the Larmor signal. This also ensures that the local oscillator has the same frequency as the input Larmor signal. The response of such a PLL-based magnetometer will depend on the time constants of both the phase detector and the PI controller. We use the smallest time constants (790 ns for the phase detector and 50 μs for the PI controller) for the following experiments in the fundamental slew rate investigation.

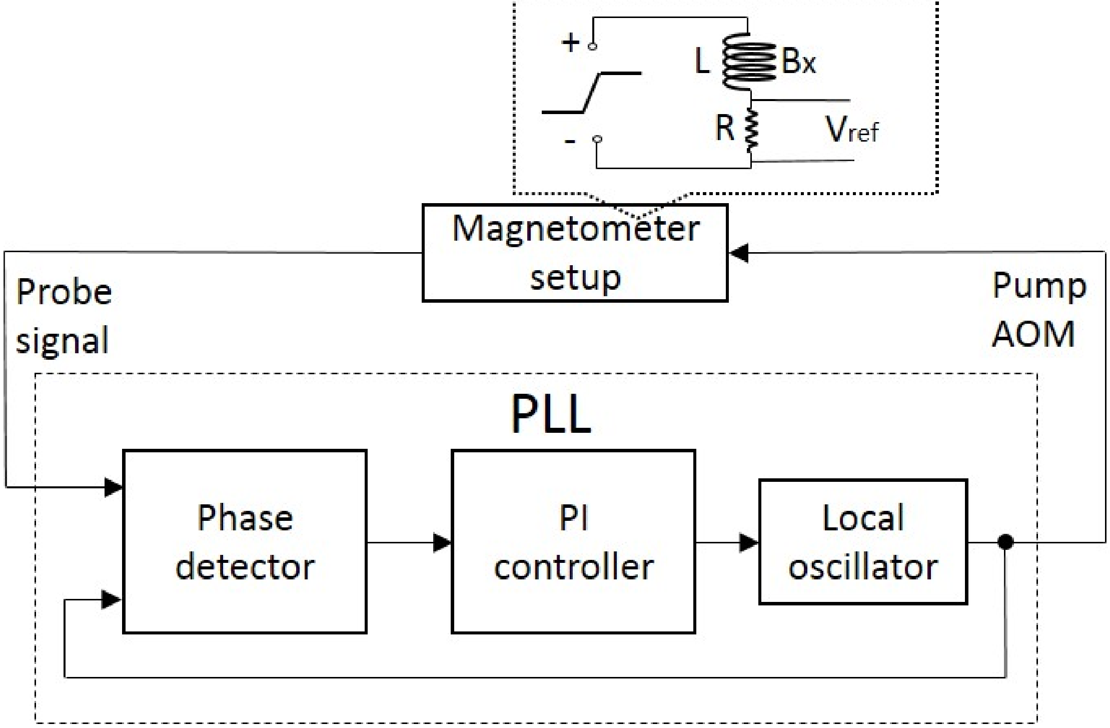

Figure 20 Block diagram showing the implementation of the PLL. The magnetometer setup is shown in Figure 10.

### 2.3. Limit of the Slew Rate of the Magnetometer

We test the slew rate of the magnetometer by ramping up a 50 μT magnetic field in x direction using the small coils as shown in Figure 20. A constant field of 60 μT is also applied along the same direction using the larger coils. We also measure the voltage across a current sensing resistor in series with the small coils. This reference voltage, $V_{ref}$, indicates the actual magnetic field ramp. The ramping time constant is changed. The probe photodiode signal, $V_{ref}$, and the magnetometer output are recorded during the ramp. The results are shown in Figure 21, with the photodiode signal (black curve) and V<sub>ref</sub> (blue curve) given by the left axis and the magnetometer output (red curve) given by the right axis. As can be seen, when the ramp time is more than 200 µs, the magnetometer output tracks the magnetic field ramp very nicely. When the ramp time is shortened to less than 100 µs, the PLL starts to lose lock, shown in Figure 21 (d), where the ramp time is only 90 µs. In this particular case, the magnetometer recovers its operation after the magnetic field is ramped back down to 60 µT. For short ramping time constants (< 100 µs), sometimes the PLL can completely lose the lock and never recover.

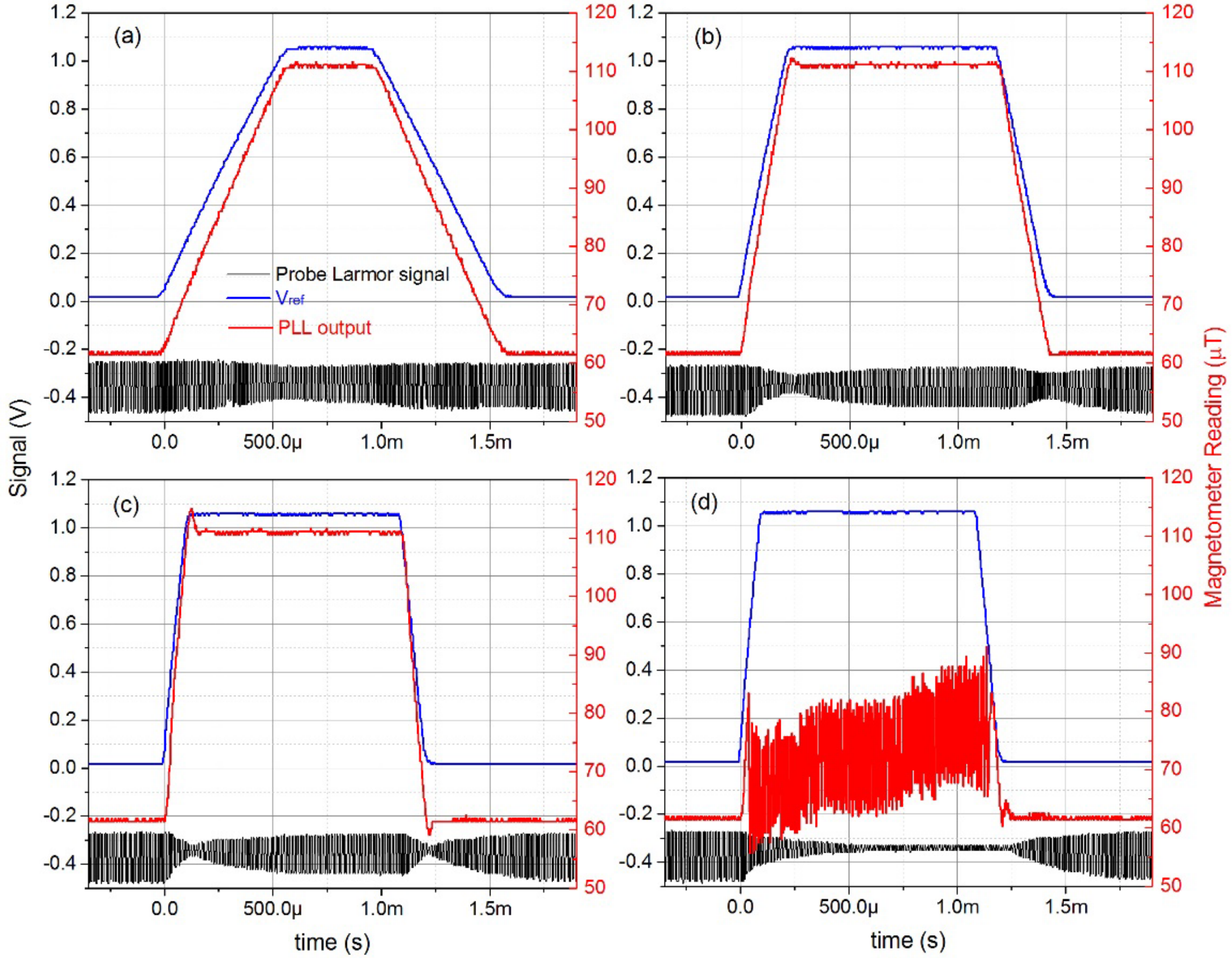

Figure 21 Response of the magnetometer to different rates of change of the magnetic field. (a), (b), (c) and (d) correspond to a 50 µT change in 500 µs, 200 µs, 100 µs and 90 µs, respectively. The photodiode signal (black) and $V_{ref}$ (blue) are given by the left axis and the magnetometer output (red) is given by the right axis.

### 2.4. Bandwidth and Noise of the High-Slew-Rate Magnetometer

We measure the bandwidth of the magnetometer at different magnetic fields. The main magnetic field is set by the large coils in x direction. The small x coils generate an oscillating magnetic field, the frequency of which is swept from 0.1 Hz to 80 kHz while its amplitude is fixed at 50 nT. We record the output of the magnetometer and measure the amplitude of the oscillating field as a function of its frequency. The normalized amplitude vs. frequency curve is plotted in Figure 22 (a). As seen in the plot, the bandwidth of the magnetometer at different magnetic fields is about the same. The hump around 10 kHz is due to the over-tuning of the PLL. The magnetometer noise is also measured by recording the magnetometer output for 5 minutes at a constant magnetic field.

The results are shown in Figure 22 (b). The rise of the magnetometer noise at high frequencies is mainly due to the increase in the PLL gain. We also notice that the low-frequency noise becomes worse at smaller magnetic fields. This is likely due to the small time constant of the PLL phase detector. At lower magnetic fields, the phase detector does not have enough time for averaging over many Larmor cycles, resulting in a larger phase error. Rubidium atoms have twice the gyromagnetic ratio of Cs atoms. This results in twice the Larmor frequency allowing more cycles to be used for the phase measurement. Therefore, Rubidium magnetometers may work better in terms of noise performance.

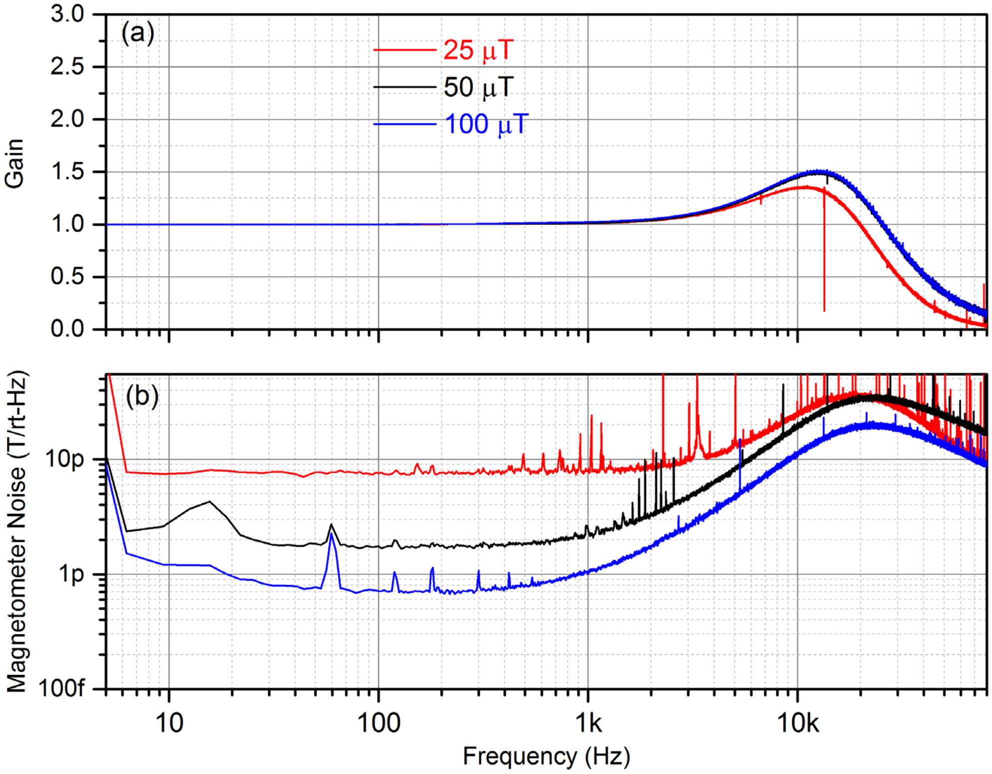

Figure 22 Bandwidth (a) and noise (b) of the high-slew-rate magnetometer at different magnetic fields.

## 2.5. Discussion

We demonstrate a slew rate of 500 μT/ms with a bench-top magnetometer. However, we do not expect that similar slew rates can be achieved with our MFAM sensors. In the miniature sensors, vertical cavity surface emitting lasers (VCSEL) are used to minimize the size and power-consumption of the sensor, at the expense of increased laser frequency noise. MFAM electronics, driving the operation of the sensor, are also noisier than the commercial PLL system. As a result, the MFAM measurement noise is likely to be much worse than that demonstrated in Figure 22 (b), especially around high frequencies. Combined with high PLL gains at high frequencies, it is hard to achieve a stable operation of PLL with MFAM sensors. In addition, many portable TDEM systems generate magnetic pulses exceeding the 500 μT/ms slew rate. Therefore, high-slew-rate portable magnetometers are not likely to be the solution achieving the simultaneous operation of magnetometers with TDEM systems. In the following section, we will investigate the fast-recovery method after the EM pulse is switched off.

# 3. Fast-recovery with a Pre-determined Larmor Frequency

When the EM pulses exceed the slew rate of the magnetometer, the magnetometer loses the track of the magnetic field. A considerable amount of time has to be spent by the magnetometer searching and finding the resonant Larmor frequency again. We believe that the recovery time can be greatly reduced if the searching range is limited and close to the actual Larmor frequency. This hypothesis will be verified in this section. The dependence of the recovery time on the separation between the starting searching frequency and the actual Larmor frequency will also be investigated. As discussed in the previous section, it is unlikely to achieve a bandwidth of exceeding 10 kHz with miniature MFAM sensors. Therefore, we tune the PLL bandwidth to be around 2 kHz for the following experiments. This bandwidth is achievable with actual miniature sensors.

## 3.1. Efficacy of the Method

We set the constant background magnetic field $B_x = 60.5$ μT inside the shield can, corresponding to a resonant Larmor frequency of 212 kHz. Amplitude and phase of the Larmor signal across the resonant Larmor frequency are shown as the black and red curves, respectively, in Figure 23. To investigate the dependence of the PLL settle time on the separation between the starting pump modulation frequency and the actual Larmor frequency, the initial pump modulation frequency is set to be different from the resonant Larmor frequency before the PLL loop is closed. The tested starting pump frequencies are indicated by the blue lines in Figure 23. At t =0, the PLL is enabled.

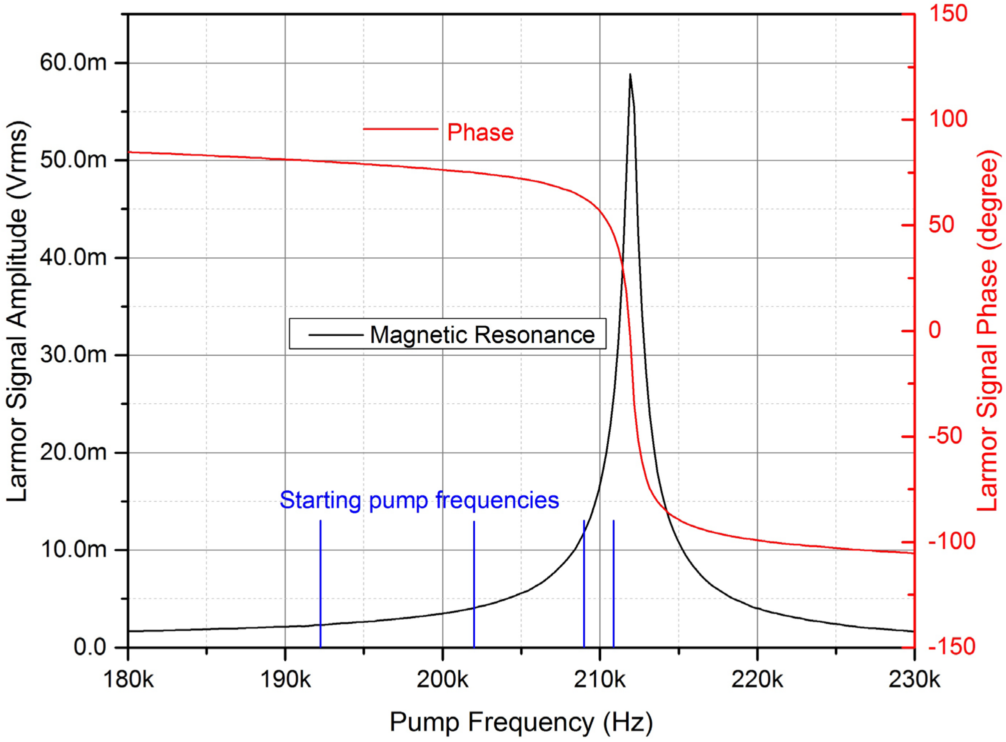

Figure 23 Magnetic resonance signal (black curve), its phase (red curve) and the starting pump frequencies (indicated by the blue lines).

We first set the initial pump frequency to be 1 kHz away from the resonant Larmor frequency, shown as the closest blue line to the magnetic resonance signal in Figure 23. We record both the Larmor signal (black curve) and the magnetometer reading (red curve) around t=0, shown in Figure

24 (a). As can be seen, in less than 1 ms, the magnetometer outputs the correct field reading. Meanwhile the Larmor signal also reaches steady state. Notice that the field reading settles much faster than the signal amplitude because PLL measures the frequency, not the amplitude, of the Larmor signal. We also set the initial pump frequency to be 3 kHz, 10 kHz and 20 kHz away from the resonant Larmor frequency. Corresponding results are shown in Figure 24 (b), (c) and (d), respectively. As expected, the further away the initial pump frequency, the longer it takes for the magnetometer to recover its normal operation. Note that in order to record both the Larmor signal (analog) and the magnetometer reading (digital) at the same time, the digital reading is first converted to an analog signal through a digital-analog converter. The magnetometer reading appears to settle at different values most likely due to the nonlinearity of the converter. The reading range is only 0.4μT in (a) compared with 6.5μT in (d).

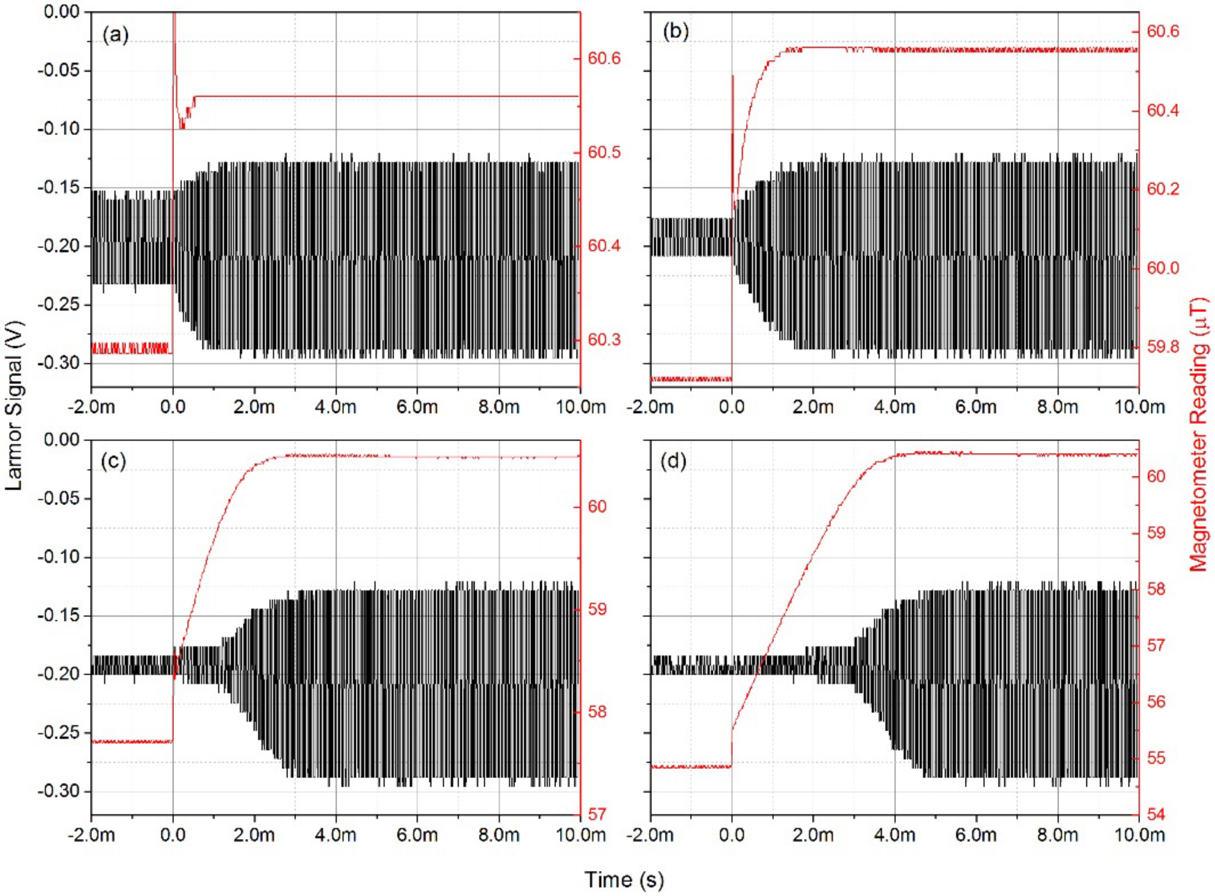

Figure 24 Reading of the magnetometer after the PLL is enabled (red curves). The initial pump modulation frequency is (a) 1 kHz, (b) 3 kHz, (c) 10 kHz and (d) 20 kHz away from the resonant Larmor frequency, corresponding to 4 blue lines in Figure 23. The probe Larmor signal detected by the photodiode is also shown as the black curve.

### 3.2. Fast-recovery after the EM Pulse

The previous experiment verifies that as long as the starting pump frequency is close to the actual Larmor frequency, less than 1 ms recovery time is possible. Therefore, the key to the fast-recovery of the magnetometer is to estimate the actual Larmor frequency. In most practical applications, people are only interested in the magnetic field measurements after the EM pulses are switched off. Since typical EM pulses last less than 10 ms, the Larmor frequency before an EM pulse should be a good estimation of the Larmor frequency after the EM pulse. In this case, we can use the actual magnetometer reading (multiply by a constant ~3.5Hz/nT) before the EM pulse as the starting pump frequency after the EM pulse.

With the commercial PLL system, we can limit the PLL range centered on a user-defined frequency. By applying this limitation, we can control the separation between the initial pump frequency and the actual Larmor frequency after the EM pulse is switched off. In the following experiment, we set the constant background magnetic field along polar 30° angle (Bz = 53 µT and Bx = -30 µT with large coils). This field orientation is right outside the dead zone of the magnetometer. Therefore, we expect the magnetometer to work even better in other background field directions. The center PLL frequency is set to be 210 kHz, corresponding to the Larmor frequency of the background magnetic field. The EM pulses are generated by the small x coils with amplitude of 220 µT and ramping time of 10 µs, well exceeding the slew rate of the magnetometer. The pulse is at 50 Hz repetition rate with 25% duty cycle. During the EM pulses, $V_{ref}$ and the magnetometer output are recorded. The results are shown in Figure 25, with the $V_{ref}$ (blue curve) given by the left axis and the magnetometer output (red curve) given by the right axis.

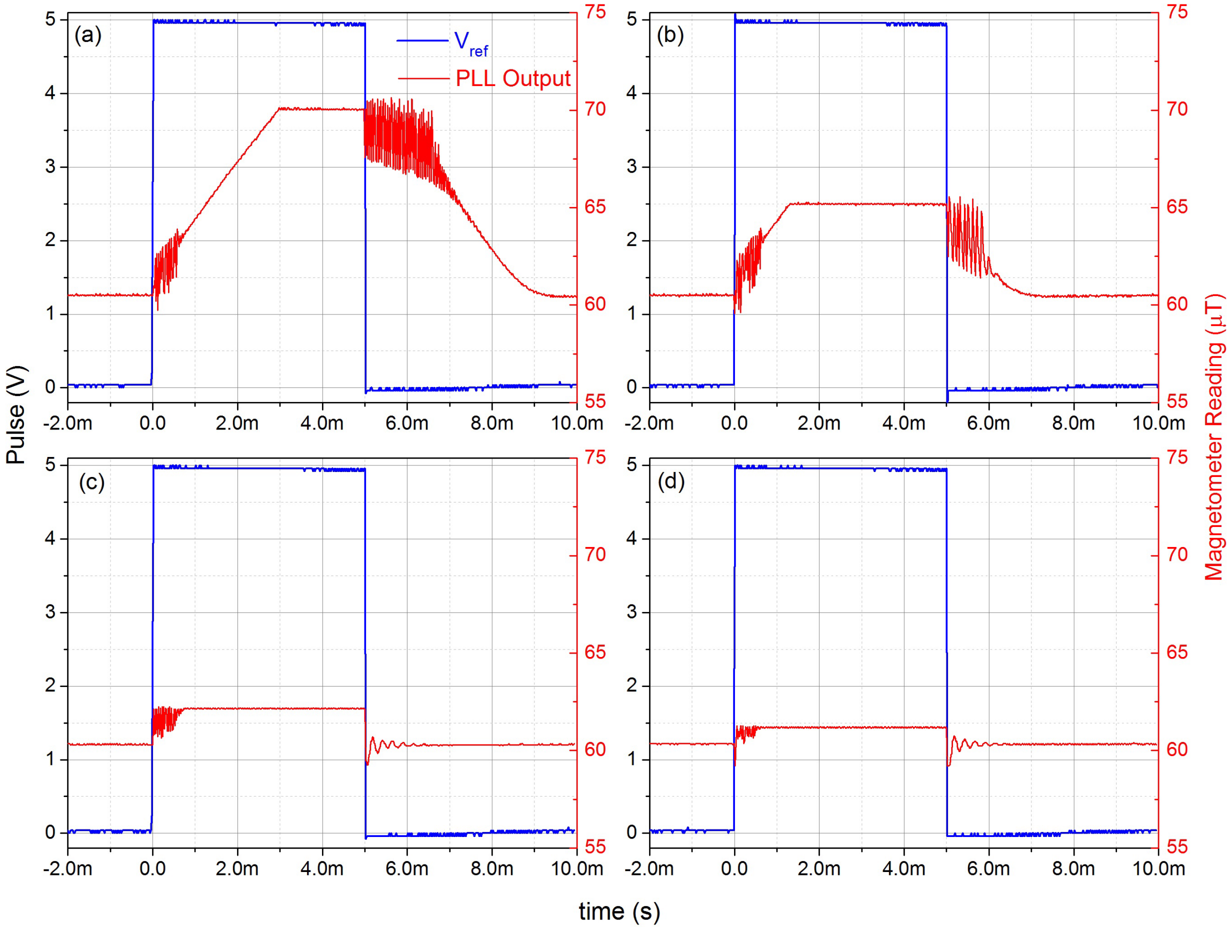

**Figure 25 Fast-recovery of the magnetometer operation after EM pulses. The PLL range is set at (a) +/-35 kHz, (b) +/-17.5 kHz, (c) +/-7 kHz and (d) +/-3.5 kHz, from a center frequency of 210 kHz. The background magnetic field is set at 30° polar angle, Bz = 53 µT and Bx = -30 µT, with large coils. The magnetic pulse is generated by the small x coils with amplitude of 220 µT and ramp time of 10 µs.**

In Figure 25 (a), the PLL frequency range is set to be +/- 35 kHz, corresponding to a magnetic field range of about +/- 10 µT. As seen in the plot, when the magnetic field pulse is switched on at t = 0, indicated by the $V_{ref}$ curve, the PLL loses the track of the magnetic field. After about 3 ms, the PLL reaches the max range. The PLL frequency stays constant until the pulse is switched back off at t = 5 ms. At this moment, the pump frequency, controlled by the PLL, is about 35 kHz away from the actual Larmor frequency. As can be seen, it takes almost 5 ms for the magnetometer to produce valid measurements again after the pulse is switched off. In Figure 25 (b), (c) and (d), we set the PLL frequency range to be +/- 17.5 kHz, +/- 7 kHz and +/- 3.5 kHz, respectively. Compared with the result in Figure 25 (a), when the initial pump frequency is closer to the actual Larmor frequency, shown in Figure 25 (b), the recovery of the magnetometer operation is faster. We verify that the damped oscillation in the magnetometer reading after the pulse is switched off, shown in Figure 25 (c) and (d), is a real magnetic signal. This is due to the under-damping of the induced current in the large coil circuit. By adding a resistor in series with the large coils, we can change the large coil circuit from under-damping to over-damping. The change of behavior in the induced current is observed by the magnetometer.

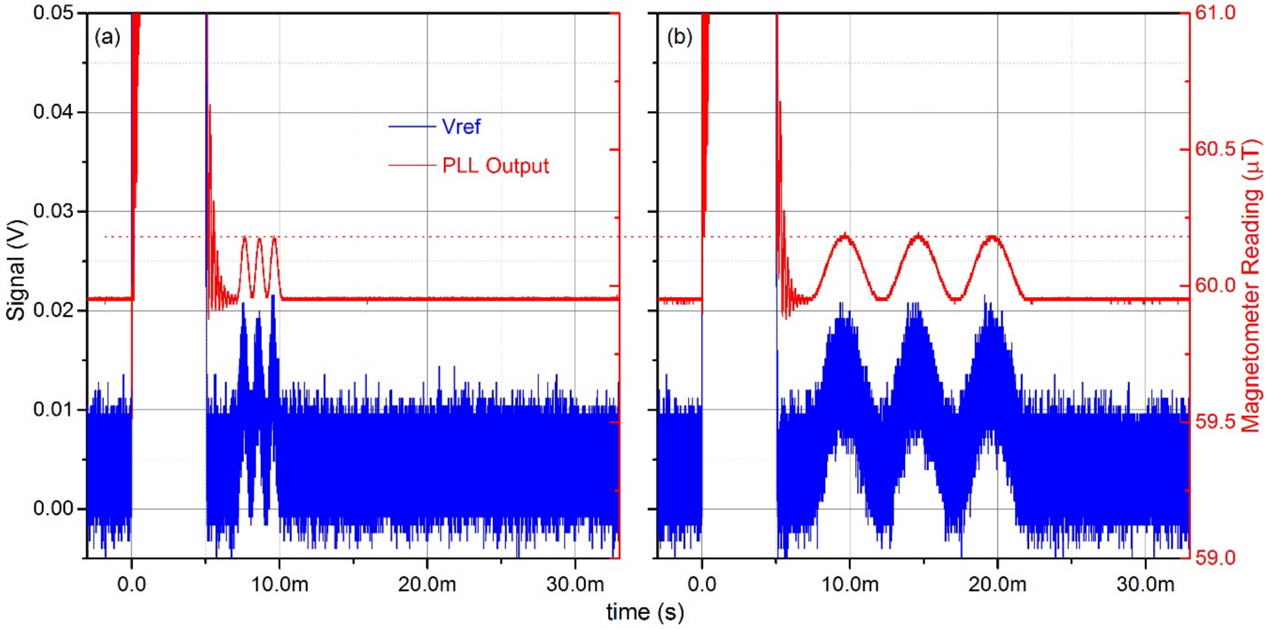

**Figure 26 Measurement of a small oscillating signal 2ms after the magnetic pulse is switched off. The frequency of the signal is (a) 1 kHz and (b) 200 Hz.**

We also apply a small oscillating signal, about 200 nT peak to peak in the projected background field direction, 2 ms after the EM pulse is switched off. The EM pulse is at 20 Hz repetition rate now. The magnetometer reading and $V_{ref}$ are recorded and shown as the red and blue curves, respectively, in Figure 26. As can be seen, the magnetometer can respond to the small signal after the EM pulse is switched off. The signal frequency is changed from 1 kHz to 200 Hz from Figure 26 (a) to (b). The measured signal amplitude does not change, indicating a magnetometer bandwidth of well above 1 kHz.

### 3.3. Bandwidth and Noise

We also measure the bandwidth and the noise of the magnetometer under the current PLL conditions. The results are shown in Figure 27. Compared with the results shown in Figure 22, the magnetometer performance is not affected by the magnitude of the background magnetic field.

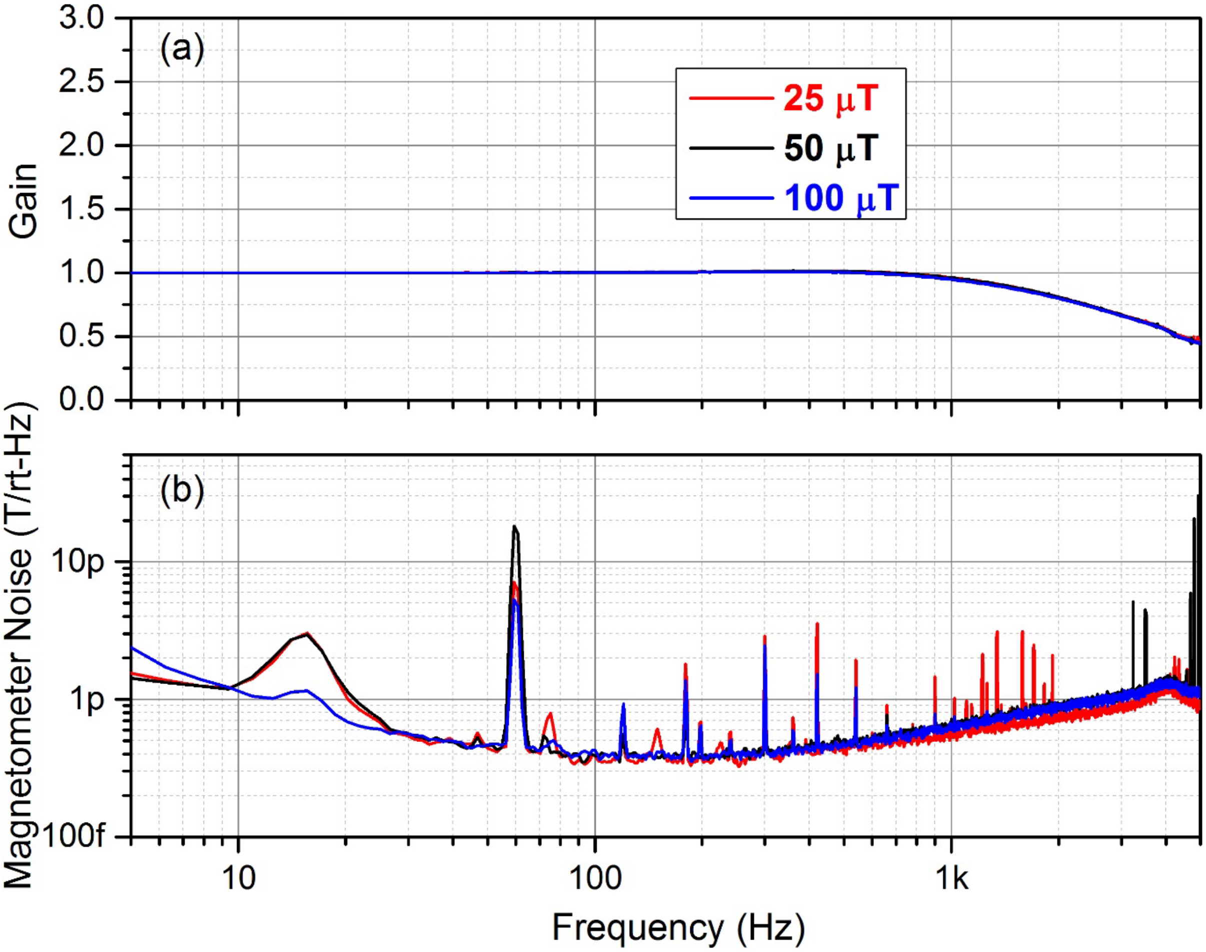

Figure 27 Bandwidth (a) and noise (b) of the magnetometer at different background magnetic fields.

### 3.4. Detection of the EM Pulses

In practical applications, we need a signal detecting the onset and the end of EM pulses so that only the valid magnetometer readings are reported. In principle, the TDEM system can output a synchronized electronic pulse to be used by the magnetometer as the signal. However, this increases the complexity of electronic designs for both the TDEM system and the magnetometer. Therefore, it is preferred that the magnetometer can detect the EM pulse by itself. After exploring several candidates, we identify the probe Larmor amplitude to be the signal detecting the EM pulses. When the EM pulse is switched on, the Larmor amplitude is quickly reduced to zero since the PLL cannot follow the EM pulse. After the EM pulse is switched off, the Larmor amplitude will increase when the pump frequency is close to the actual Larmor frequency.

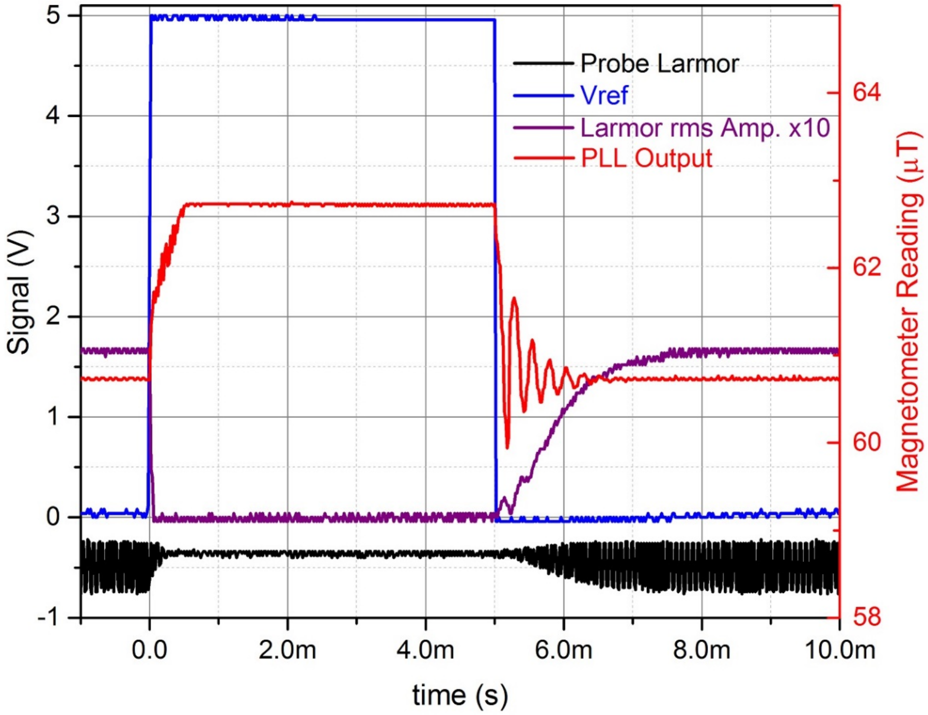

Figure 28 Larmor amplitude in root-mean-square multiplied by 10 (purple curve) during the EM pulse.

We record the root-mean-square (rms) Larmor amplitude (measured by demodulated the probe photodiode signal at the PLL output frequency) during the EM pulse. The rms Larmor amplitude (purple curve) together with $V_{ref}$ (blue curve) and the probe Larmor signal (black curve) are plotted in Figure 28 and given by the left axis. The rms amplitude is multiplied by a factor of 10 in order to be on the same scale as the other signals. The magnetometer reading (red curve) is also plotted, given by the right axis. As seen in the plot, a threshold in the Larmor amplitude can be used to indicate the onset and the end of the EM pulse.

### 3.5. Fast-recovery during the EM Pulse

For fast-recovery during the EM pulse to work, we need to combine the angle measurement results, developed in the first objective, with the fast-recovery method. This is hard to implement with the commercial PLL system due to the limited options in the PLL setup. Therefore, we will not explore the fast-recovery during the EM pulse with the bench-top magnetometer. Instead, it will be implemented and tested with the MFAM sensors.

### 3.6. Discussion

We demonstrate, with a bench-top magnetometer, that less than 1 ms magnetometer recovery time is possible after the EM pulse is switched off. We also show that the Larmor amplitude can be used as an internal signal detecting the EM pulse. This greatly simplifies the design of a practical magnetometer-TDEM system since now they can be operated independently. With the above investigation, we are ready to implement the fast-recovery method using MFAM sensors.

# 4. Quasi-DC Magnetic Field Excitation

## 4.1. Theoretical Model

To study the magnetic response of UXOs to background magnetic fields along different directions, we first establish a theoretical model simulating the induced magnetic field generated by spheroids, which are good approximations of UXOs. The model is similar to the one described in detail in reference [8], where actual field data is also shown to support the theoretical model.

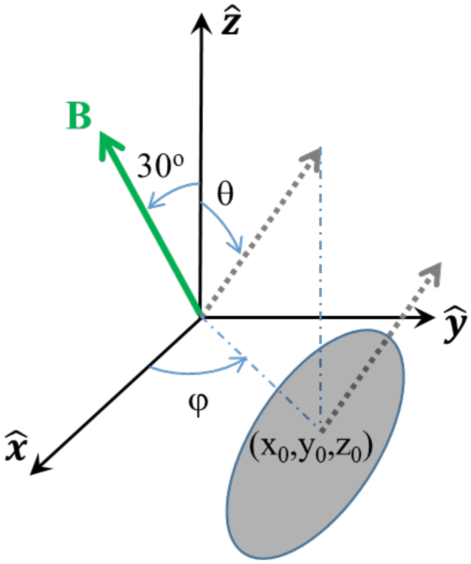

Figure 29 Geometry of a spheroid in a background magnetic field.

The spheroid is characterized by eight parameters, ($x_0$, $y_0$, $z_0$, θ, φ, $a$, $e$, μ). The location of the spheroid is given by ($x_0$, $y_0$, $z_0$) with ground at $z = 0$ and negative $z$ indicating underground. The spheroid has a diameter of $a$, aspect ratio of $e$ (length = $a \times e$) and permeability of μ.The symmetric axis of the spheroid points in the (θ, φ) direction, with θ being the polar angle and φ being the azimuth. The spheroid in the xyz coordinate is schematically shown in Figure 29. Note that definitions of θ and φ are different from reference [8]. The background magnetic field parameters can be changed as well. For simplicity, in the following sections, it has a magnitude of 50 μT and in (30°, 0) direction, unless otherwise noted. With the spheroid parameters and the background magnetic field, the induced magnetic dipole moment can be calculated. The dipole approximation is valid as long as the distance between the spheroid and the observation point is greater than a few body lengths of the spheroid. With the induced dipole moment and the background magnetic field, the magnitude of the combined field can be computed at any location. Detailed calculations can be found in reference [8].

## 4.2. Magnetic Anomaly Generated by UXO

With the theoretical model, we can simulate the magnetic anomaly generated by an UXO. The permeability μ can be expressed as $\mu = \mu_r \mu_o$, where $\mu_r$ is the relative permeability and $\mu_o$ is the permeability of free space. Once the relative permeability exceeds a few hundred units, the induced magnetization becomes virtually independent of μ [8]. Steel typically has $\mu_r$ of several hundred or higher. Therefore, we assume $\mu_r = 200$ for the rest of the simulation and confirm that change in $\mu_r$ does not affect the results as long as $\mu_r > 100$.

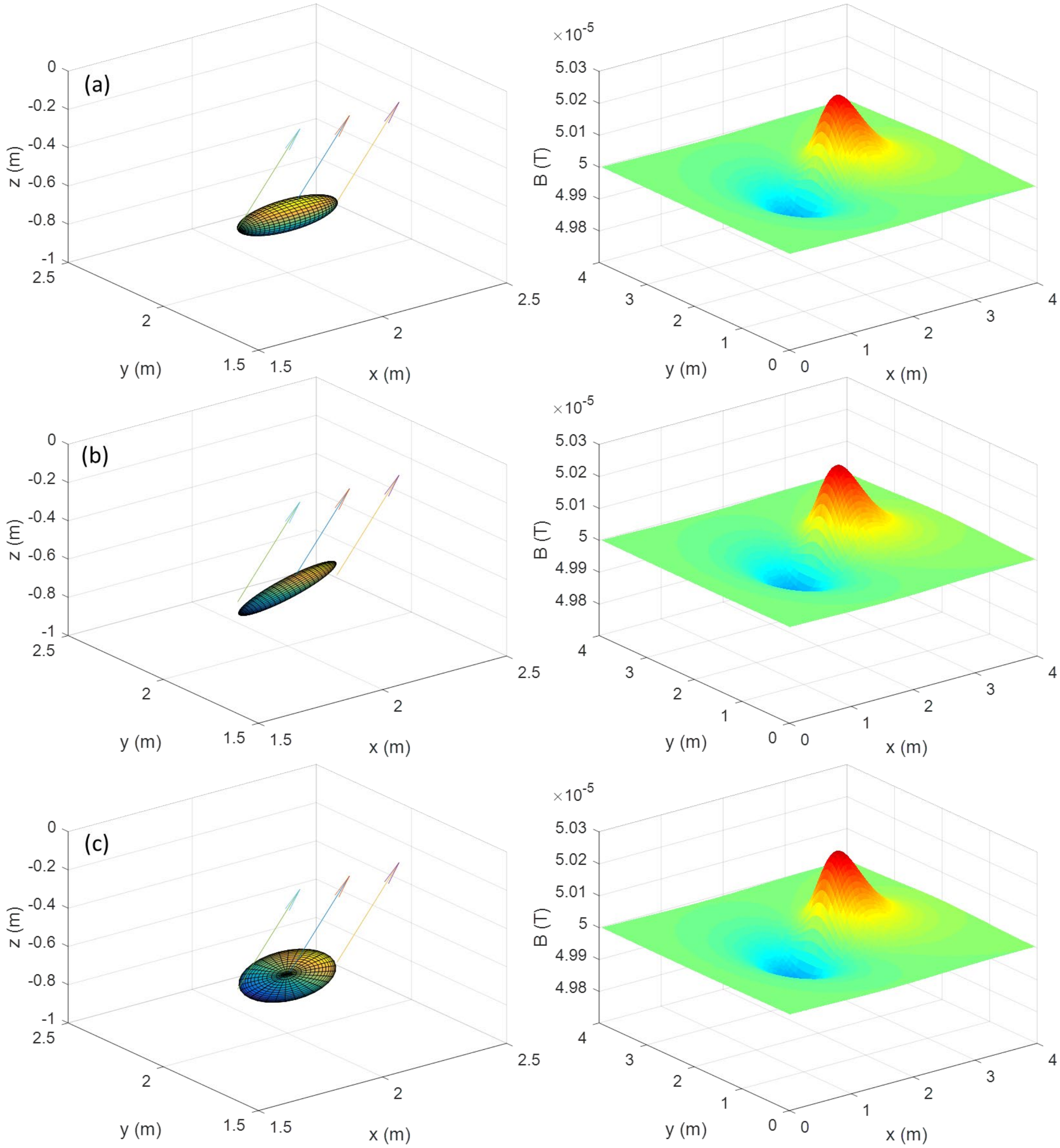

**Figure 30 Simulated magnetic anomalies (right picture) on the ground, z = 0, from different objects buried 0.7 m deep, shown in the left picture. The arrows represent the background magnetic field.**

In Figure 30, we plot the simulated total magnetic field at z = 0 (on the ground) as a function of x and y (right picture) for different objects. In Figure 30 (a), the field is generated by a spheroid with a diameter of $a$ = 13.8 cm, aspect ratio of $e$ = 2.82, located at $x_0$ = 2 m, $y_0$ = 2 m and $z_0$ = -0.7 m and a symmetric axis pointing in $\theta = 87.2^{o}$ and $\varphi = 0^{o}$ direction. The spheroid is shown in the left plot with arrows representing the background magnetic field. The magnetic field profile shown in the right side of Figure 30 is a typical magnetic anomaly generated by a magnetic dipole not near vertical direction. The anomaly plot can reveal much information regarding the dipole. The plot has a minimum spot and a maximum spot with the direction of the line connecting the two spots determined by the azimuth of the dipole. The magnitude and polar angle of the dipole affects the absolute amplitude and the relative amplitude of the two spots. The separation between the two spots is closely related to the depth of the dipole.

### 4.3. Ambiguity in Magnetic Survey

Although magnetic survey method can provide valuable information regarding the target of interest (ToI), it is not as accurate, compared with the EM method, in UXO discrimination and classification. The fundamental reason is because many parameters of ToI greatly affect the induced magnetic field, such as size, aspect ratio and orientation. As a result, dramatically differently shaped objects can generate very similar magnetic anomalies at certain orientations in the external magnetic field. In Figure 30 (b) and (c), we show two objects at the same location as the one in (a) but with different other parameters given by (*a* = 8.2 cm, *e* = 5, θ = 70.5°, φ= 0°) and (*a* = 32.7 cm, *e* = 0.06, θ = 156.6°, φ= 0°), respectively. As seen in Figure 30, the magnetic anomalies generated by these 3 objects are almost identical. If one such data set is obtained and all 3 objects are known to be present around the survey area, it is impossible to perform UXO discrimination and classification based on the magnetic method.

### 4.4. Quasi-DC Magnetic Field Excitation

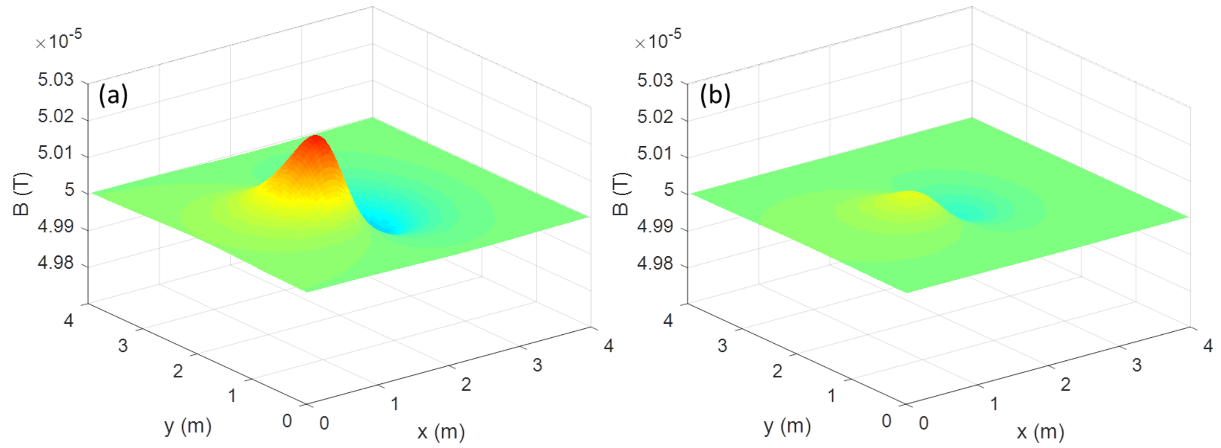

**Figure 31 Simulated magnetic anomalies with an additional 50 μT DC magnetic field along –x direction. (a), (b) correspond to two objects shown in Figure 30 (a) and (b), respectively. All other conditions are exactly the same as those in Figure 30.**

For objects with aspect ratios different from 1 (spherical object), the induced magnetic field depends strongly on the relative orientation of the object with respect to the external magnetic field. Even though two differently shaped objects may generate similar magnetic anomalies at certain orientations, much different results can be expected if the relative orientations of the objects with respect to the background field are varied, which can be realized by adding a DC magnetic field. To obtain more information, both amplitude and direction of the DC magnetic field can be changed. If continuous, the change should be slow enough that the target response can be considered static. We apply another 50μT magnetic field along – x direction to the simulations shown in Figure 30. All other conditions are exactly the same. Under the new background field magnetic anomalies corresponding to two objects shown in Figure 30 (a) and (b) are plotted in Figure 31 (a) and (b), respectively. As can be seen, the magnetic anomalies are indeed much different this time.

### 4.5. Discussion

There is one major challenge when applying the quasi-DC magnetic field excitation method in practical applications. The additional magnetic field not only alters the total background field experienced by the target, but also changes total fields at sensor locations. Any instrument orientation variation, which is almost inevitable in practice, will lead to change in total magnetic fields measured by sensors. This motion-induced field amplitude fluctuation can easily overwhelm the magnetic anomalies generated by the target. It is not likely to obtain results shown in Figure 31 in practical applications. In principle, extra smaller coils can be excited to cancel the quasi-DC magnetic field at sensor locations. However, it is not obvious whether it is possible to achieve field cancellation at multiple sensor locations without generating too much field gradient which is detrimental to robust sensor operation. More simulation results will be presented to assess possible solutions overcoming this challenge.

## 5. Low Frequency AC Magnetic Field Excitation

As demonstrated in Figure 21, the magnetometer is capable of tracking rapid varying magnetic fields. This capability enables us to explore a new method of detecting and discriminating targets using magnetometers.

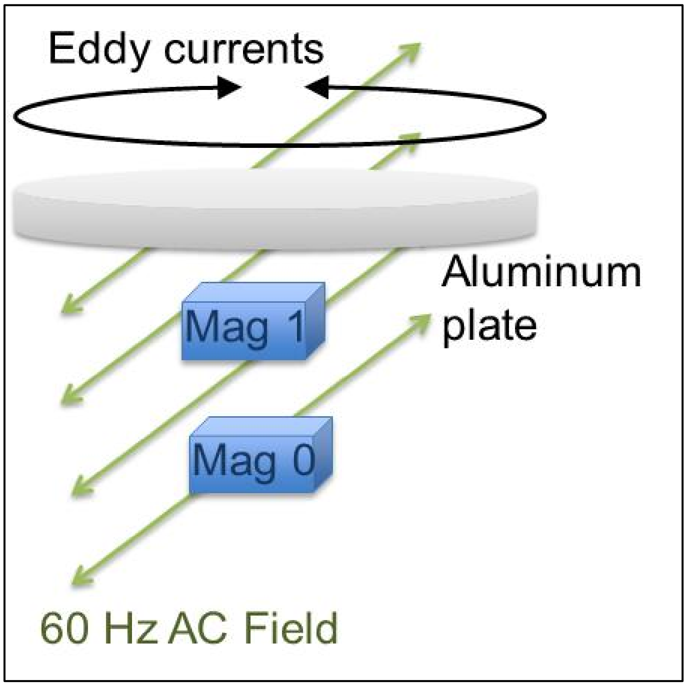

Figure 32 Low frequency AC magnetic field excitation method.

The new method can be illustrated by Figure 32. Assuming two magnetometers are placed near an aluminum plate with one sensor closer to the plate than the other. A low frequency AC magnetic field, such as a 60 Hz oscillating field, is present in the background. Without the aluminum plate, the 60 Hz components in two magnetometer outputs have the same phase. With the aluminum (or any metal) plate, an eddy current is induced by the oscillating magnetic field. The eddy current has the same frequency as the exciting AC field. But its amplitude and phase are determined by many factors such as the frequency of the exciting field, the conductivity of the material as well as the size and shape of the target. Due to the eddy current, a secondary oscillating magnetic field is generated with the same frequency as the main AC field but a slightly different phase. As a result, the overall 60 Hz signal at sensor 1 location is phase shifted from that at sensor 0 since the secondary field amplitude decreases fast away from the plate. Based on this theory, we should be able to use the phase difference between two sensors as a signal to detect metal targets.

Note that an important parameter in the eddy current theory is the skin depth $\delta$, which describes how deep the AC magnetic field penetrates into the material. The skin depth is given by:

$$\delta = \sqrt{\frac{2}{\omega\mu\sigma}} \qquad (4)$$

Here $\omega$ is the angular frequency of the field, $\mu$ and $\sigma$ is the permeability and conductivity of the material, respectively. From the skin depth equation, it is easy to conclude that the lower the excitation frequency the deeper the field penetrates into the material. Due to the high permeability of ferrous material, the skin depth of magnetic targets is much smaller than those of non-magnetic targets. In addition, the magnetic hysteresis phenomenon will also alter the phase of the secondary field. Therefore this new method may not work as well with magnetic targets.

## 6. Advanced Signal Extraction in Scalar Atomic Magnetometers

In our Micro-Fabricated Atomic Magnetometer (MFAM) sensor, we replaced the DBR lasers shown in Figure 10 with vertical cavity surface emitting lasers (VCSELs). The optical wavelength of the VCSELs can be dithered at the Larmor frequency through laser current modulation, thus eliminating the need for AOMs. With these changes, we were able to integrate the bench top magnetometer into a sensor package less than 20 cubic centimeters in volume. All signals generated by the sensor are analyzed by a field-programmable gate array (FPGA). The DSP programmed within the FPGA records the probe DC signal and calculates the demodulated probe light-shift amplitude. The MFAM sensor outputs both the probe DC level and the probe light-shift amplitude at a rate of 100 samples per second. Note that the magnetic field output of the MFAM is still at 1000 samples per second. In the following, we use the MFAM sensors to investigate the field angle measurements.

### 6.1. Polar Angle Measurement using MFAM Sensors

#### 6.1.1. Characterization of the probe DC transmission method

We first verify the response of the sensor probe DC level to the change of polar angle. The results are shown in Figure 33. A fit of Equation (2) to the experimental data is also shown as the red curve. As can be seen, the data agrees well with the theoretical model. Based on the fitting parameters, a look-up table of probe DC vs polar angle is generated. In the polar angle measurement, after the probe DC value is measured, the closest table element is found and the polar angle is interpolated linearly.

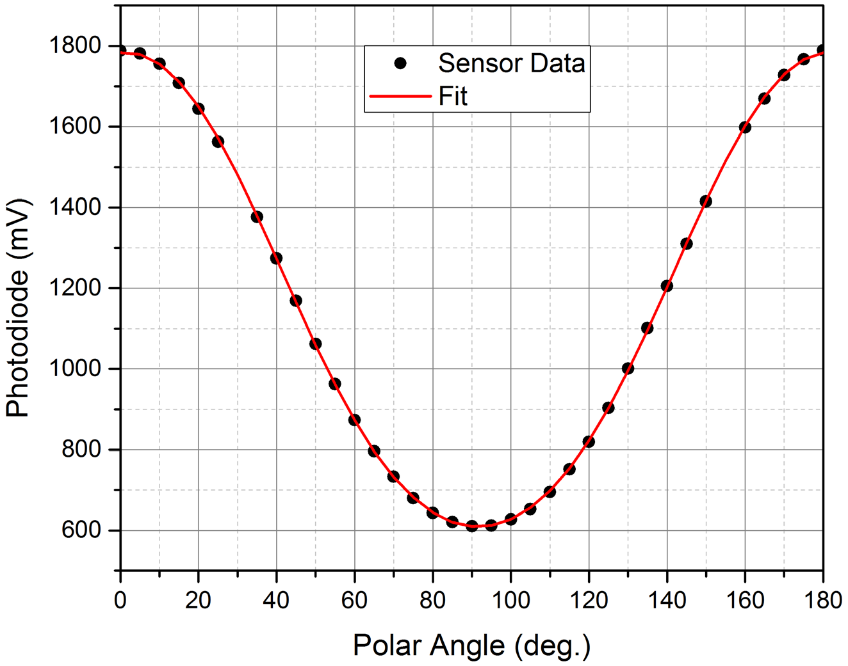

Figure 33 Probe DC output of a MFAM sensor as a function of polar angle (black dots). The red curve is a fit of Equation (2) to the data.

We also measure the Allan Deviation of the probe DC output with the polar angle set at about 45°. The result is shown in Figure 34. With an integration time of over 100 ms, the deviation of the probe DC drops below 0.3 mV. Combined with the slope of the curve in Figure 33 which is about 0.05 degree/mV around 45° polar angle, the most sensitive region of the angle measurement should have resolution better than 0.02°.

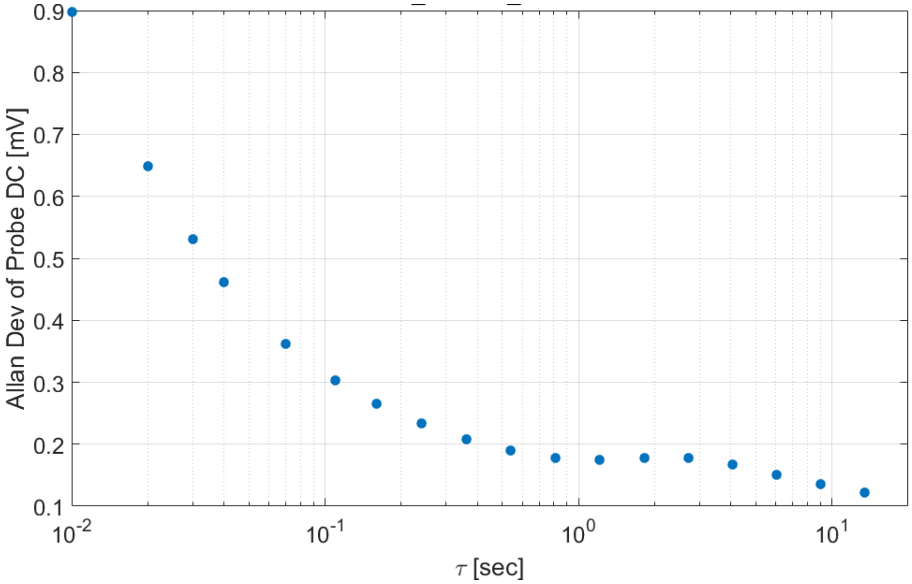

**Figure 34 The Allan deviation of the MFAM probe DC output.**

The bandwidth of the polar angle measurement based on the probe DC is also investigated. We set the polar angle to about 60°. A small oscillating field is added perpendicular to the probe. As a result, the total polar angle is changed by a couple of degrees at the same frequency as the oscillating field. We fix the oscillating field amplitude and change its frequency. The amplitude of the measured oscillating polar angle is recorded as a function of the driving frequency. The gain of the polar angle measurement at a certain frequency is calculated as the normalized amplitude relative to that at 1 Hz. The result is plotted in Figure 35. As seen in the plot, the system bandwidth is well above 50 Hz and is currently limited by the 100 Hz sample rate.

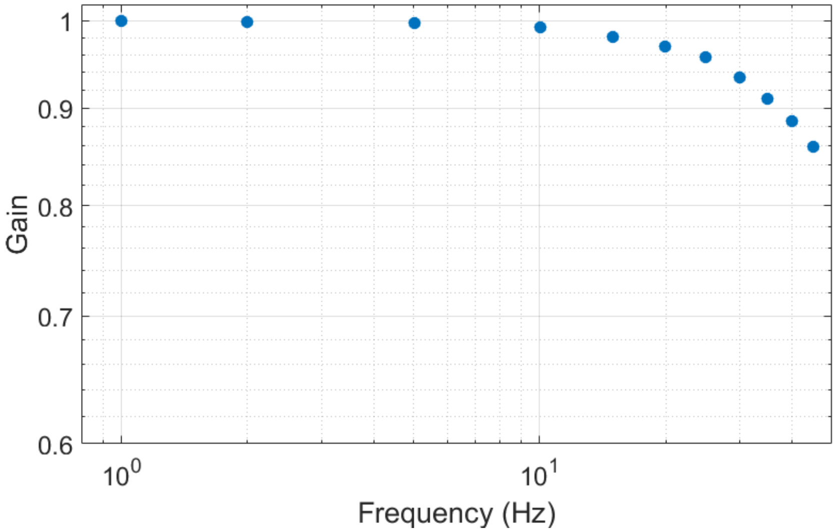

**Figure 35 Bandwidth of the MFAM probe DC based polar angle measurement.**

### 6.1.2. Characterization of the light-shift method

A small 3 kHz dither signal is applied to the laser current and modulates the wavelength of the laser light. This introduces a light shift that can be used for the polar angle measurement. The magnetometer reading is demodulated at 3 kHz with a bandwidth of 36 Hz. The Y component of the demodulator is then reported by the MFAM sensor.

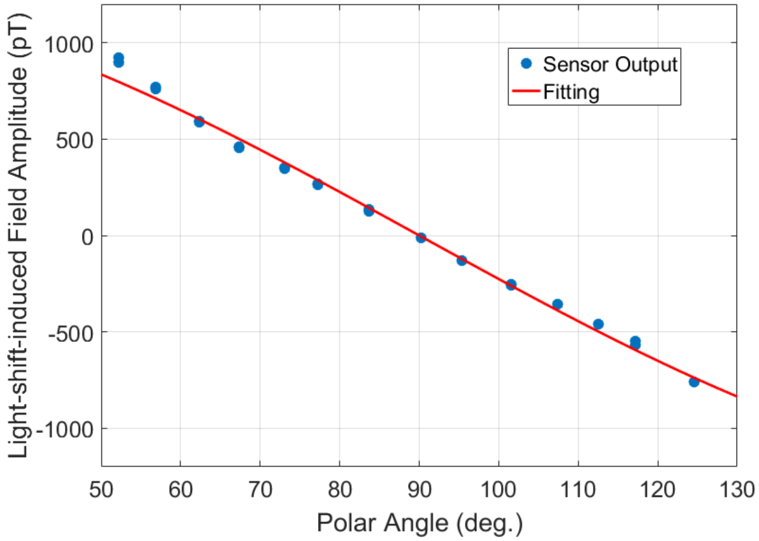

**Figure 36 Amplitude of the light-shift-induced oscillating field as a function of polar angle (blue dots). The red curve is a fit of a cosine function to the data.**

We first investigate the Y component amplitude as a function of the polar angle. The data is shown in Figure 36 as blue dots. A fit of a cosine function to the data is shown as the red curve. The data is well represented by a cosine curve around polar angles close to 90º, which is where the probe DC method is least sensitive. Away from 90º, only the sign of the Y component is used.

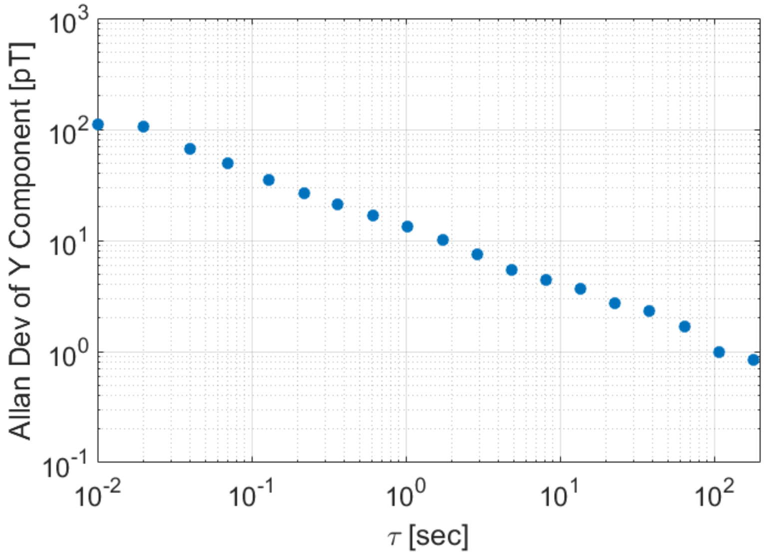

**Figure 37 Allan deviation of the amplitude of the light-shift-induced oscillating field.**

The Allan deviation is also measured and shown in Figure 37. With an integration time of about 100 ms, the noise in the demodulator Y component output is about 40 pT. The slope of the curve in Figure 36 is about 0.05 degree/pT around 90° polar angle, which yields a resolution of about 2° for the light-shift based polar angle measurement. This is much worse than the sensitivity achieved with the benchtop setup. It is mostly due to the linewidth of the VCSEL lasers, which is typically around 100 MHz, compared with sub-MHz linewidth for the DBR lasers used in the benchtop magnetometer. The laser linewidth contributes to the magnetometer noise through light absorption, which is a highly nonlinear procedure. In this case, the signal to noise ratio is reduced by about a factor of 10 due to the VCSEL linewidth.

### 6.1.3. Measurement of the polar angle

We combine the probe DC method and the light-shift method to generate the polar angle measurement. The measured probe DC is first compared with the minimum value in the lookup table. If it is within 5 mV from the minimum, the polar angle is calculated as the arccosine of $a/A$, where $a$ is the demodulator output and $A$ is the amplitude of the fitting cosine function shown in Figure 36. For other values of probe DC, the polar angle, $\theta$, is first calculated according to the lookup table. Then, based on the sign of $a$, the polar angle is decided between the value of $\theta$ or 180° - $\theta$.

We installed a testing setup at our NASA facility where the Earth magnetic field is minimally disturbed. The sensors are mounted to a rotation table, as shown in Figure 38. The optical axis of the sensor 1 is aligned with the rotation axis of the table and the sensor 2 optical axis lies parallel to the rotation plane. The rotation angle of the table is recorded by an optical encoder with a sensitivity of 0.35°. The rotation plane can also be adjusted between -30° and 70° with respect to the Earth magnetic field.

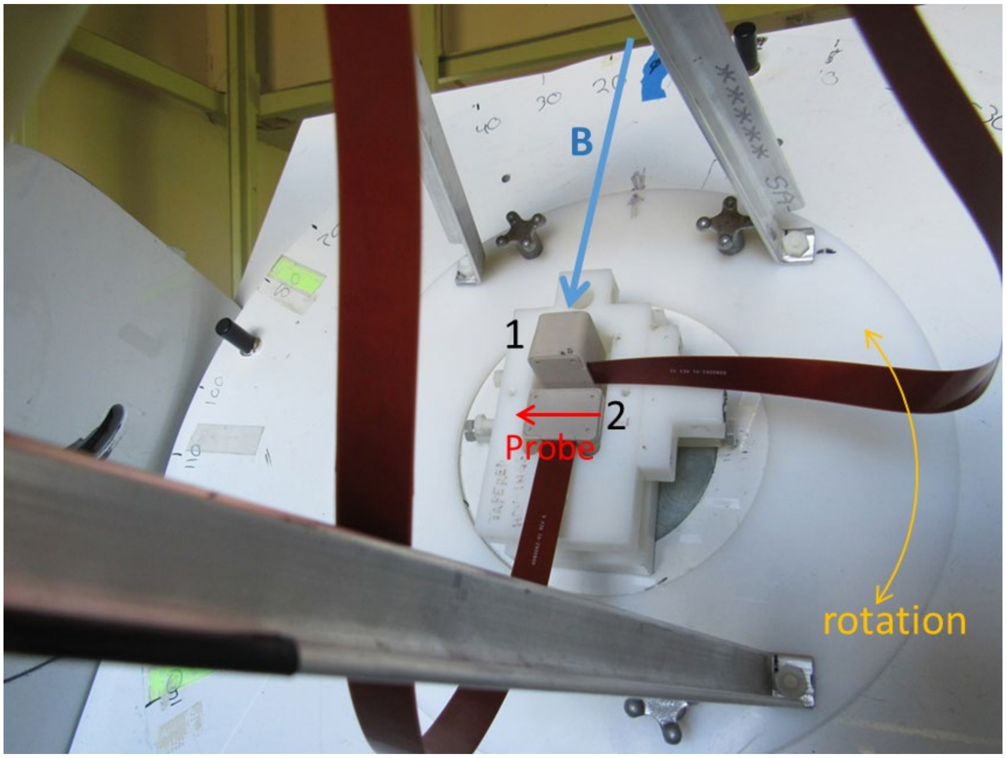

Figure 38 Testing setup for the polar angle measurement.

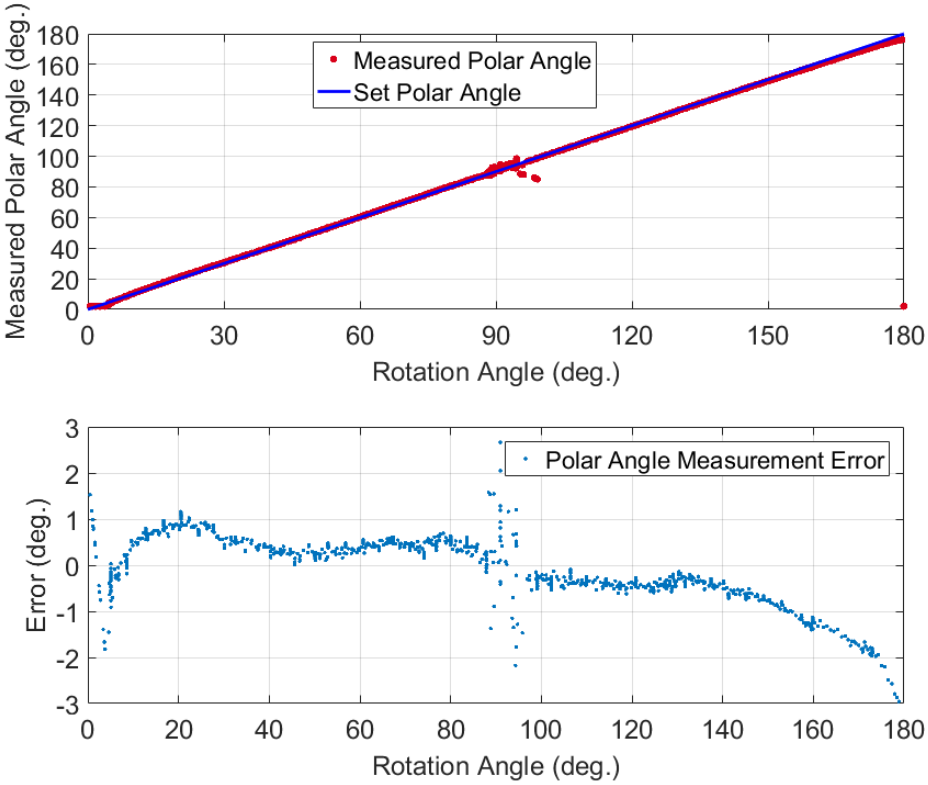

**Figure 39 Top: the measured polar angle vs the set polar angle. Bottom: the difference between the measured polar angle and the set polar angle vs the set polar angle.**

To test the polar angle measurement of the sensor 2, the table is set up such that its rotation axis is perpendicular to the Earth magnetic field. In this configuration, the rotation angle of the table (with a constant offset depending on the zero-angle position) is the set polar angle of the sensor 2. We record both the measured polar angle and the optical encoder output and plot the measured polar angles as a function of the set polar angle in Figure 39 (top). The difference between the measured polar angle and the set polar angle is also plotted in Figure 39 (bottom). As can be seen, for polar angles from 20° to 160°, the measurement produces fairly accurate results except in the vicinity of 90° where only the light-shift method is used.

### 6.2. Azimuthal Angle Measurement using MFAM Sensors

As discussed in Section 1.3., with two sensors, the azimuthal angle can also be measured. We set up two nearly orthogonal sensors as shown in Figure 38, with the sensor 1 optical axis defining the z-axis and the sensor 2 optical axis as the x-axis. In such a coordinate system, the polar angle of the sensor 1 defines the polar angle of the system and the azimuthal angle is calculated according to Equation (3). The system polar angle is set by adjusting the rotation plane angle with respect to the Earth magnetic field with an accuracy of about 1°. At a set polar angle, the table is rotated with the optical encoder output measuring the azimuthal angle. We define the total angle measurement error as the square root of sum of squares of polar and azimuthal errors. For a set polar angle between 60° and 160° in steps of 10° and a set azimuthal angle from 0° to 180° in steps of 5°, the total angle measurement error is plotted on a color scale from 0° to 6° in Figure 40. The scale saturates at 6°. As can be seen, the angle measurement method can produce results better than 3°

accuracy for most orientations. The error goes up significantly when one sensor approaches its dead zone, where its optical axis is aligned with the magnetic field. This is not surprising since at the center of the sensor dead zone, both the probe DC method and the light-shift method fail to produce the polar angle. Typically within +/- 25° of z-axis or x-axis (sensor optical axis), the azimuthal angle measurement result can be considered invalid.

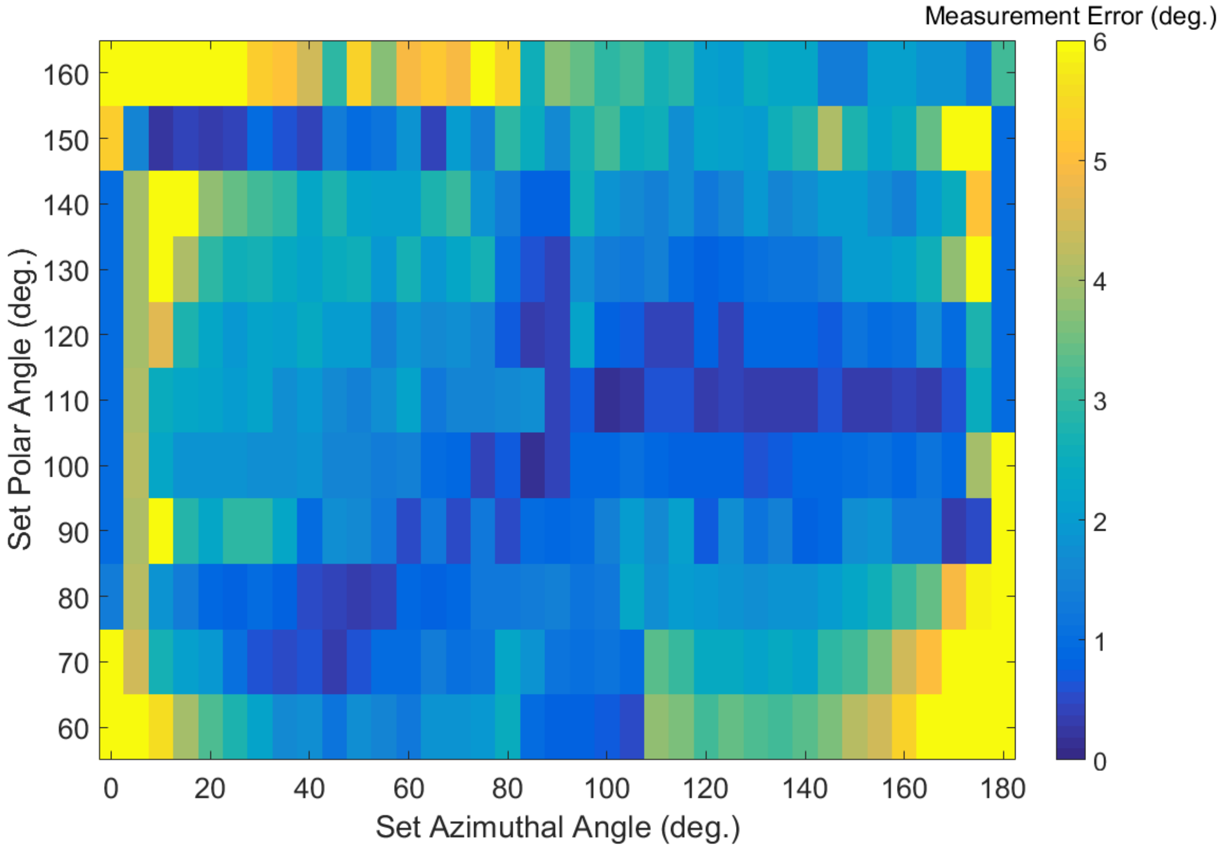

Figure 40 Total angle measurement error at different set angles.

### 6.3. Discussion and Conclusion

The biggest challenge facing the angle measurement is the stability of the operating temperature of the atomic vapor cell. A diode next to the cell is used to stabilize the cell temperature. However, the operating temperature of the cell is set by its coldest point, which is not necessarily detected by the diode. Change of the environmental temperature can affect the cell operating temperature slightly, leading to shape changes in the probe DC signal vs the polar angle curve, as shown in Figure 33. In fact, if we use two different lookup tables, one for a higher cell temperature, a much better measurement accuracy can be achieved.

The sensitivity in the light-shift method cannot be improved much due to the limit of the VCSEL laser. With future improvements in VCSEL fabrication technology, the light-shift method can also be improved. In the azimuthal angle measurement, at present, there is still an ambiguity between azimuthal angle, φ and 360°- φ. If the pump and the probe lights have an angular separation, the phase delay of the Larmor signal with respect to the pumping signal becomes dependent on the rotation of the optical plane defined by the pump and the probe beams. In principle, this phase delay can be used to remove the ambiguity in the azimuthal angle measurement. The implementation of this method is beyond the scope of the current research.

In conclusion, we have demonstrated the measurement of orientation of the magnetic field using a scalar atomic magnetometer with advanced signal extraction techniques. Away from the dead zones and 90° polar angle, a single sensor can produce a polar angle measurement better than 1° in accuracy and 0.1° in noise with 100 ms integration time. With two orthogonal sensors, the azimuthal angle of the field can also be measured with an accuracy of better than 10°. We demonstrate that the angle measurement method is suitable for next objectives. Specifically, to achieve the fast-recovery of the magnetometer operation only after the EM pulse, we do not need the angle measurement. Under the real-world field conditions, we do expect the angle measurement to be less robust mainly due to the temperature fluctuation in the environment. This issue can be addressed by using additional thermally insulating materials covering the sensor.

Any field measurement during the EM pulse requires a significant local compensation of the EM pulse at the location of the magnetometer. Otherwise the heading error effect will most likely dominate the measurement for any practical applications. The compensated local EM pulse is likely to be less than one micro Tesla. Even with an angle measurement error of 10°, the resulting error in the estimated resonant Larmor frequency during the EM pulse should still be less than 1 kHz, which is less than the FWHM of the typical magnetic resonance in our scalar magnetometers. This should enable the fast recovery of the magnetometer operation during the EM pulse.

Finally we want to emphasize that the 100 Hz sample rate quoted in this report is only for the angle measurement. The magnetic field output sample rate of our advanced magnetometer system is 1 kHz by default and can be increased to 3 kHz if necessary. In practical applications, the angle measurement is used to minimize negative effects to the magnetometer operation due to the relative orientation change of the instrument with respect to the Earth magnetic field. A sample rate of 100 Hz should be fast enough for this purpose.

## 7. Fast Recovery of MFAM Operation in Presence of EM Pulses

### 7.1. MFAM Slew Rate

We first test the slew rate of the MFAM sensor. The sensor is placed inside a magnetic shield can with a constant background magnetic field set perpendicular to the optical path of the sensor. Additional 1 μT magnetic field pulses are generated along the same direction. The pulse has a repetition rate of 20 Hz and a duty cycle of 20%. The MFAM readings are recorded with different ramping time constants of the magnetic field pulse. For ramping time constants larger than 80 μs, MFAM can track the magnetic field pulse robustly, which is shown in Figure 41 for 80 μs ramping time. In the zoom-in plot, we can see small spikes in the reading when the pulse is switched on and off. This is mainly due to the response of the output digital filter to a step change in the magnetic field reading. PLL dynamics also contributes to the spikes. When the pulse ramping time is less than 80 μs, MFAM sometimes loses track of the pulse, as shown in Figure 42 for a ramping time of 70 μs. In the zoom-in plot, it is clear that magnetometer outputs invalid readings even after the pulse is switched off.

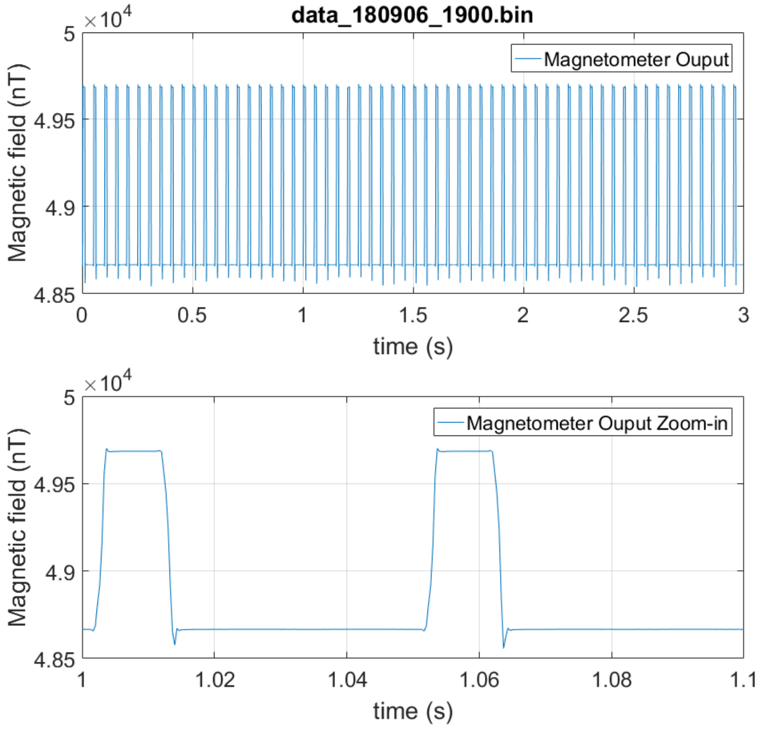

**Figure 41 MFAM reading under a magnetic pulse. The pulse has a magnitude of 1 µT, a repetition rate of 20Hz, a duty cycle of 20% and a ramping time constant of 80 µs.**

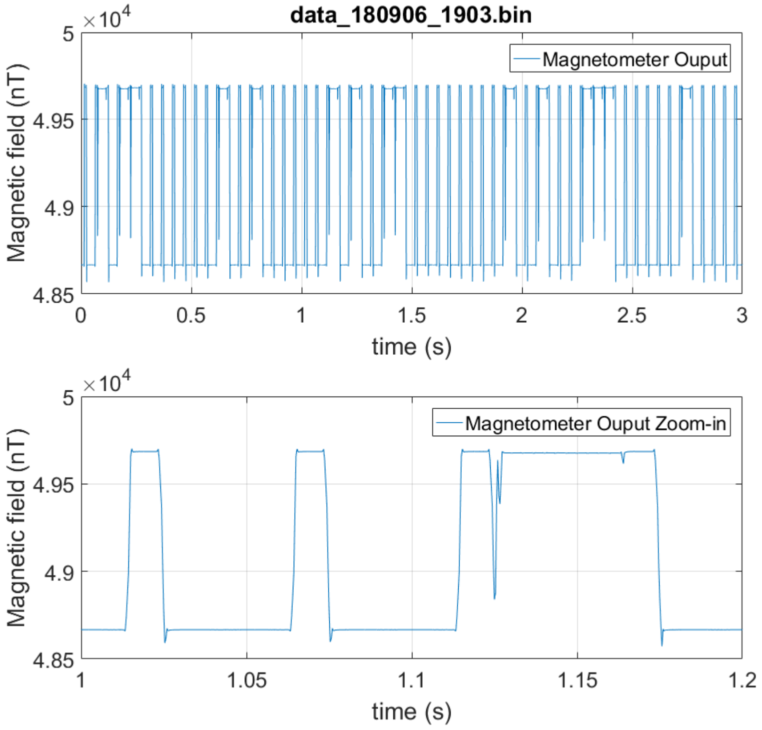

**Figure 42 MFAM reading under a magnetic pulse. The pulse has a magnitude of 1 µT, a repetition rate of 20Hz, a duty cycle of 20% and a ramping time constant of 70 µs.**

The above experiments indicate a MFAM slew rate of 10 μT/ms, which is much smaller than the slew rate demonstrated in Figure 21. This is expected as discussed in the Technical Approach section. Due to higher noises resulting from both lasers and driving electronics, we have to limit the bandwidth of the PLL implemented in the MFAM in order to achieve a robust and stable operation. The MFAM slew rate, however, is still an order of magnitude higher than that of many commercial magnetometers.

### 7.2. Fast Recovery after EM Pulses

As discussed in Section 3.2., less than one millisecond recovery time is possible. Therefore, the MFAM data sample rate is increased to 3 kHz for this project from the standard 1 kHz.

#### 7.2.1. Fast recovery scheme

Main steps for fast-recovery after the EM pulse is schematically shown in Figure 43. When MFAM starts, it searches the full operation range for the Larmor frequency. After the Larmor frequency is found, the PLL is enabled and the magnetometer is in the *Normal Operation* mode, where the magnetometer outputs one-millisecond-delayed local oscillator frequency as the field reading and keeps measuring the probe Larmor amplitude. A memory is also created to store the latest Larmor frequency. The stored Larmor frequency is continuously updated until the probe Larmor amplitude reaches *threshold1*, indicating the onset of the EM pulse. At this moment, the PLL is immediately switched off. The 1 ms delay is necessary to ensure that the stored Larmor frequency is not affected by the EM pulse. Now the magnetometer enters *Fast Recovery* mode. First, the stored Larmor frequency is loaded as the local oscillator frequency (pump modulation frequency). The probe Larmor amplitude is then continuously measured. If it reaches *threshold2*, indicating the end of the EM pulse, the PLL is temporarily on for 51 μs. During this stage if the probe Larmor amplitude stays above threshold1, *Normal Operation* is resumed. Otherwise, the detected signal is due to noise and the magnetometer restarts the fast-recovery procedure. *Threshold2* is set to be slightly larger than *threshold1* for robust fast-recovery operation. A timeout of one second (starting from PLL off) is also set in case of unpredicted failures. We refer the magnetometer reading in *Normal Operation* as valid. In other stages, the magnetometer can also output the local oscillator frequency, which is flagged as invalid and can be replaced with 0.

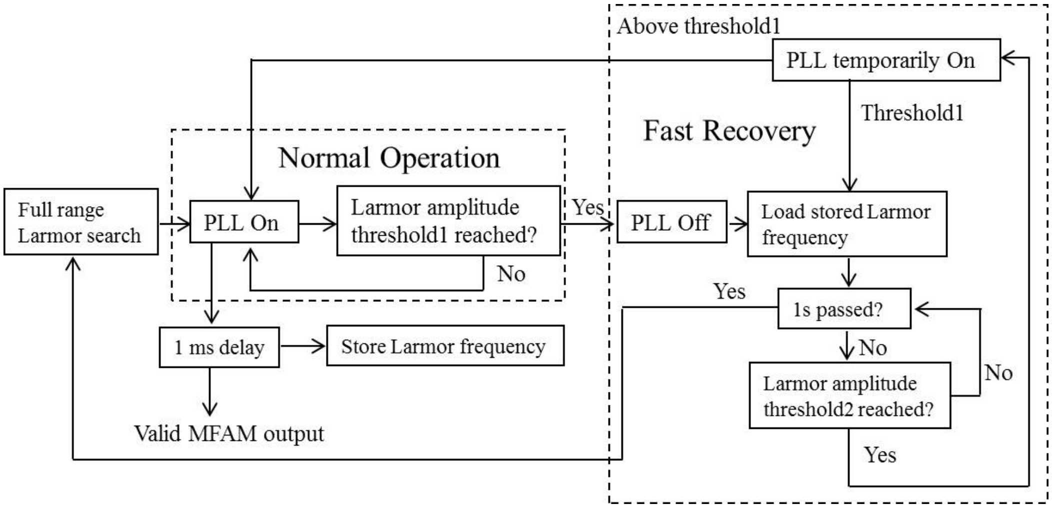

Figure 43 Schematics showing the fast-recovery method after EM pulses.

### 7.2.2. Fast recovery with background field in optimal direction

After implementing the fast-recovery scheme, we first test the sensor in the magnetic shield can with the constant background field (~48.337 μT) set perpendicular to the optical path of the sensor. Additional 5 μT magnetic field pulses are generated by an arbitrary function generator through a 5-turn 1-cm-in-diameter coil. The pulse is in the same direction as the background field, with a ramping time of less than 10 μs, a repetition rate of 10 Hz and a duty cycle of 30%. The pulse is well above the slew rate of the magnetometer. With the fast-recovery method implemented, the valid MFAM readings are shown in Figure 44, with invalid readings replaced with 0. As can be seen, after the pulse generator is enabled around t = 3.1 s, magnetometer recovery during pulse-off is very consistent. In the zoom-in plot, it is also shown that the noise performance of the magnetometer is not affected by the fast-recovery method. The peak-peak noises in the magnetometer readings are the same before and after the pulse.

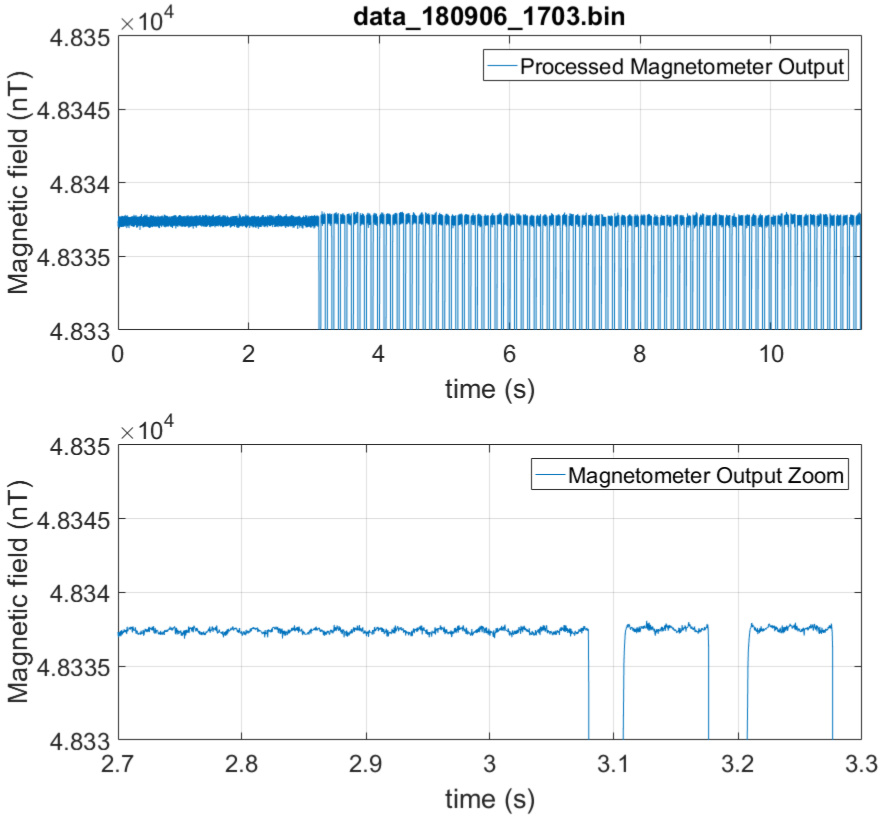

Figure 44 Fast recovery of MFAM operation after EM pulses.

To characterize the fast-recovery time, we program the arbitrary function generator to produce a tiny signal during pulse-off. The signal has FWHM of 0.5 ms and peak amplitude of about 10 nT. The time separation between the signal peak and the falling edge of the pulse is one millisecond. We use an oscilloscope to measure the voltage across a pick-up resistor to record the signal, shown in Figure 45. The oscilloscope is triggered by the falling-edge of the pulse at t = 0. The peak of the signal is at t = 1 ms. If this signal can be detected by the magnetometer, fast-recovery time of 1ms or less is demonstrated.

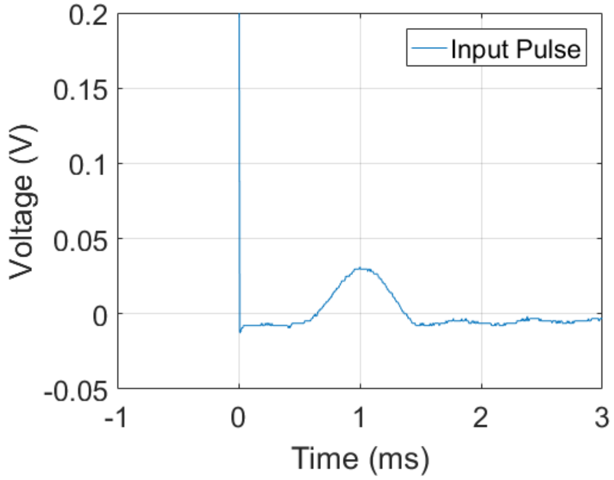

Figure 45 Oscilloscope recording of a tiny signal during pulse-off, starting at t = 0.

The valid magnetometer reading is shown in Figure 46. Compared with the result shown in Figure 44, a spike signal is consistently detected by the magnetometer. We notice that the measured signal amplitude is not constant. Long-term variation in the measured signal amplitude is due to the 3 kHz sample rate of the magnetometer output. Only several readings are reported during the signal duration. Since the magnetometer output and the pulse generation are not synchronized, the magnetometer reading during the peak of the signal may not be consistently reported. The measured amplitude variation between neighboring signals is due to a small inconsistence in the fast-recovery time.

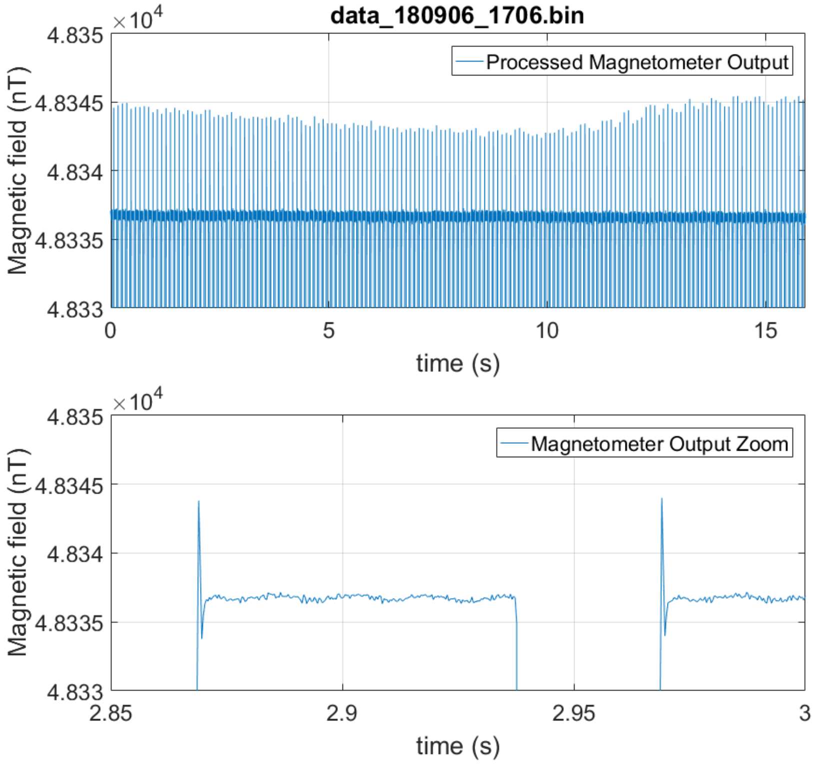

Figure 46 Fast recovery after magnetic pulses with a tiny signal, as shown in Figure 45, during pulse-off.

As shown in the zoom-in plot in Figure 46, the background field during the signal appears to be several nT lower than the overall background reading. A more careful study indicates that an extra 2 ms is required for the magnetometer reading to settle, as shown in Figure 47. After some investigations, we are confident that the settling of the magnetometer reading after the pulse is due to the dynamics of the PLL, although we cannot completely rule out the possibility that this phenomenon is due to the real magnetic field change, caused by the fast switching of the magnetic pulses.

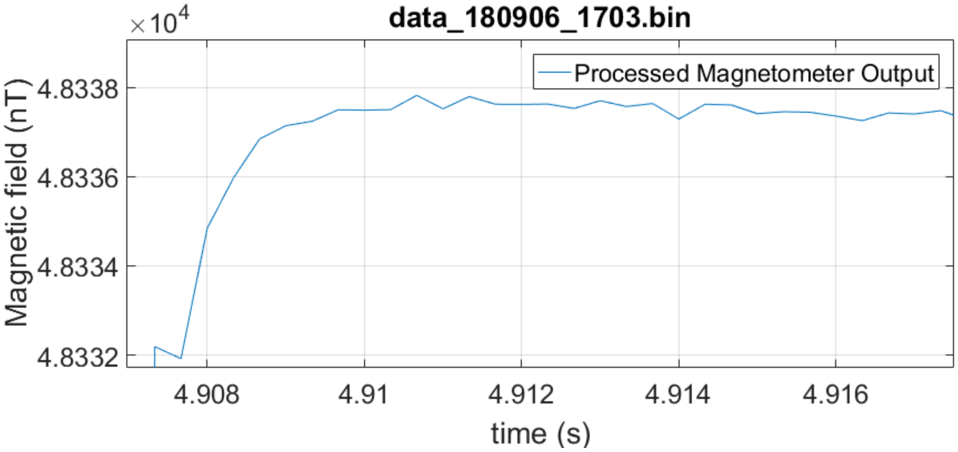

Figure 47 Magnetic field readings right after the pulse.

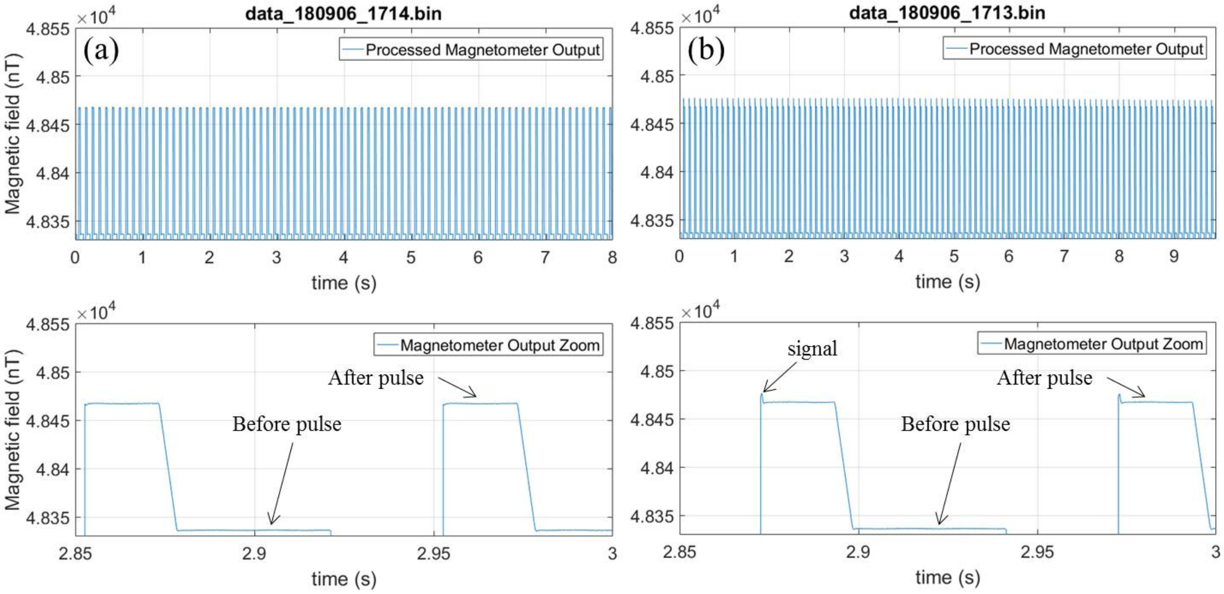

Figure 48 Change of ~150 nT in the background magnetic field before and after the magnetic pulse (a). (b) A tiny signal is added during the pulse-off, with 1 ms between the signal peak and the off-edge of the pulse.

So far we demonstrate the magnetometer fast-recovery in a constant background magnetic field. In practice, the background field may be slightly different before and after pulses. However, we do not expect a big change since the EM pulses are typically very short (less than 10 ms). In Figure 48 (a), we show the fast-recovery result when there is a 150 nT difference between the background magnetic fields before and after the magnetic pulse. As can be seen, the fast-recovery still works robustly. We also introduce the same signal, as shown in Figure 45, during the pulse-off. The measurement result is presented in Figure 48 (b). As seen in the plot, the signal is still detected, indicating a minimal impact of the background magnetic field change on the fast-recovery time. Field changes in the opposite direction are also tested and similar results are observed.

### 7.2.3. Fast recovery with background field in polar 30º direction

The Larmor amplitude depends on the polar angle of the magnetic field, which is defined as the angle between the magnetic field direction and the optical path of the magnetometer. In the previous section, the background magnetic field is set along the optimal direction, 90º polar angle. In practice, this condition is usually not satisfied. As a result, the Larmor amplitude is reduced, which may cause problems for the fast-recovery method since it relies on the Larmor amplitude. In this section, we set the background magnetic field along the polar 30º direction, which is right outside the dead-zone of the magnetometer. We carry out similar tests as discussed in the previous section. Overall, similar performances are observed. However, under similar conditions as in Figure 48 (b), the tiny signal sometimes is not detected, indicating a magnetometer recovery time of more than 1 ms. After we increase the separation between the peak of the signal and the falling edge of the pulse to 2 ms, consistent detection of the signal is observed. The experimental data is shown in Figure 49.

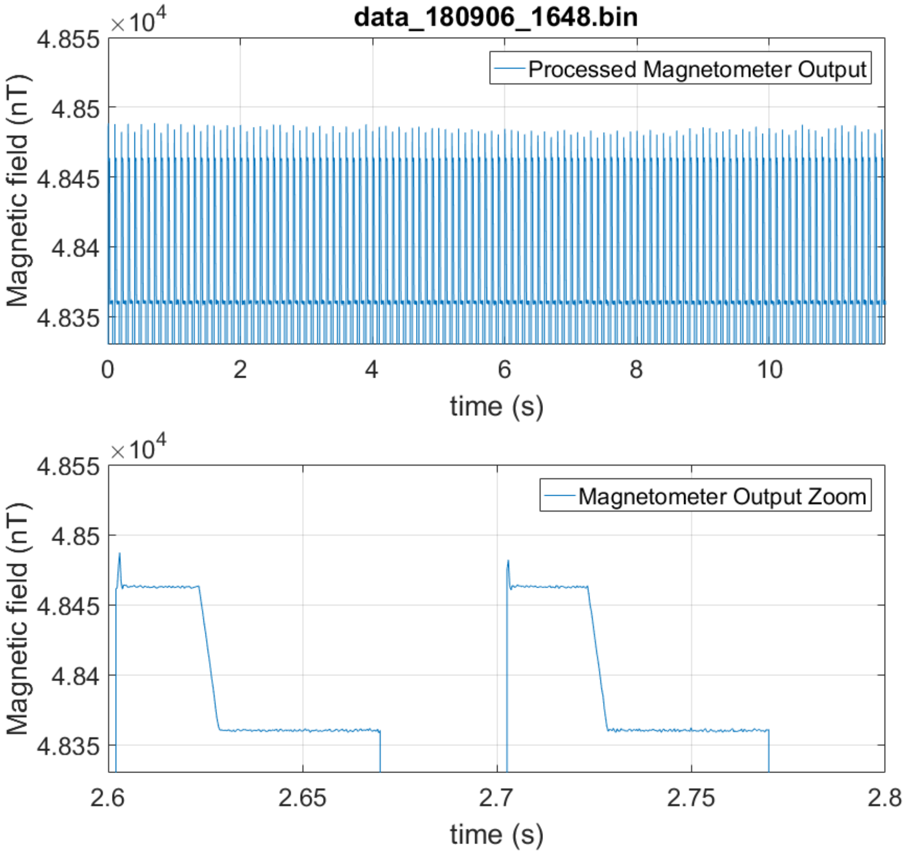

**Figure 49 Change of ~100 nT in the background magnetic field (along polar 30º direction) before and after the magnetic pulse (along polar 90º direction). The separation between the off-edge of the pulse and the signal peak is 2 ms.**

### 7.2.4. Simultaneous operation of MFAM sensor with TDEM system

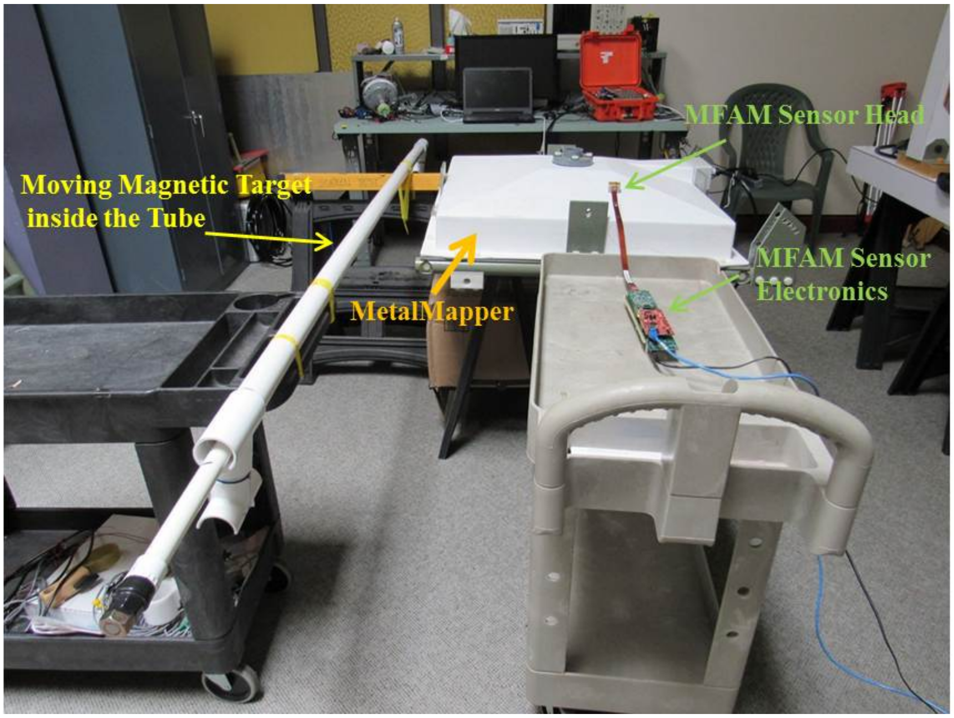

Figure 50 Setup for testing the simultaneous operation of the magnetometer and the MetalMapper.

We now test the simultaneous operation of MFAM with a commercially available TDEM system, MetalMapper from Geometrics. The setup is shown in Figure 50. To simplify the testing setup, we move the magnetic target, instead of the MFAM-MetalMapper system. For the maximum effect of the EM pulse on the magnetometer operation, the MFAM sensor head is placed directly on top of the MetalMapper. In this sensor orientation, the polar angle of the Earth's field is about 60º. We record the MFAM readings during on and off of the MetalMapper. In the meanwhile the magnetic target travels back and forth in the tube, changing the total magnetic field by about 25 nT at the location of the sensor. When the MetalMapper is on, it generates 8 ms pulses in alternating directions separated by 8 ms off times. The pulse has amplitude much larger than the Earth's field at the location of the sensor. The raw MFAM output, including valid and invalid readings discussed in section 7.2.1., is plotted in Figure 51 (a). As can be seen, when the MetalMapper is turned on, MFAM reading becomes very noisy, overwhelming any magnetic field signals. After the MetalMapper is switched off, the effect of the moving magnetic target clearly shows up. The reading noise during MetalMapper off is dominated by 60 Hz oscillating magnetic fields generated by nearby power lines.

If the MFAM recovery time is much less than 8 ms and an internal signal can be used to distinguish between valid and invalid readings, noises caused by the MetalMapper can be filtered out and the real magnetic response can be recovered. In Figure 51 (b), we plot only the valid readings of the same data in Figure 51 (a). Filtered data indicates that turning on the MetalMapper almost has no effect on the MFAM operation. Note that here we flag additional 2 ms data as invalid, as discussed in the paragraph describing Figure 47. Otherwise, the signal during the MetalMapper-on is a little bit noisier.

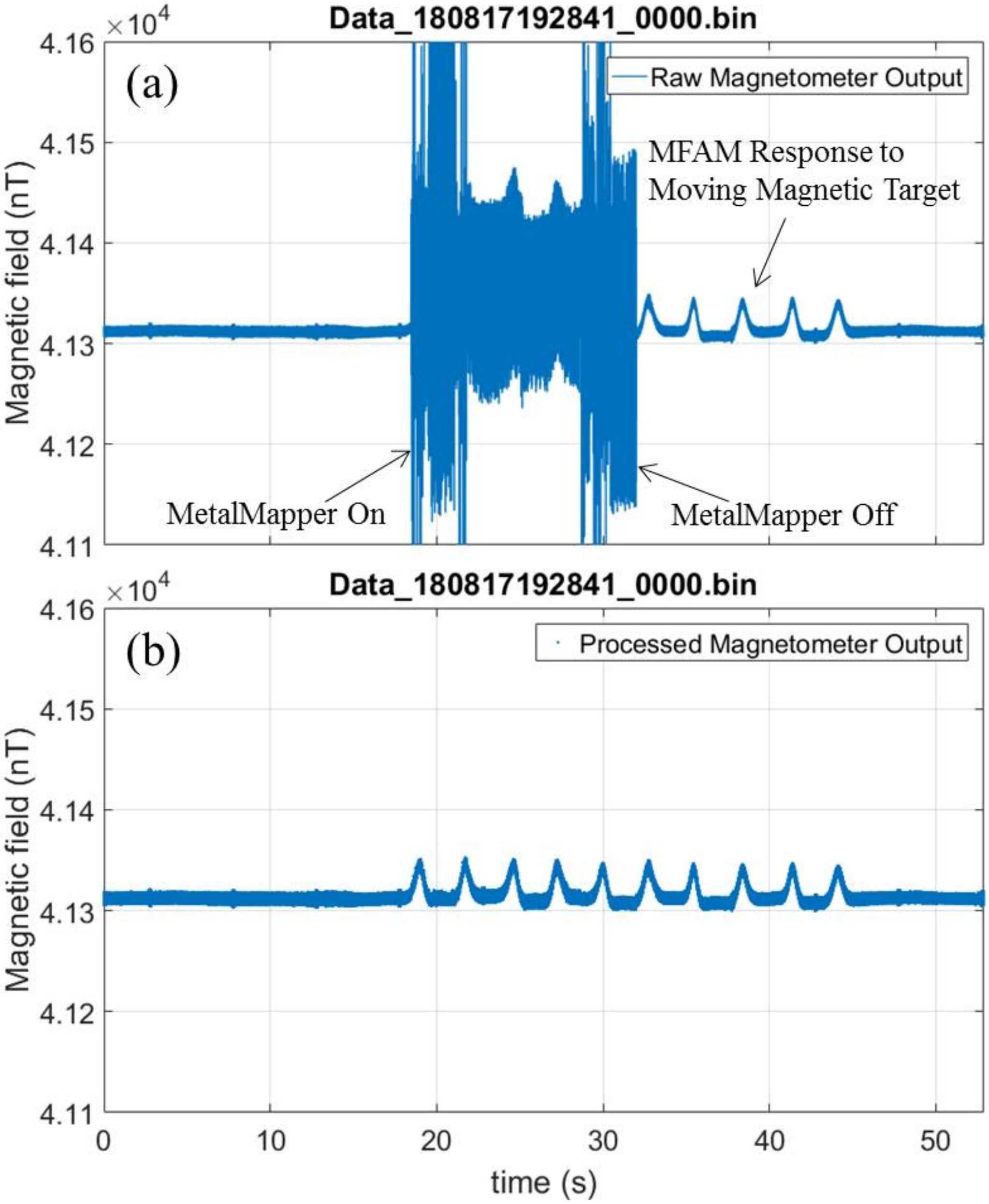

**Figure 51 MFAM readings during on and off of the MetalMapper. (a) Raw MFAM output including valid and invalid readings. (b) The same data as in (a), but only valid readings are plotted as dots.**

### 7.2.5. Discussion

In this section, we demonstrate the fast-recovery of MFAM operation after the EM pulse. MFAM can respond to magnetic field changes less than 1 ms after the EM pulse is switched off. When measuring magnetic signatures less than 10 nT, additional 2 ms recovery time may be needed. We also set up a MFAM-MetalMapper system and successfully demonstrate the simultaneous operation of the MFAM with the commercial TDEM system. With the fast-recovery method, the negative effect of the EM pulse on the MFAM operation is shown to be minimized. We expect the fast-recovery to function well as long as the frequency of the TDEM system is less than 100 Hz, i.e. the off-time of the EM pulse is more than 2.5 ms assuming bi-polar EM pulses.

## 7.3. Fast Recovery during EM Pulses

### 7.3.1. Fast recovery scheme

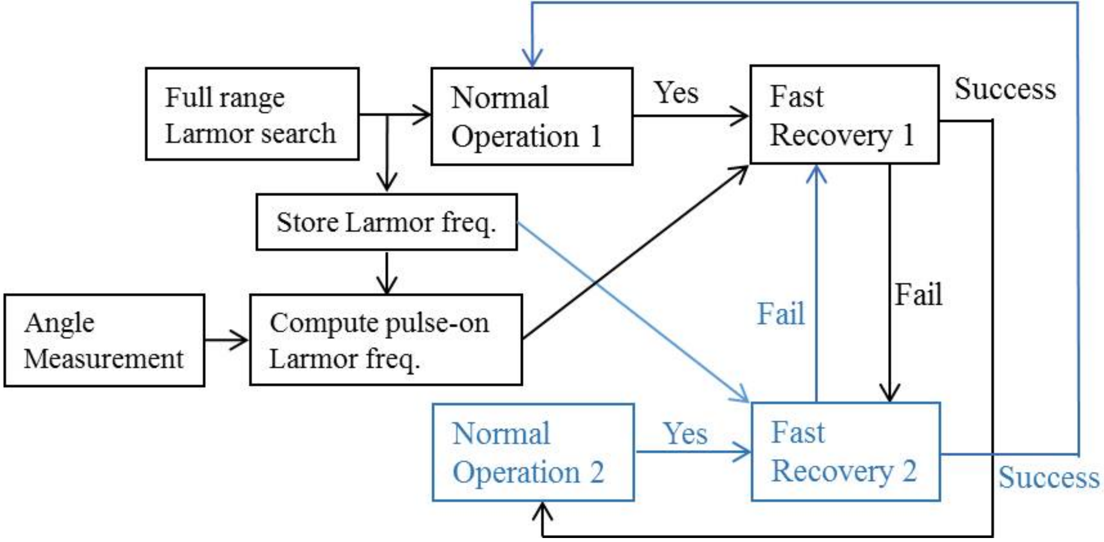

Figure 52 Schematics showing the fast-recovery method during EM pulses.

The procedure for fast-recovery during the pulse is schematically shown in Figure 52. Here *Normal Operation* and *Fast Recovery* procedures are essentially the same as shown in Figure 43. When MFAM starts, it searches the full operation range for the Larmor frequency. After the Larmor frequency is found, it is stored and *Normal Operation 1* starts. If the Larmor signal is lost during *Normal Operation 1*, magnetometer operation enters *Fast Recovery 1*, where the starting frequency for the local oscillator is the calculated Larmor frequency based on the angle measurement, which is updated every 10 ms. If *Fast Recovery 1* succeeds within 0.8 ms, *Normal Operation 2* follows. *Normal Operation 2* is essentially the same as *Normal Operation 1*, except that when it fails, magnetometer enters *Fast Recovery 2*. In *Fast Recovery 2* the starting frequency for the local oscillator is the stored Larmor frequency. If *Fast Recovery 1* fails after 0.8 ms, *Fast Recovery 2* is tried, and vice versa. This step is in general not necessary. However, in this scheme, no internal signal of the magnetometer can be used to identify the pulse-on and pulse-off (pulse-on can be treated as pulse-off while the pulse-off is the opposite-pulse-on). In case that the starting Larmor frequency is wrong, the alternative starting frequency is also tried. If the magnetometer does not resume normal operation (either 1 or 2) after one second, it starts searching for the Larmor frequency again over the full frequency range. MFAM cannot detect the polarity of the EM pulse. Therefore the calculated Larmor frequency may be incorrect. To solve this problem, if two consecutive normal operations are in *Normal Operation 1*(meaning that the fast-recovery-during-pulse does not work), the opposite pulse polarity is assumed for the Larmor frequency calculation. This procedure is not shown in Figure 52.

In many practical applications, the EM pulse keeps switching its polarity. The above recovery scheme will not work in these cases. In principle this issue can be solved by sending out two trigger signals from the EM system, synchronized with the positive and negative pulses, to the magnetometer for selecting three starting Larmor frequencies for the fast recovery. This solution is beyond the scope of this project since fundamental hardware changes will be required for MFAM electronics. However, the research here is still valuable because the fundamental fast-recovery scheme remains the same.

### 7.3.2. Fast recovery during EM pulses in magnetic shielded environment

We first test the fast-recovery scheme inside the magnetic shield can. The EM pulse is fixed along the optical path of the magnetometer and calibrated to be about 5 μT with less than 10 μs ramping time. The pulse is on for 5 ms and repeats at 50 Hz. Its polarity can also be switched. In this pulse configuration, only the polar angle of the background magnetic field is needed for calculating the Larmor frequency during the pulse. The fast-recovery method is tested for many background magnetic field directions. Robust fast-recoveries during and after the pulse are observed. The experimental data for the background magnetic field along polar 30° is shown in Figure 53. Over many cycles, the fast-recovery method does not fail except right after the pulse polarity is switched, as shown in the zoom-in plot. When the pulse polarity is switched, the calculated Larmor frequency during the pulse is no longer correct. Fast-recovery will not work during the pulse-on. As discussed in the above section, after two consecutive fast recoveries in *Normal Operation 1*, the opposite polarity is assumed. Fast-recovery works again when the next pulse is on. Since both pulse polarities are taken into account in the fast-recovery algorithm, only polar 0° to 90° is needed in the angle measurement. Polar 90° to 180° with one pulse polarity gives the same answer as polar 0° to 90° with the opposite pulse polarity. In Figure 53, both valid and invalid readings are plotted.

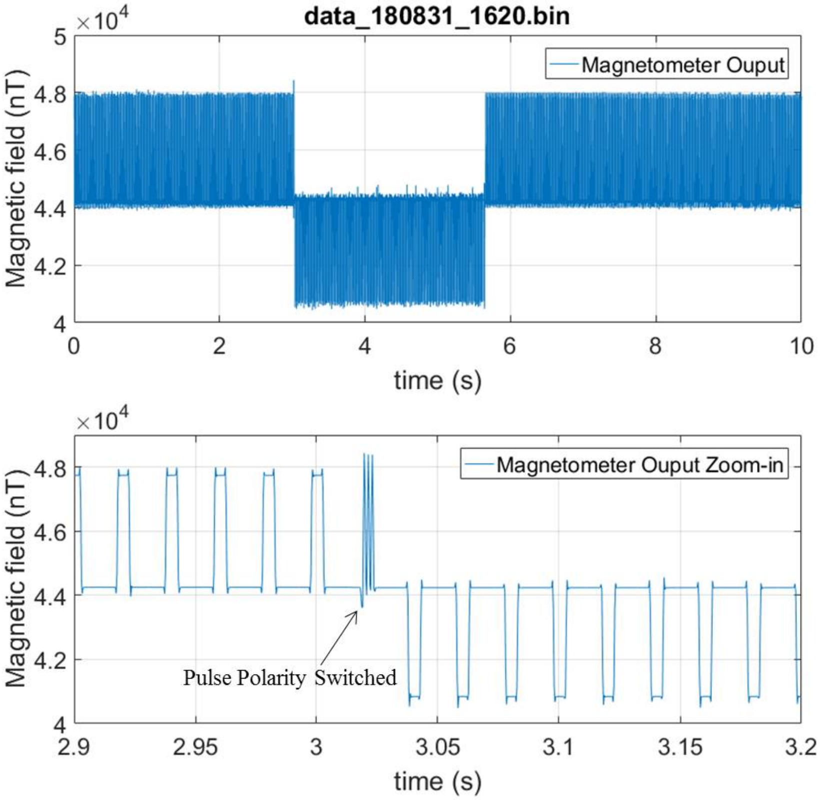

**Figure 53 Fast-recovery during EM pulses. The pulse is along the optical path (polar 0°) of the MFAM sensor and the background magnetic field is along polar 30°. Both valid and invalid readings are plotted.**

To measure the fast-recovery time, we zoom into a single-pulse duration within the data shown in Figure 53 and plot only the valid readings in Figure 54. As shown, both recovery times during and after the pulse are a little less than 2 ms. This recovery time is longer than that for the fast-recovery-after-pulse method, mainly due to the increased complexity of the recovery scheme. We expect the recovery time to be reduced if trigger signals of the EM pulse can be used to simplify the fast-recovery scheme.

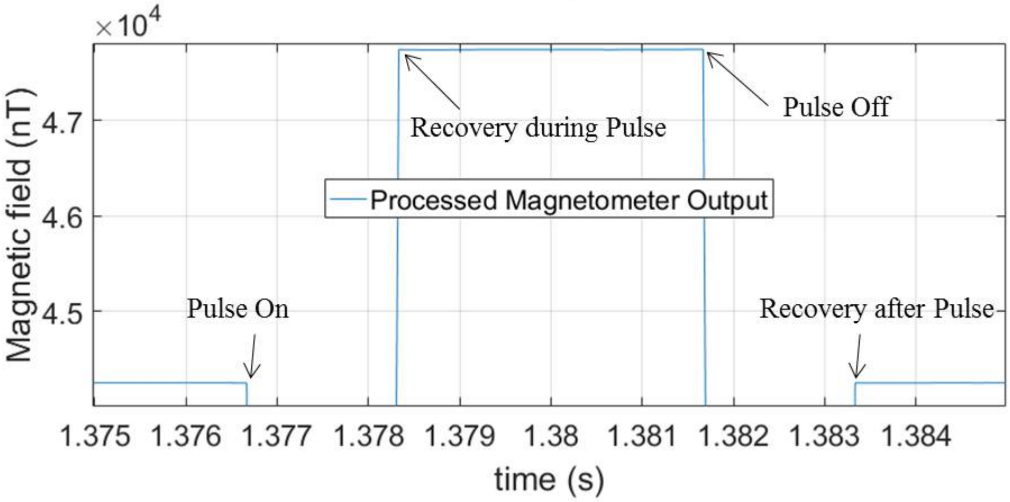

Figure 54 Zoom-in plot of the data shown in Figure 53. Only valid readings are shown here.

### 7.3.3. Fast recovery during EM pulses in open environment

We also test the fast-recovery-during-pulse method outside the magnetic shield can. The setup is shown in Figure 55. The EM pulse is generated by an arbitrary function generator through two 5-turn coils wrapped around the MFAM sensor head. The magnetic pulse is along the optical path (polar 0º) of the MFAM sensor and has amplitude of 5 μT, repetition rate of 10 Hz and a duty cycle of 50%. When the pulse is on, the sensor head is also rotated randomly in order to simulate the instrument orientation change during surveys.

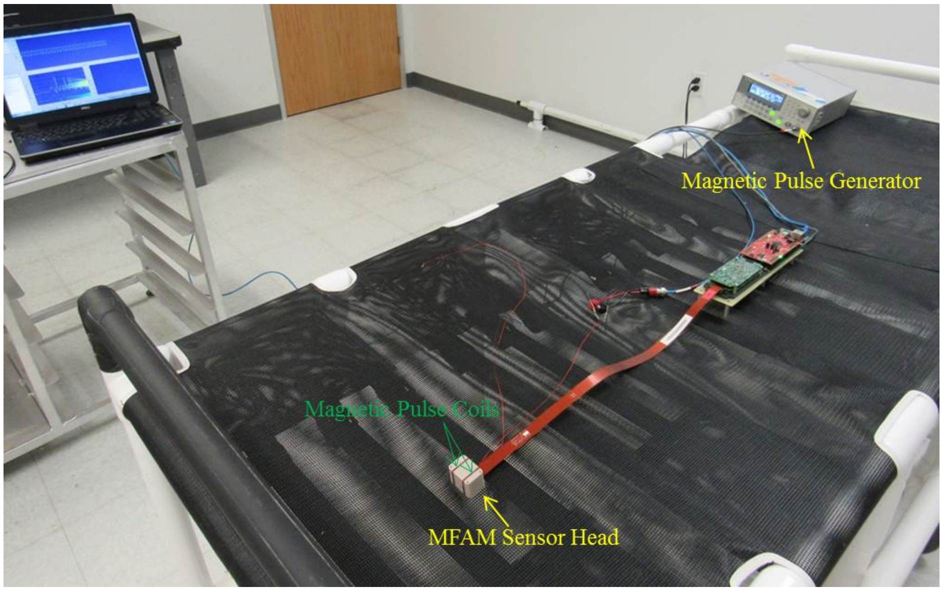

Figure 55 Experimental setup for testing the fast-recovery-during-pulse method in the open environment.

Magnetometer readings are recorded by a computer and raw data is plotted in Figure 56. As seen in the plot, during the pulse on, the MFAM reading is changing due to the rotation of the sensor (together with the pulse direction) in the Earth's magnetic field. As a result, the total magnetic field at the location of the sensor is changed. When the Earth's field is close to polar 90°, the projected pulse field is almost negligible. When the sensor is right outside the dead-zone, the projected pulse field has the largest amplitude. Angle measurement ensures that the calculated Larmor frequency during pulse-on is accurate enough throughout the rotation of the sensor. We also rotate the sensor through the dead-zone. In one case, the sensor stays in the dead-zone for more than two seconds, forcing MFAM to restart the full range Larmor search. In another case, the sensor goes through the dead-zone quickly. In both cases, MFAM recovers its operation once outside the dead-zone.

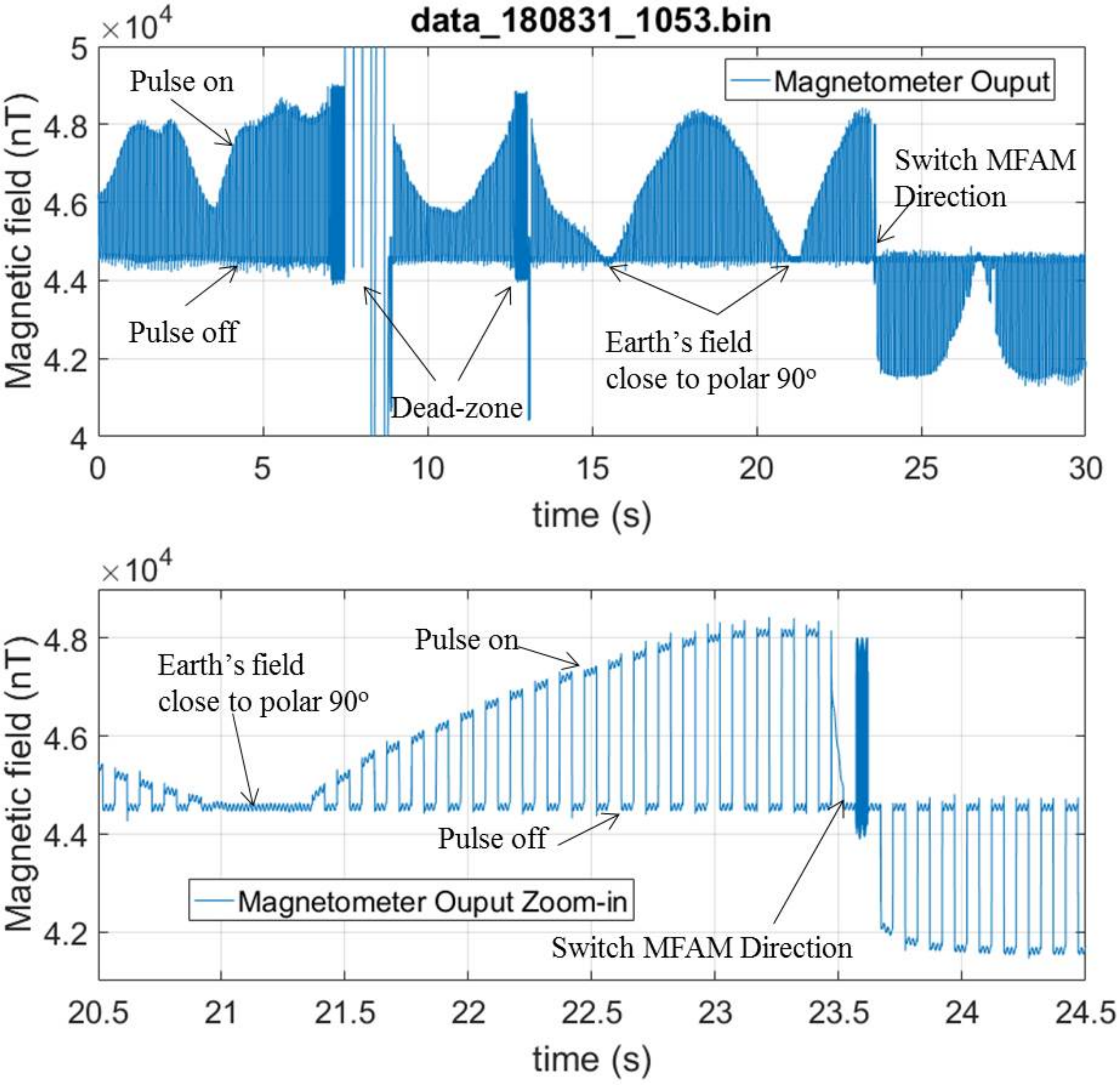

Figure 56 Fast-recovery during EM pulses in the open environment. The data is taken when the MFAM sensor is rotated.

Opposite pulse direction is also tested by quickly switching the sensor to the opposite orientation. As seen in the zoom-in plot, after one pulse cycle, the magnetometer recovers its operation during pulses. Small oscillating signal is present during both pulse-on and pulse-off. This oscillating signal is the magnetic field generated by nearby 60 Hz power lines. Detection of small 60 Hz oscillating magnetic field confirms that the magnetometer is functioning both during and after pulses.

#### 7.3.4. Discussion

In section 7.3., we demonstrate the fast-recovery of MFAM operation during EM pulses. Angle measurement result is used to calculate the starting Larmor frequency for fast-recovery during the pulse-on. Less than 2 ms recovery time is achieved. We also simulate the real survey operation by rotating the sensor and the EM coil in the Earth's magnetic field. Reasonably robust operation of fast-recovery-during-EM-pulses is demonstrated. In practical applications, the EM pulses generate much bigger magnetic fields than 5 μT tested here. However, as discussed before, for any useful interpretation of the field reading during the pulse, the EM pulse has to be locally compensated at the location of the sensor. The pulse field after compensation should ideally be much less than 5 μT. Otherwise the heading error during the pulse is too much, as demonstrated in Figure 56.

### 7.4. Discussion and Conclusion

In this section, we have demonstrated the fast-recovery of MFAM operation in presence of EM pulses. Fast-recovery-after-EM-pulse method is first implemented in MFAM digital circuit. The magnetometer is shown to respond to a small signal less than one millisecond after the EM pulse is switched off, when operating in the optimal background magnetic field direction. Less than two milliseconds recovery times can be expected over the entire operating orientations of the magnetometer in the Earth's magnetic field. We also successfully demonstrate the simultaneous operation of MFAM with a commercial TDEM system. The negative effect of the EM pulse on the MFAM operation is shown to be minimized. We expect MFAM to function well as long as the pulse frequency of the TDEM system is less than 100 Hz, i.e. the off-time of the EM pulse is more than 2.5 ms assuming bi-polar EM pulses. Previous efforts in simultaneous magnetometer and EM system researches [1, 2, 3] require interleaving magnetometer and EM system data acquisition. In our method, the magnetometer and the EM system can be operated independently, which greatly simplifies the system integration of the two devices. In addition, the combined system can have much higher sample rate than that in the previous researches. By combining the angle measurement method, demonstrated in Section 6., and the fast-recovery method, we are also able to achieve the fast-recovery of MFAM operation during EM pulses. Reasonably robust operation is demonstrated when the integrated system of MFAM and the EM coil is rotated in the Earth's magnetic field.

## 8. UXO Discrimination Enhancement Using Quasi-DC Magnetic Field

### 8.1. Local Field Cancellation Scheme

As discussed in Section 4.5., when the quasi-DC magnetic field is applied, cancellation of the field is required at sensor location in order to minimize the motion-induced measurement error during practical surveys. In addition, to save survey time, simultaneous operation of multiple sensors is necessary. Since the sensor performance is greatly degraded under high magnetic field gradient (> 300 nT/cm for MFAM), it is important to keep the local field as uniform as possible. We wrote a simulation program to calculate the magnetic field at any location generated by a rectangular coil. The coil is first decomposed into small segments. Magnetic field generated by each segment is calculated according to the Biot-Savart law. The segment fields are then vector summed to achieve the field generated by the coil.

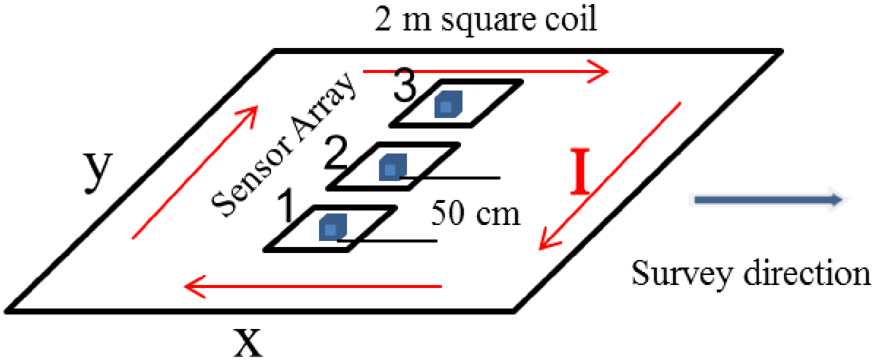

Figure 57 Coil configuration for quasi-DC magnetic field generation.

With the magnetic field simulation program, we tried many different coil configurations. The most promising one is shown in Figure 57, based on its simplicity and effectiveness (presented in the following sections). The coil system is consisted of one large square coil with a 2 m side length, centered at (0, 0, 0), and three small square coils with ~20 cm side length (results from different side lengths will be presented). Three sensors are each located inside one small coil. The middle sensor is also at the center of the large coil with two other sensors separated by 50 cm each from the center in y direction.

### 8.2. Magnetic Field Simulation Using Biot-Savart Law

We first set the side length of all small coils to be 20 cm and adjust both currents in the coils and small coil locations to achieve both low fields and low gradients at all sensor locations. If we have 400 A current in the large coil and -48.75 A, -40.61A and -48.75 A in three small coils located at (0, -49.3 cm, 0), (0, 0, 0) and (0, 49.3 cm, 0), respectively, both field magnitude and gradient can be minimized at three sensor locations. We assume all coils have only a single turn of wire in the simulation. In practice more turns can be added to the coils with proportionally less current. Magnetic field distributions at sensor 1 and sensor 2 (field at sensor 3 should be the same as that at sensor 1 due to symmetry) are plotted in Figure 58 (a) and (b), respectively. At each location, field distributions across x-y, x-z and y-z planes are shown in left, middle and right plots, respectively. In Figure 58, the magnetic field unit is Tesla and the length unit is meter. As can be seen, at all three sensor locations, the field magnitude is much smaller than 100 nT and the field gradient is much less than 100 nT/cm.

One issue with the above coil configuration is the need for independent current control for each coil, which can be challenging in practice. Therefore we simulate another coil configuration with 50 A current in all coils. The large coil has the same dimension but with 8 turns (so the same total current as before). The small coils have different side lengths. Two outer coils have a side length of 20.4 cm and the center one 24.6 cm. The coil centers are at (0, -49.4 cm, 0), (0, 0, 0) and (0, 49.4 cm, 0), respectively. With this set of parameters, magnetic field distributions at sensor 1 and sensor 2 (field at sensor 3 should be the same as that at sensor 1 due to symmetry) are plotted in Figure 59. As can be seen, similar results are achieved compared with the plots shown in Figure 58.

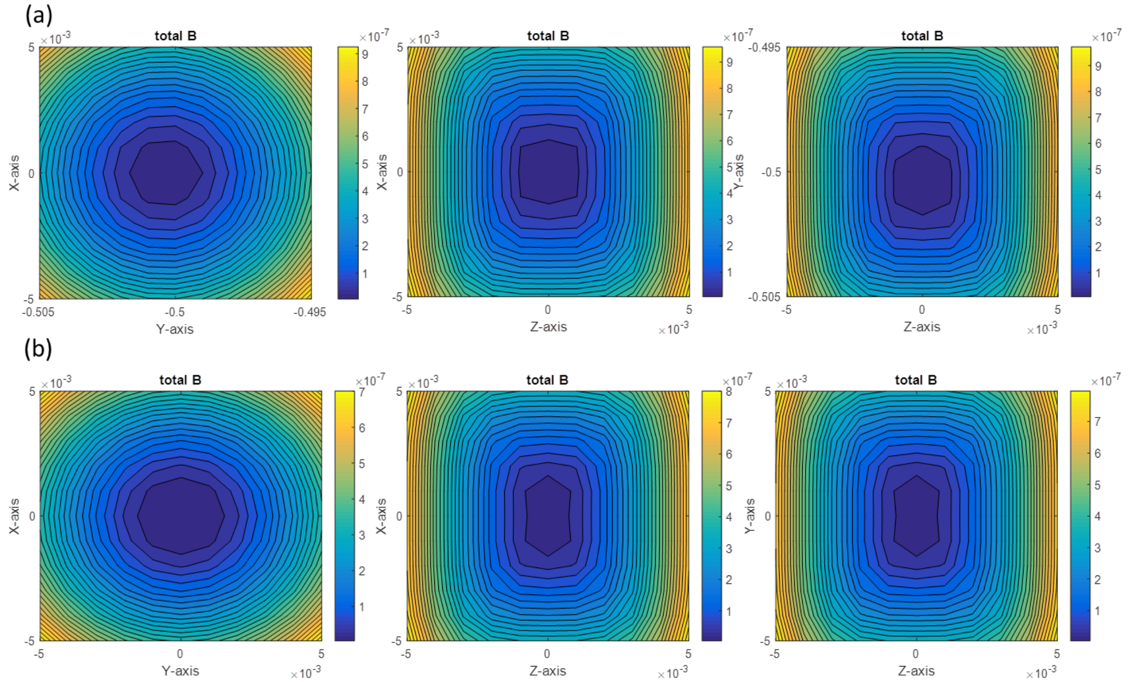

**Figure 58 Simulated magnetic field at sensor 1 (a) and sensor 2 (b) for 400 A current in the large coil and -48.75 A, -40.61A and -48.75 A in three small coils located at (0, -49.3 cm, 0), (0, 0, 0) and (0, 49.3 cm, 0), respectively. Left, middle and right plots are for field distribution across x-y plane, x-z plane and y-z plane, respectively. The magnetic field is in unit of Tesla and the length is in unit of meter.**

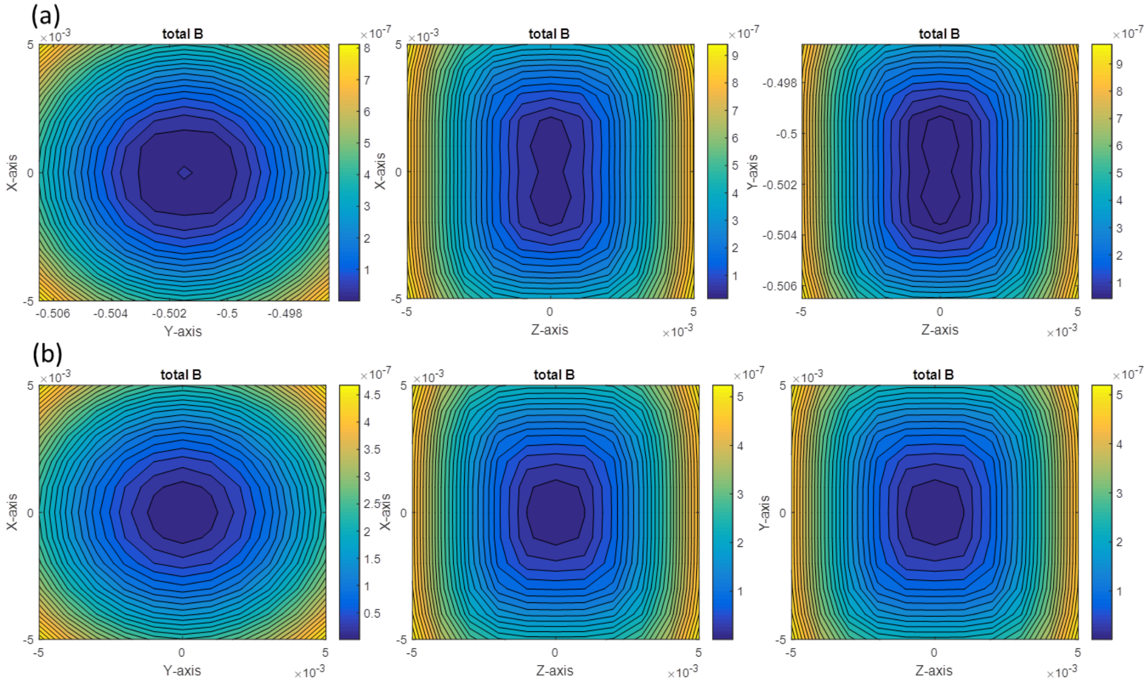

**Figure 59 Simulated magnetic field at sensor 1 (a) and sensor 2 (b) for 50 A current in all coils. The large coil has 5 turns. Three small coils have different sizes and are located at (0, -49.4 cm, 0), (0, 0, 0) and (0, 49.4 cm, 0), respectively. Left, middle and right plots are for field distribution across x-y plane, x-z plane and y-z plane, respectively. The magnetic field is in unit of Tesla and the length is in unit of meter.**

### 8.3. Magnetic Anomalies Due to Quasi-DC Excitation

We simulate the magnetic anomalies of five different objects (including three objects shown in Figure 30) exposed to the quasi-DC excitation. The excitation is generated by the coil configuration shown in Figure 57 with coil parameters given by those corresponding to Figure 59. When the excitation is off, all five anomalies are almost the same, leading to the ambiguity in UXO discrimination and classification. In this section, we will show that the quasi-DC excitation can indeed remove the ambiguity in the magnetic anomaly data.

The simulation is based on the theoretical model described in the Technical Approach section. The excitation field by the coil system is added to the model. After calculating the induced field by the object, total magnetic fields at three sensor locations are computed by a simple vector sum of the background magnetic field, residual excitation field and the induced field. This calculation repeats after the coil system is moved to the next location. We assume that the survey is along x direction. After finishing one line of survey (three actual lines from three sensors), the coil system is displaced by 1.5 m in y direction. The next line of survey resumes. Simulated survey data has a grid size of 0.2 m along x direction and 0.5 m along y direction. The results are shown in Figure 60 with a constant background magnetic field removed. The unit of the field is Tesla. Figure 60 (a), (b) and (c) correspond to three objects shown in Figure 30 (a), (b) and (c), respectively. Objects in (d) and (e) have parameters ($a$ = 32.7 cm, $e$ = 0.31, θ = 176.6°, φ= 0°) and ($a$ = 13.8 cm, $e$ = 5, θ = 114°, φ= 0°), respectively. All objects are centered at the same location of (2m, 2m, -0.7m). As seen in Figure 60, magnetic anomalies under the quasi-DC excitation are quite different. This additional data (data shown in Figure 30 can always be acquired when the coils are off) can now be used in UXO discrimination and classification. In practice, we can even apply different currents to the coils to generate different quasi-DC excitations to obtain more information.

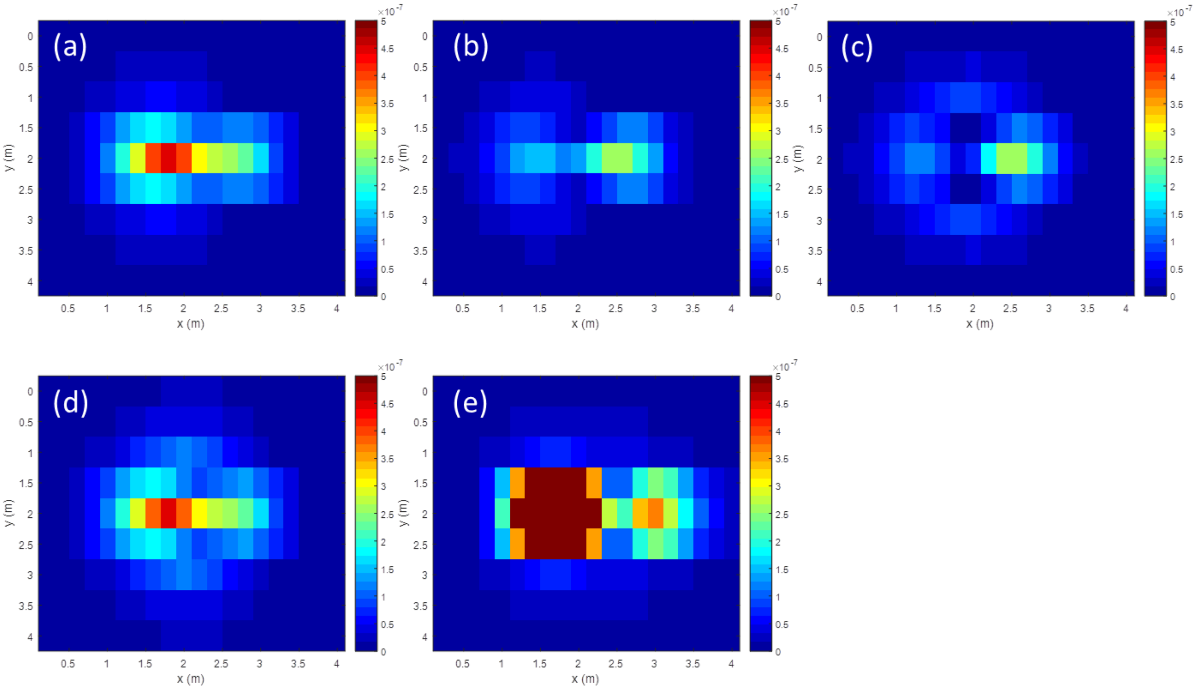

Figure 60 Magnetic anomalies measured by the instrument shown in Figure 57. We assume that the instrument is moving in x direction. Therefore the grid size along y direction is 0.5 m, defined by the sensor separation.

## 8.4. Practical Challenges

In this section, we want to investigate the feasibility of achieving the field cancellation shown in Figure 59 with a coil system shown in Figure 57. We will slightly alter the coil parameters and simulate the resulting field distribution around the sensor location. In practice, it is relatively easy to have a precise and stable current source but the coil size and position may not be exactly the same as designed. Therefore first we change the small coil 1 side length from 20.4 cm to 20.5 cm. The result is shown in Figure 61 (a). At the sensor 1 location, magnetic field cancellation no longer works as well. However, good field cancellation is still possible with the new side length. After the center of the coil is moved from (0, -49.4 cm, 0) to (0, -48.8 cm, 0), local field is minimized again, shown in Figure 61 (b). We also notice that the minimum field location is changed, which means that the sensor location needs to be changed as well.

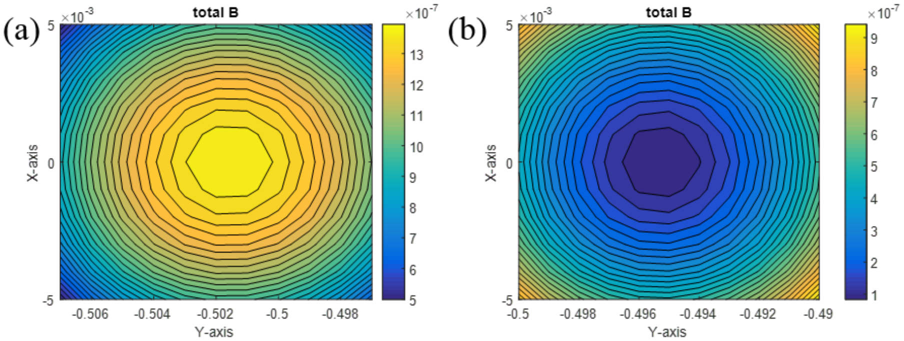

**Figure 61 Magnetic field distribution around sensor 1 with different coil parameters. In (a) coil 1 side length is changed from 20.4 cm to 20.5 cm. Field cancellation is greatly degraded. However, good field cancellation can still be achieved with the 20.5 cm side length coil, as seen in (b) after the coil center is moved from (0, -49.4 cm, 0) to (0, -48.8 cm, 0). Note that the sensor location also has to be moved accordingly.**

## 8.5. Discussion and Conclusion

We have shown in this section that the quasi-DC excitation method can indeed enhance the UXO discrimination and classification. Although it is definitely challenging to design and construct a coil system for the quasi-DC excitation, we have shown the possibility of offsetting the effect of imperfect coil sizes with different coil locations. By carefully designing an adjustable coil location system, a practical instrument is achievable. However, we are concerned that pursuing this application may consume us too much in the initial construction and evaluation of the coil system and at the end leave us with limited resource towards the main goal of this project, which is to demonstrate MFAM operation in presence of EM pulses in field applications. Therefore we decided to investigate the other new method for UXO detection and discrimination: low frequency AC magnetic field excitation.

# 9. Low Frequency AC Magnetic Field Excitation

## 9.1. Aluminum Targets

The experimental setup for testing the low frequency AC field excitation method is schematically shown in Figure 62. As seen in the plot, two MFAM sensors are separated by 5 inches vertically. AC magnetic fields are generated by a 10-turn coil with a radius of 5 inches. Using an arbitrary function generator and frequency modulation, multi-frequency sinusoidal magnetic fields can be mixed and applied at the same time to a moving target below the sensors. The maximum peak-to-peak amplitude of the applied field at 100 Hz is 5 μT at the center of the coil. This is determined by the slew rate of the MFAM sensor. The MFAM readings are recorded and analyzed using MatLab code. The phase information is extracted by first demodulating the MFAM reading at the reference frequency. The X and Y components out of the demodulator are then low-pass filtered at 5 Hz. Finally the phase is calculated based on the trigonometry from the filtered X and Y components. The phase difference between two MFAM sensors will be used as a signal to detect nearby metal targets. The phase difference can also be converted to the time delay through a simple division of 360 degrees and a multiplication with the reference signal period.

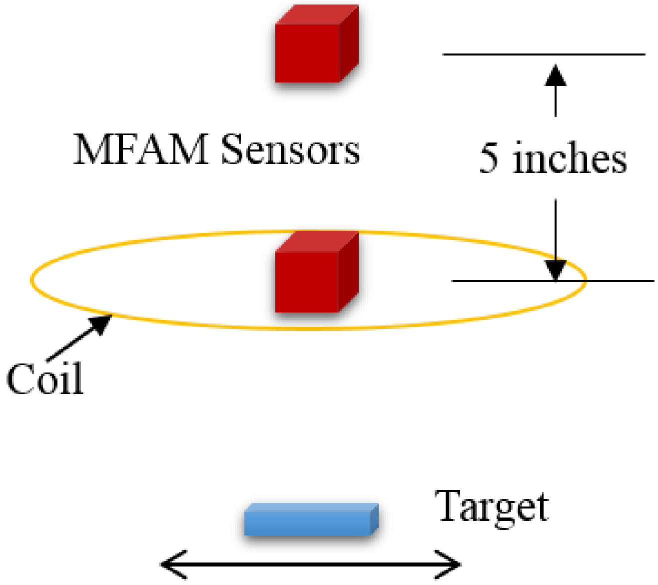

Figure 62 Schematic of a low frequency AC field excitation setup.

We first test the method with a 2 x 2 x 0.5 inches aluminum block moving at about 0.1 m/s on a surface 5 inches below the coil. The exciting AC field has a center carrier frequency of 100 Hz and two main sidebands at 30 Hz and 170 Hz. The time delay is calculated for each frequency and plotted in Figure 63 as a function of time, during which the aluminum block passes the MFAM setup 3 times. As seen in the plot, when the target is far away from the setup, the time delay is almost zero because both MFAM sensors measure the oscillating fields from the same source. When the target is nearby, the secondary field generated by the target is much stronger at the bottom sensor than that at the top one. As a result, the time delay increases. As discussed in Section 5., the skin depth is larger when the exciting field frequency is lower. For aluminum, the skin depth is about 8 mm at 100 Hz. If the thickness of the aluminum block is larger than the skin depth, we expect to see an increase in the signal time delay. This is what we observe for the 0.5 inch thickness aluminum target, as shown in Figure 63. If the thickness of the target is much less than the skin depth, the signal time delay will be limited by the material thickness instead and become independent of the excitation field frequency. We perform the same test with a 2 x 2 x 0.1 inches aluminum block. The results are plotted in Figure 64. As expected, the time delay does not change even when the excitation field frequency changes. In principle, this method can be used to measure the thickness of non-magnetic material. Note that at 30 Hz the time delay has much worse noise. This is due to the background magnetic field fluctuations which tend to be much bigger at lower frequencies.

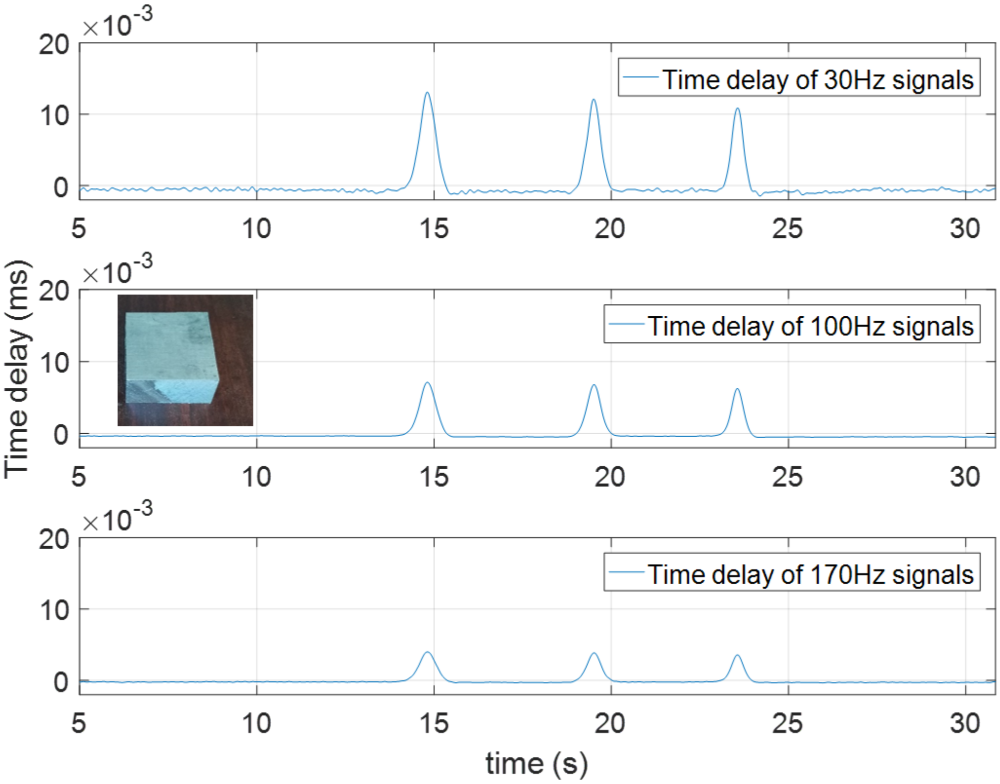

Figure 63 Signal time delay as a function of time while the thick aluminum block passing the MFAM setup 3 times.

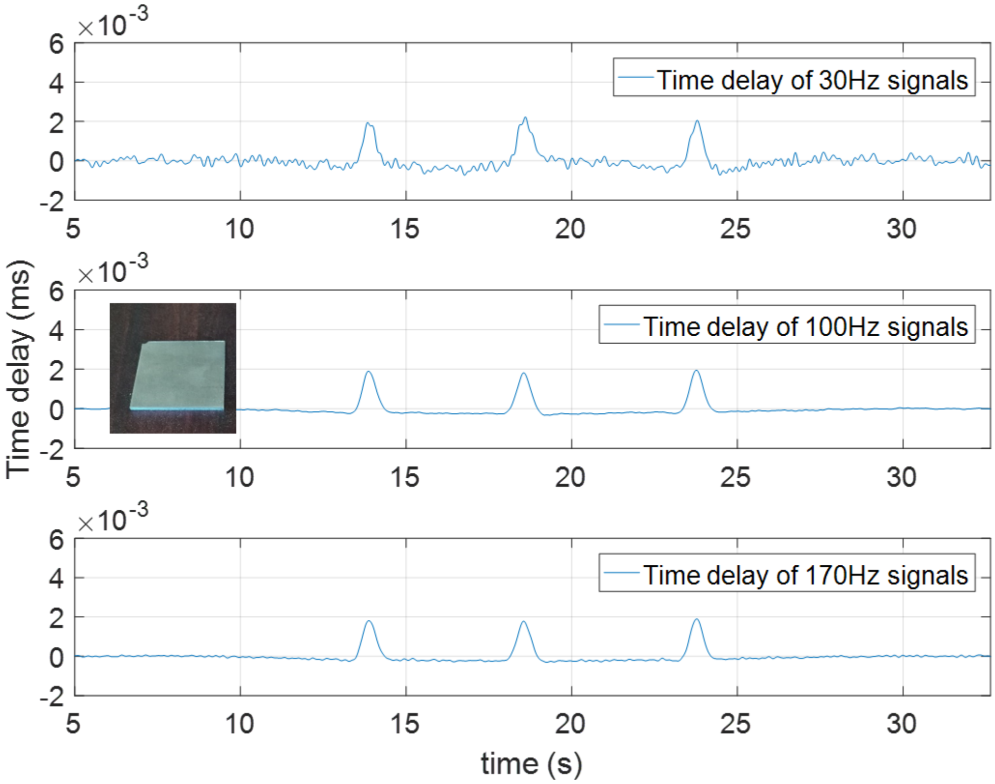

Figure 64 Signal time delay as a function of time while the thin aluminum block passing the MFAM setup 3 times.

### 9.2. Magnetic Targets

Due to the magnetic hysteresis phenomenon and much smaller skin depths, magnetic targets display very different behavior in terms of their excitation frequency responses. We repeat the test with a cylindrically shaped can made of magnetic material. It has a length of 4.5 inches and a diameter of 3.5 inches. We passes the can back and forth underneath the MFAM setup 3 times, each time with a different orientation indicated by the pictures in the top graph of Figure 65. The signal at 30 Hz is overwhelmed by the noise and not shown here. The time delay at 240 Hz is included. The noise is worse because the 240 Hz excitation field has a much smaller amplitude. As seen in Figure 65, the time delay even increases with higher excitation frequencies. We do not have a good explanation to the dependence of the frequency response on the target orientation.

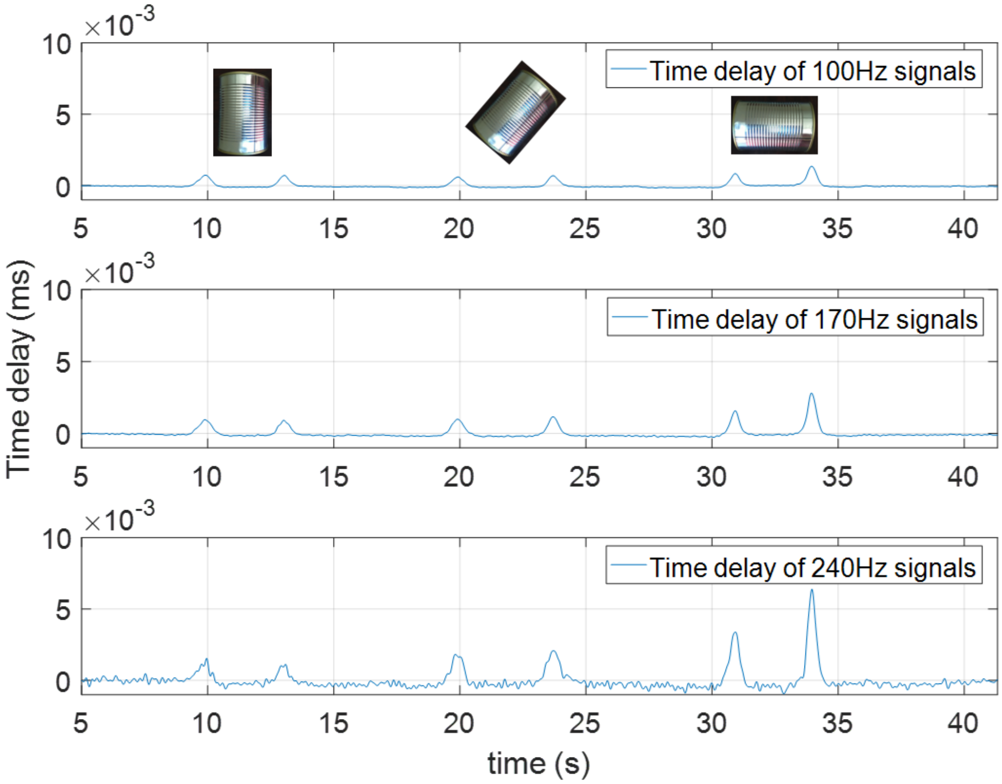

Figure 65 Signal time delay as a function of time while the can passing the MFAM setup back and forth 3 times, each time with a different orientation indicated by the pictures in the top graph.

### 9.3. Discussion and Conclusion

In conclusion, we present the lab results of the low frequency AC magnetic field excitation method. Our work demonstrates that this method enables MFAM magnetometers to detect non-magnetic targets. In addition, by exciting targets with different frequencies, target parameters, such as the material thickness, may be extracted from the frequency response of the time delay signal. On the other hand, the magnetic method is still better in detecting magnetic targets. Whether additional useful information can be extracted from the low frequency AC magnetic field excitation method for magnetic targets is still unclear and needs further investigation.

# 10. Field Testing Results

## 10.1. Dead-zone and Heading-error Issues

There are two main challenges using MFAM sensors in real-world field applications: dead-zone and heading-error. The strength of the magnetic sensing signal, Larmor signal, depends on the relative angle between the optical path of the sensor and the background magnetic field, due to the fundamental physics behind the sensor operation. The Larmor signal decreases and eventually disappears when the optical path of the sensor approaches the background magnetic field direction. This is called polar dead-zone. For our MFAM sensors, the polar dead-zone is about ± 25° with respect to the optical path. Even when the sensor is outside the dead-zone, the magnetic field reading of the sensor slightly depends on the relative orientation of the sensor with respect to the background magnetic field. This is called heading-error of the sensor. Many factors contribute to the heading-error, such as nonlinear Zeeman-shift of alkali atoms, light-shift effect [7] and orientation-dependent phase change in Larmor signal.

In Figure 66, we show a typical measurement of the dead-zone and the heading-error of MFAM sensors. The optical axes of two sensors are initially aligned along the background magnetic field direction, as shown in Figure 66 left. The sensors are then rotated with the rotation axis perpendicular to the field. The magnetic field readings of the sensors are recorded as a function of rotation and shown in Figure 66 right. A constant offset is applied to the magnetic field reading. As can be seen, when sensor optical axes are aligned close to the magnetic field direction, the sensor readings drop. The sensors are in the dead-zone. Outside the dead-zone, although the background magnetic field does not change, the sensor field readings still vary due to the heading-error. Typical heading-error is about 60 nT for MFAM sensors.

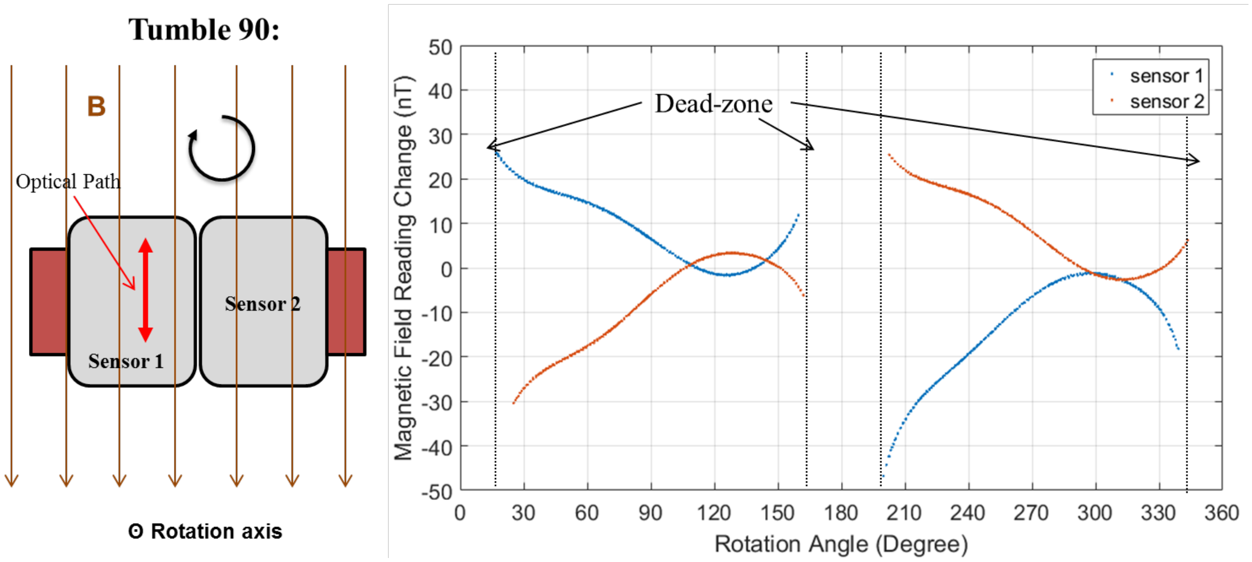

**Figure 66 Measurement of the dead-zone and the heading-error. Left: schematic showing the rotation of the sensor in the background magnetic field. Right: sensor output (with a constant offset) as a function of sensor rotation.**

MFAM driver can operate two MFAM sensors at the same time. Therefore we can orient two sensors orthogonally, as shown in Figure 67, and combine the Larmor signals of two sensors as a single signal input. In this configuration, the combined Larmor signal will never disappear under any sensor orientation since one of the sensors will always be outside its dead-zone. It turns out that the heading-error of the combined sensor is also much smaller compared with the data shown in Figure 66. The magnetic field gradient tolerance of the combined sensor, however, is greatly reduced to about 50 nT/inch. Nevertheless, in most field applications, the background magnetic field gradient should still be within this limit.

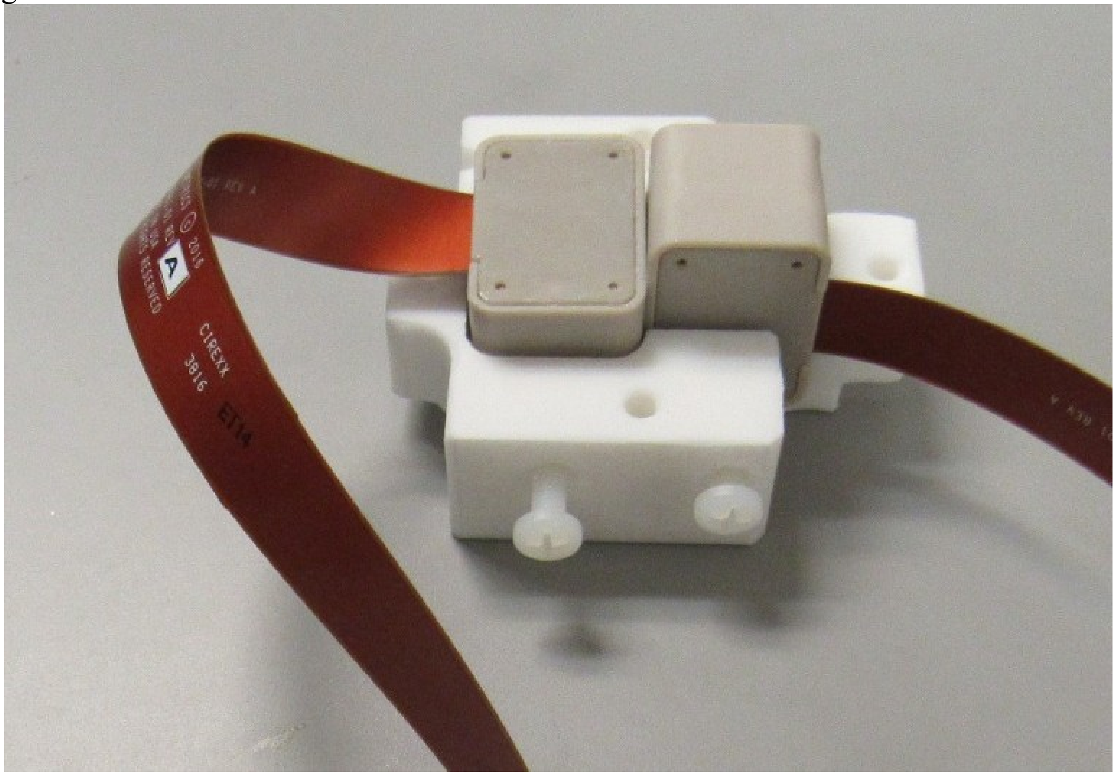

**Figure 67 Orthogonal orientations of two sensors for dead-zone-free operation by combining the signal inputs of two sensors. The heading-error in the combined operating mode in this configuration is also greatly reduced.**

We perform similar measurements to the one shown in Figure 66 with the combined sensor. Three orthogonal rotation axes are chosen such that during each rotation at least one sensor optical axis will overlap with the magnetic field lines. In the single sensor mode, this will cause the sensor to enter the dead-zone. However, due to the orthogonal configuration of two sensors, the other sensor should be at the optimal orientation, where its optical axis is perpendicular to the magnetic field direction. The dead-zone and heading-error measurement results around the three orthogonal rotation axes are plotted in Figure 68. The two sensors here are the same ones used for results in Figure 66. As shown, the combined sensor has no dead-zone. The heading-error is also greatly reduced from 60 nT to about 12 nT, a factor of 5 improvement. The heading-error reduction is achieved mainly by cancelling out the orientation-dependent phases when the two Larmor signals are combined and by avoiding the sensor operation close to the dead-zone where the magnetic reading is affected more by side effects since the Larmor signal is small.

We demonstrate a combined two-sensor configuration which not only eliminates the dead-zone issue of a single magnetometer but also greatly reduces the heading-error of the sensor. The MFAM configuration shown in Figure 67 will be used in the field test. In field applications, the remaining heading-error can be further reduced by heading-error compensation techniques.

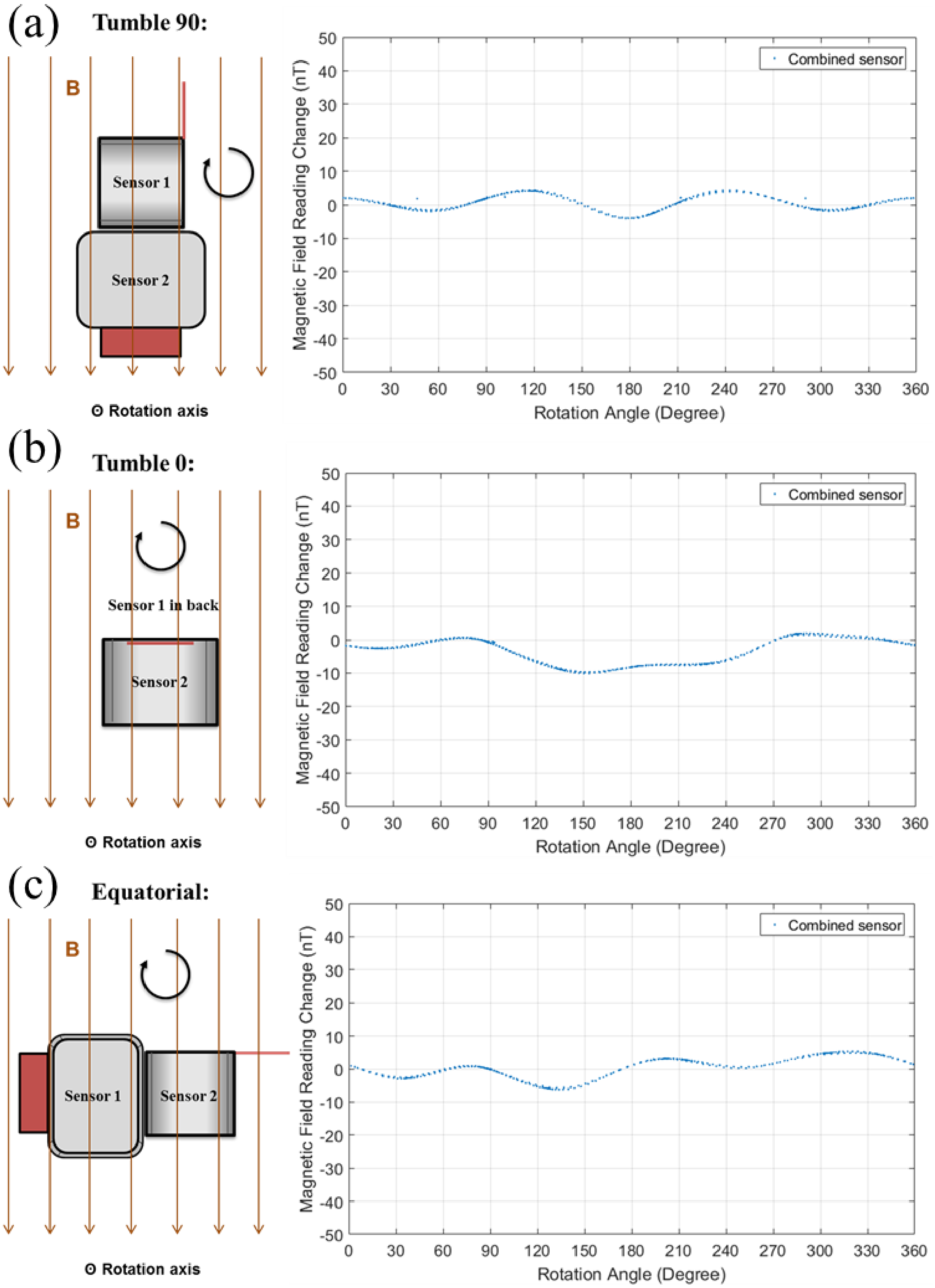

Figure 68 Heading-error measurements of the combined sensor. Three different rotation axes are chosen such that during the rotation at least one sensor optical axis can overlap with the magnetic field.

### 10.2. Testing Site Selection and Qualification

We choose a drive way at NASA Ames Research Center as the testing site since it is located in a relatively remote area, far away from buildings and major roads. A magnetic field survey covering the drive way is first conducted to map the spatial background field variation. The survey covers an area of 100 x 30 feet. The site and the survey result is shown in Figure 69. As can be seen, on both ends of the drive way, there are large magnetic anomalies which we will need to avoid for the testing. The final selected testing site is located between 50 and 90 feet in the long direction and between 5 and 20 feet in the short direction. Within this 40 x 15 feet area, the spatial field change is less than 100 nT.

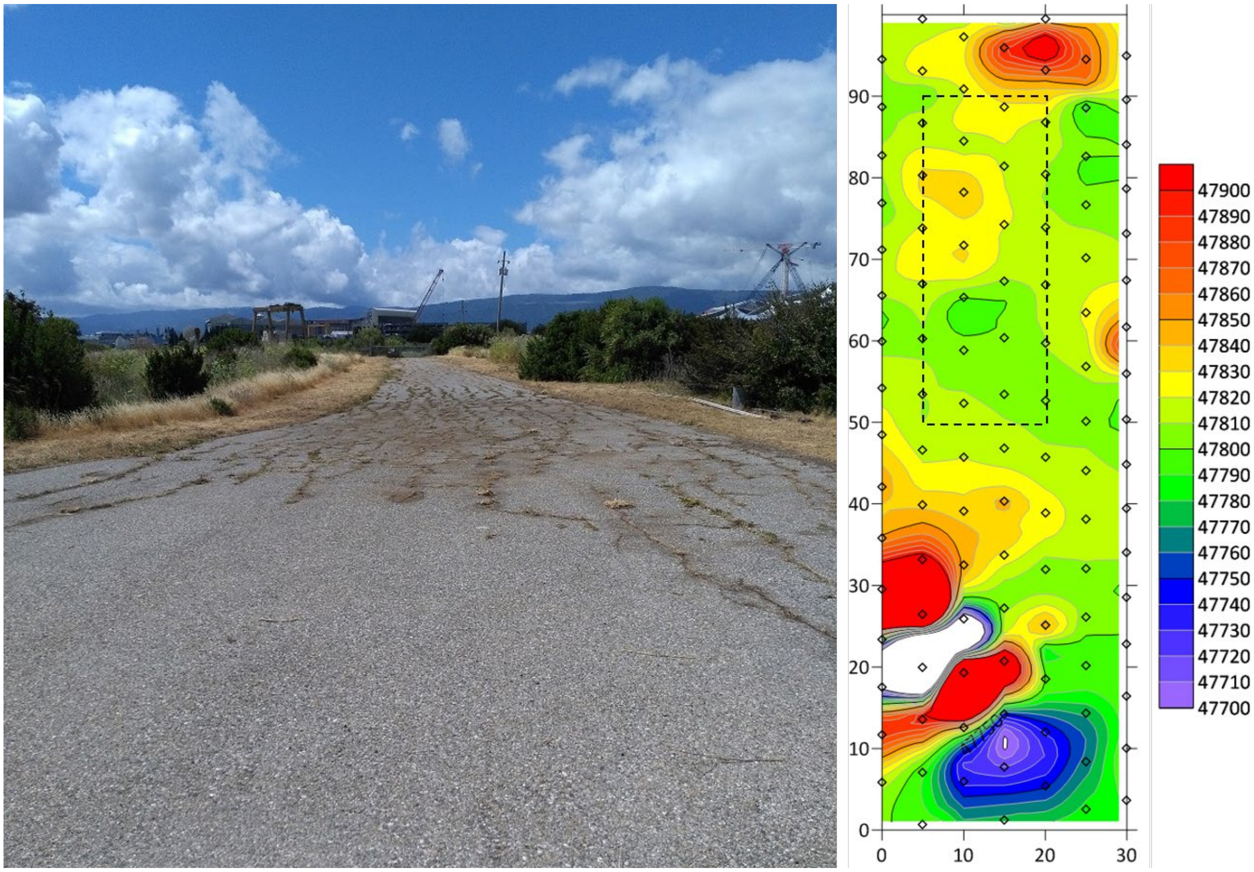

**Figure 69 NASA testing site and its magnetic survey result. The field reading in nT is represented by the color scale on the right. The selected survey area is indicated by the dash lines.**

### 10.3. Magnetic Field Survey in Presence of EM Pulses

We combine an EM transmitter with the MFAM sensors and integrate the system to a customized non-magnetic survey cart. The square-shaped 10-turn transmitter coil has a side length of about 2 feet and is about 1.5 feet above the ground. The sensors are located at the center of the transmitter coil. We use an arbitrary function generator to create pulses for the transmitter coil. The pulse has an amplitude of more than 5 μT at the location of the sensor and rising and falling edges of less than 10 μs. The MFAM data is logged using a computer. Since the function generator and the computer are quite magnetic, we need another cart to carry these instruments together with the battery and follow the sensor cart about 15 feet away. The setup is shown in Figure 70.

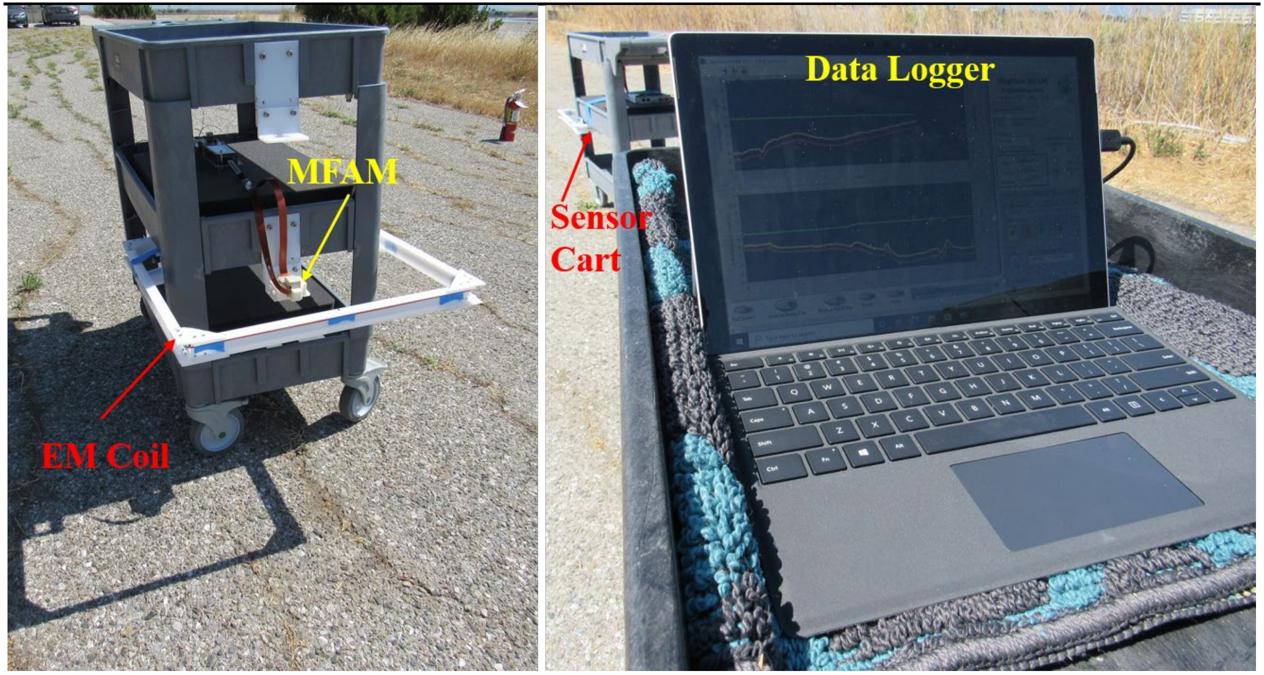

**Figure 70 Advanced magnetometer setup. The system has an EM transmitter coil and the MFAM sensors. The data logger computer and the pulse generator is located in another cart 15 feet away.**

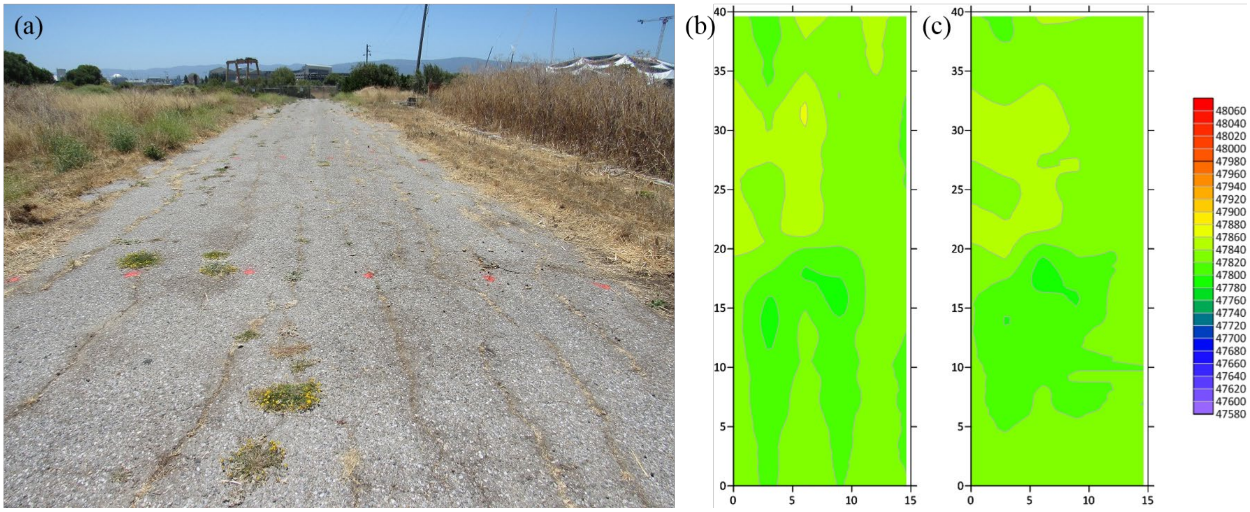

**Figure 71 (a) Survey site with red painted spots as markers for positioning. (b) Raw background magnetic field survey result. (c) Background magnetic field survey result after heading error compensation.**

The survey site is covered by 6 40-feet long lines with 3 feet line spacing. We mark each line with 3 spots painted with red color and separated by 20 feet, as shown in Figure 71 (a). When the MFAM sensors pass a spot, a voltage pulse is sent manually to the data logger system to record the position of that spot together with the MFAM reading. The position along the line is then interpolated assuming a constant speed between two spots. A magnetometer base-station is also set up (not shown here) to record the diurnal field change. The result presented is always after the base-station correction. We first conduct the background survey. After collecting the 3 kHz MFAM data, a low pass filter at 5 Hz is applied to remove high frequency noises. The resulting raw data is shown in Figure 71 (b). As discussed in Figure 68, there is still heading-error associated with the MFAM. The heading-error effect can be detected in Figure 71 (b). However, after a constant offset is added or subtracted from each line depending on the heading, the heading-error is mostly removed, as shown in Figure 71 (c). In the following report, the results are always heading-error compensated.

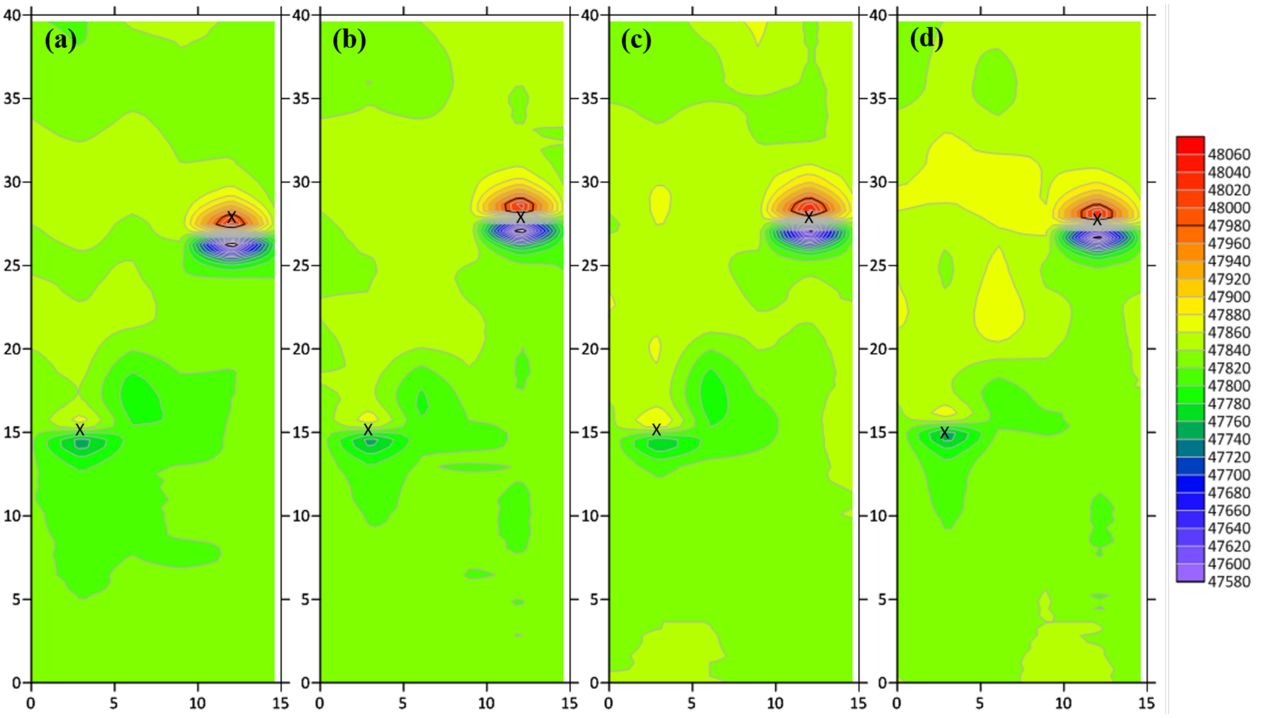

**Figure 72 Magnetic field survey results with two targets. (a) Without EM pulses. (b) With 50 Hz EM pulses. (c) With 100 Hz EM pulses. (d) With 200 Hz EM pulses. The color scale is given on the right in unit of nT. The target locations are marked by "x". Due to the positioning inaccuracy, the magnetic field survey results do not always overlap with the target locations.**

After the background survey, two magnetic targets (1.375 inch in diameter and 4.5 inch long) are placed on the survey site along the same direction. We first repeat the survey without turning on the EM pulses. The survey result is shown in Figure 72 (a). Two targets can be clearly located in the survey map. One target has much higher magnetic signature due to its inherent magnetic properties. The real target locations are indicated by the marker "x". Due to the positioning error, the target location from the magnetic field survey is off. The EM pulses are then turned on during the survey. All pulse waveforms have 50% duty cycle. The frequency of the first waveform is set at 50 Hz. After collecting the raw MFAM data, the missing readings during the EM pulse on are interpolated based on the valid MFAM data. The 5 Hz low pass filter is then applied to the data set. The resulting MFAM survey data with 50 Hz EM pulses is plotted in Figure 72 (b). Compared with the data without the EM pulses in Figure 72 (a), the magnetic field survey is not impacted much by the 50 Hz EM pulses. We also apply 100 Hz and 200 Hz waveforms. The corresponding MFAM survey results are plotted in Figure 72 (c) and (d), respectively. These two data sets show that MFAM still generates valid magnetic field readings in presence of EM pulses up to 200 Hz. The raw MFAM readings as a function of time is plotted in Figure 73. With the 200 Hz EM pulses, the pulse-off time is 2.5 ms. Minus the recovery time, the field measurement time is only about 1 ms, as shown in the zoom-in plot in Figure 73. Therefore 200 Hz is about the highest EM frequency the MFAM can be operated with. For bi-polar EM pulses, the maximum allowed frequency is about 100 Hz.

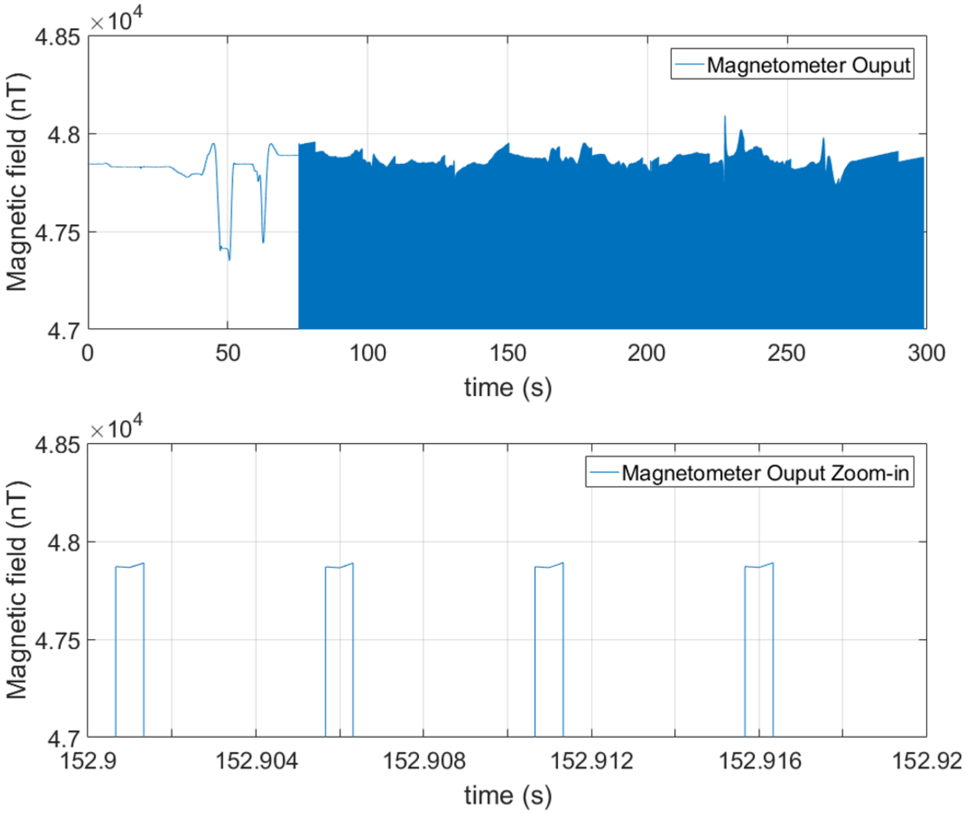

Figure 73 Raw MFAM readings with 200 Hz EM pulses.

## 10.4. Low Frequency AC Field Excitation

Figure 74 (a) MFAM sensor configuration for the low frequency AC field excitation method. (b) Survey site with targets. Compared with the site in Figure 72, 5 more targets were added. Among them, four are made of aluminum.

A gradiometer setup is needed for the low frequency AC field excitation method. The coil position is kept the same. But the two MFAM sensors are separated with one moving up by about 10 cm and the other down by 10 cm. The new sensor configuration is shown in Figure 74 (a). Since the sensor position is changed, the background magnetic field survey is repeated again. We then place 7 targets on the survey site, three magnetic ones and four non-magnetic ones. Detailed target properties are listed in Table 1. All three magnetic targets have similar size and shape (1.375 inch in diameter and 4.5 inch long). Target 1 and 2 have similar magnetic signatures while the magnetic signature of target 3 is much larger due to its inherent magnetic properties. Both target 1 and 3 are placed horizontally with their symmetric axes along the drive way direction while target 2 is placed vertically. Target 1 and 3 are used in Figure 72. Four non-magnetic targets are made of aluminum. Target 4 and 5 are square-shaped (2 x 2 inches) with less than 5 mm in thickness. Target 6 and 7 are cylindrically shaped with 2.5 inches in diameter but different lengths (0.5 inch and 2.5 inches). The targets are shown in Figure 74 (b).

**Table 1 Target properties.**

| Target | Location (short x long direction) | Shape and Size | Magnetic Property and Orientation |
|---|---|---|---|
| 1 | (3 ft x 15 ft) | Cylindrical, 1.375″ in diameter 4.5″ in length | Magnetic, symmetric axis along drive way direction |
| 2 | (6 ft x 37 ft) | Cylindrical, 1.375″ in diameter 4.5″ in length | Magnetic, symmetric axis in vertical direction |
| 3 | (12 ft x 25 ft) | Cylindrical, 1.375″ in diameter 4.5″ in length | Magnetic, symmetric axis along drive way direction, much larger magnetic signature than the other two |
| 4 | (6 ft x 30 ft) | Square, 2″ in side length, 0.15″ in thickness | Non-magnetic, aluminum, square side facing up |
| 5 | (6 ft x 26 ft) | Square, 2″ in side length, 0.1″ in thickness | Non-magnetic, aluminum, square side facing up |
| 6 | (9 ft x 15 ft) | Cylindrical, 2.5″ in diameter 2.5″ in length | Non-magnetic, aluminum, symmetric axis in vertical direction |
| 7 | (9 ft x 9 ft) | Cylindrical, 2.5″ in diameter 0.5″ in length | Non-magnetic, aluminum, symmetric axis in vertical direction |

With the targets, we conduct two surveys: one without the AC field excitation and the other with a 100 Hz 5μT peak-to-peak sinusoidal field at the center of the coil. The data processing procedure is the same as described in the previous section. The magnetic field survey results using the bottom MFAM sensor for the background, the targets and the targets with the 100 Hz excitation field are shown in Figure 75 (a), (b) and (c), respectively. The color scale is given on the right in unit of nT. All targets are labeled according to Table 1 and their locations are marked by “x”. As seen in the plot, three magnetic targets are clearly detected and the 100 Hz excitation does not affect the survey result. Due to the positioning inaccuracy, the survey results do not always overlap with the target locations. Note that although target 1 and 2 are almost identical their magnetic signatures in the survey are very different due to the difference in their orientations with respect to the background magnetic field.

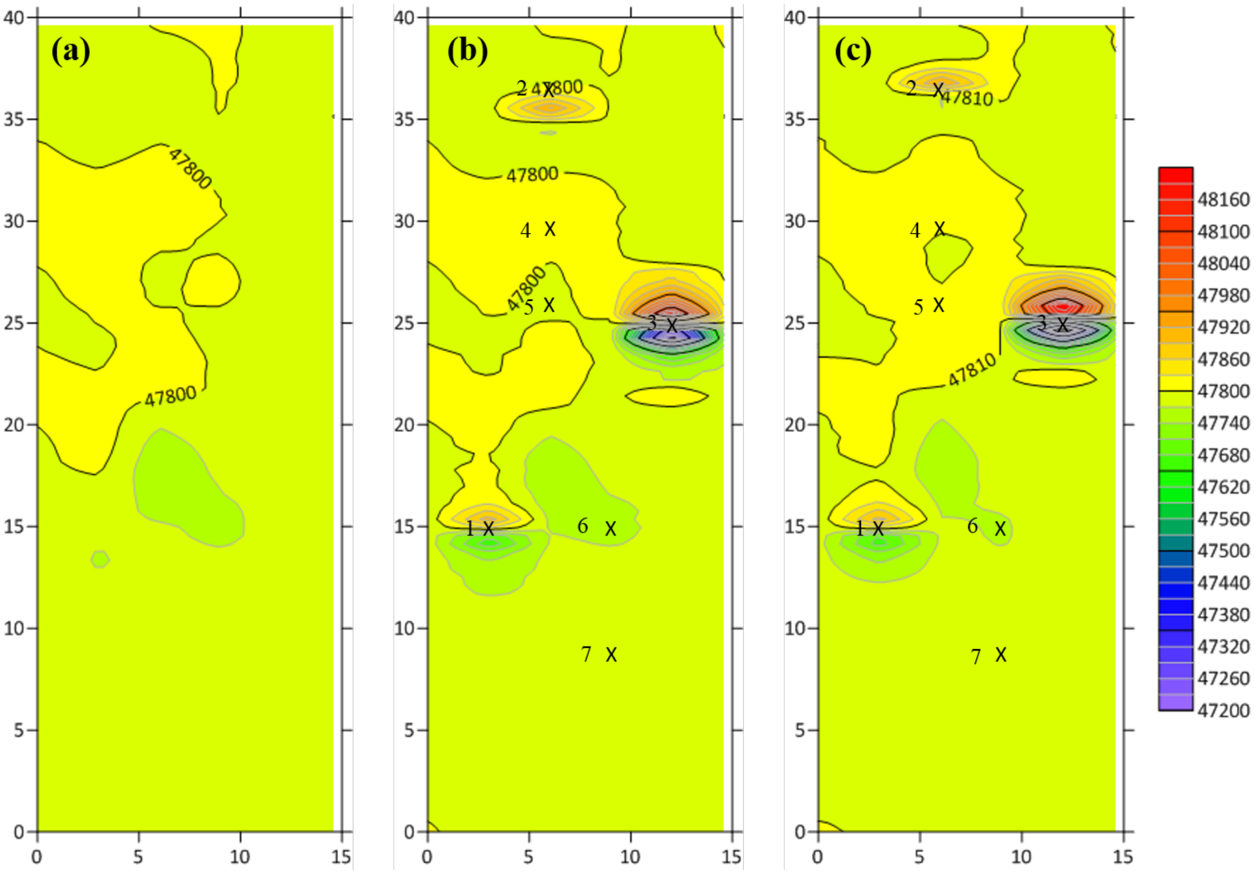

**Figure 75 Magnetic field survey result for (a) the background, (b) the targets and (c) the targets while the 100 Hz excitation is on. The targets are labeled and their locations are marked by “x”. Due to the positioning inaccuracy, the survey results do not always overlap with the target locations.**

Since there are two MFAM sensors separated by about 20 cm in the vertical direction, vertical magnetic gradient data is also collected at the same time. Compared with the magnetic field data, the vertical magnetic gradient data is less affected by the noise in the background. This is due to the fact that the gradient signal decreases much faster as a function of target distance than the total field signal. Thus it is more sensitive to nearby targets and less affected by magnetic clutters in the background which are further away. This advantage can be clearly seen in the corresponding vertical gradient data set plotted in Figure 76.

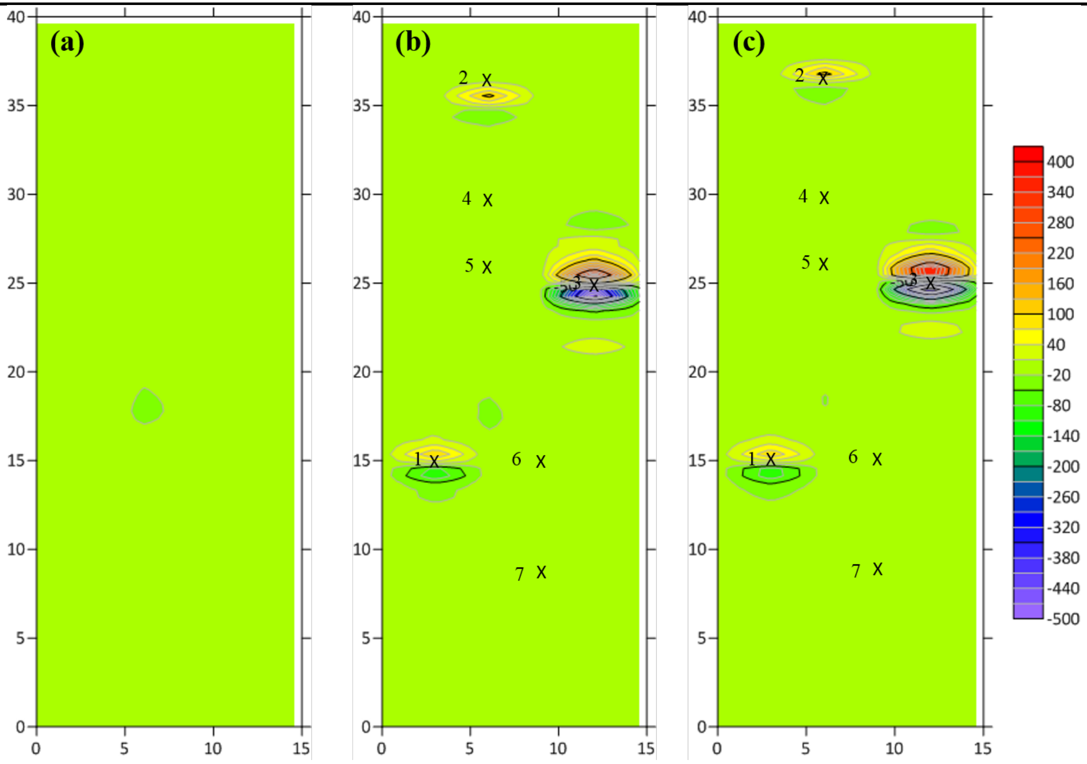

Figure 76 Vertical magnetic gradient survey result for (a) the background, (b) the targets and (c) the targets while the 100 Hz excitation is on. The color scale is in unit of nT. The targets are labeled and their locations are marked by "x". Due to the positioning inaccuracy, the survey results do not always overlap with the target locations.

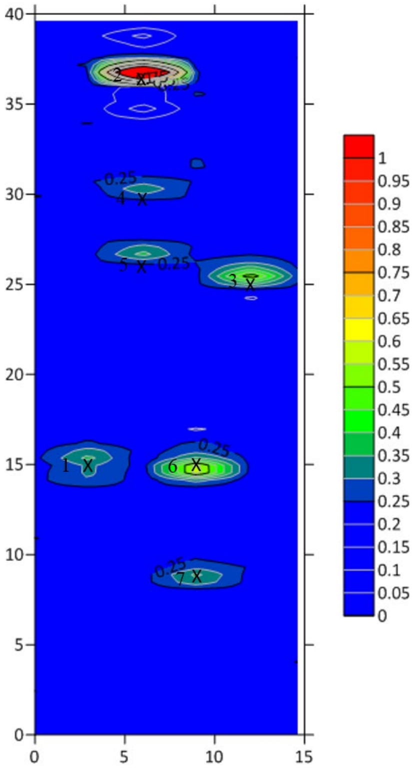

Figure 77 Target detection using the low frequency AC magnetic field excitation method. The color scale is in unit of µs. The targets are labeled and their locations are marked by "x". Due to the positioning inaccuracy, the survey results do not always overlap with the target locations.

From Figure 75 and Figure 76, it is obvious that non-magnetic targets cannot be detected by the traditional magnetometer methods. But with the low frequency AC field excitation method, all metal targets can be detected. The relative time delay of the 100 Hz signal between the top and the bottom MFAM sensor is calculated and plotted in Figure 77 in unit of µs. Now we can clearly see all seven targets. One interesting fact is that even for two magnetic targets with similar magnetic field or gradient amplitude (target 1 and 2), the time delay signal is very different. This is very likely due to the orientation difference between the two targets.

As discussed in Section 9., we can use different excitation frequencies, especially those lower than 100 Hz, to measure the wall thickness of the target. We try 30 Hz excitation frequency but find the time delay noise to be even worse than that in Figure 64. After some investigation, the reason is found to be the increased sensor noise associated with the sensor motion. Figure 78 shows the noise density for (a) the stationary sensors and (b) the moving sensors. As can be seen, there is almost a 10-fold increase in the gradient noise around 30 Hz, which directly affects the AC excitation method.

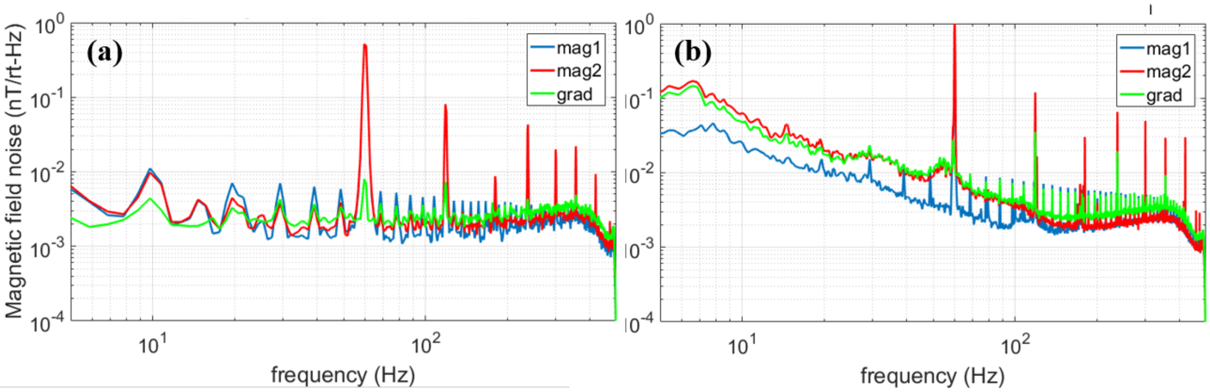

Figure 78 Noise density for two sensors and the gradient. (a) The cart is stationary. (b) The cart is moving.

### 10.5. Discussion and Conclusion

Many new issues arise when the MFAM sensors are used for field surveys. Two major ones are the dead-zone and the heading-error. We demonstrate a combined two-sensor configuration to eliminate the dead-zone issue and mitigate the heading-error issue. The remaining heading error can be further reduced by an adjacent-line-leveling technique, adding or subtracting a constant offset depending on the heading. We successfully conduct magnetic field surveys in presence of EM pulses up to 200 Hz in frequency. Compared with previous researches, this work develops advanced MFAM sensors that are capable of not only working with much higher EM pulse frequencies but also operating independently from the EM pulses. This will make the integration of the MFAM sensors with the EM system much easier. The low-frequency AC field excitation method is also studied in the field survey. The basic functionality of the method is verified. Both magnetic and non-magnetic metal targets can be detected through the time delay measurement of the AC field. However, the method’s efficacy in the UXO discrimination still needs further investigation, especially after the discovery of increased measurement noise in low frequencies associated with the sensor motion.

# Conclusions and Implications for Future Research

Taking advantage of two miniaturized MFAM sensors and their unique digital signal processing capability, we have developed an advanced atomic magnetometer system capable of magnetic field angle measurement and simultaneous operation with time-domain electromagnetic (TDEM) systems. New UXO detection and discrimination methods have also been explored. Our field testing results confirm that the project has met its objective, which is to enable integration of MFAM sensors with TDEM systems by improving the sensor to function in presence of an EM transmitter. Magnetic field surveys over the same site have been conducted and survey results with and without EM pulses have been compared. No obvious compromise is found in the MFAM sensor performance with EM pulses up to 200 Hz in frequency. On the other hand, although the magnetic field angle measurement capability and the low frequency AC magnetic field excitation for UXO detection and discrimination have been successfully demonstrated, our study indicates that further improvements are still necessary in order for these techniques to work robustly in field applications.

The advanced MFAM sensors can be easily integrated with TDEM systems to achieve simultaneous measurements of scalar magnetic field and transient EM signals. Such a hybrid magnetometer-EM system is expected to greatly improve the efficiency of UXO remediation, especially in an underwater environment where conducting surveys remains challenging. Accurate location parameters of targets, extracted from the magnetic field data, can be incorporated into the interpretation of the transient decay curves, collected by the TDEM system, to enhance the UXO discrimination and classification. With an array of MFAM sensors, it may be possible to achieve real-time target localization. Challenges in the underwater environment such as limited visibility, mobility of targets and the absence of GPS positioning can potentially be overcome by combining the real-time target localization using the magnetometer array with the high-confidence UXO discrimination with the TDEM system.

In the future, the low frequency AC magnetic field excitation method may be worth further investigation. We have clearly demonstrated the advantage of the method, which is to achieve additional information about the target without compromising the magnetic field measurement. It will be interesting to investigate how the additional information can be beneficial in UXO discrimination and classification and how to reduce motion-induced noises in field applications.

The advanced MFAM sensors also open door to a new research opportunity: transient magnetic field measurement. Traditional TDEM systems use induction coils to measure the dB/dt response of targets after cessation of EM transmitter pulses for UXO discrimination and classification. Although induction coils are effective in detecting dB/dt signal over early and intermediate times, they become less so over late times (> 10 ms) because of the fast decay of the dB/dt signal. Magnetometers measure B field directly. Since B field decays much slower than dB/dt, magnetometers may be more preferred in late-time measurements. Although transient or AC-coupled magnetometers exist that are capable of recovering and acquiring signal shortly after an EM pulse, they are orders of magnitude less sensitive than the MFAM sensors. With the fast-recovery technique developed in this project, MFAM sensors are now capable of measuring magnetic field less than 2 ms after the EM pulses. New and useful information may be revealed by the MFAM sensors in the late-time transient magnetic field measurement.

# Literature Cited

[1] R. Siegel, "Combined Electromagnetic and Magnetometer Data Acquisition and Processing," ESTCP Project MM-0208, 2004.

[2] R. Siegel and R. Selfridge, "Man-Portable Simultaneous Magnetometer and EM System (MSEMS)," ESTCP Project MM-0414, 2008.

[3] R. M. Siegel and K. D. Enriquez, "Underwater Simultaneous EMI and Magnetometer System (USEMS)," ESTCP Project MR-200733, 2011.

[4] D. B. a. D. F. J. Kimball, Optical Magnetometry, Cambridge: Cambridge University Press, 2013.

[5] W. E. Bell and H. L.Bloom, "Optically driven spin precession," *Phys. Rev. Lett.,* vol. 6, p. 280, 1961.

[6] D. W. Allan, "Statistics of Atomic Frequency Standard," *Proceedings of the IEEE,* vol. 54, no. 2, pp. 221-231, 1966.

[7] H. T. a. W. H. B. S. Mathur, "Light shifts in the alkali atoms," *Phys. Rev.,* vol. 171, p. 11, 1968.

[8] S. D. Billings, L. R. Pasion and D. W. Oldenburg, "Discrimination and Identification of UXO by Geophysical Inversion of Total-Field Magnetic Data," ERDC/GSL TR-02-16, U.S. Army Corps of Engineers, Washington DC, 2002.